UNIVERSITY OF BATH

PHD

Structural Health Monitoring and Power Harvesting Systems for Aerospace Applications

Boccardi, Salvatore

Award date:
2019

Awarding institution:
University of Bath

Alternative formats

If you require this document in an alternative format, please contact:
openaccess@bath.ac.uk

Structural Health Monitoring and Power Harvesting Systems for Aerospace Applications

UNIVERSITY OF BATH

Salvatore Boccardi

Thesis submitted for the degree of Doctor of Philosophy

University of Bath

Department of Mechanical Engineering

April 2019

Signature of Author …………………………………… Salvatore Boccardi

COPYRIGHT

Rerum omnium magister usus

Experience is master of all things

Gaius Julius Caesar

Acknowledgments

First of all, I would like to thank my supervisor, Professor Michele Meo. Throughout my PhD he has been the perfect guide and a life teacher, always there, giving advice and sharing his experience whenever I needed. I will never forget his lessons.

I would like to thank my second supervisor, Dr. Francesco Ciampa, who has been a guiding light every time I was lost as well as a good friend.

A big special thank you goes to Fabrizio Bucciarelli and Mario Emanuele De Simone who have been my advisers, my mates, my family. I will never forget the amazing travels, all the jokes and the countless adventures. Sharing my routine with them has been the best thing I could ask for.

Many thanks to Dr. Fulvio Pinto and Dr. Gennaro "Rino" Scarselli. Both of them, in different ways, have allowed me to become the man I am. Further, thank you to Christos Andreades, Marco Boccaccio, Harry Chu, Stefano Cuomo, Dr. Cristiano Figuereido, Francesco Flora, Dr. Andrea Giampiccolo, Dr Dmitri Ginzburg, Dr. Onorio Iervolino, Dr. Gian-Piero "GP" Malfense-Fierro, Dr. Simon Pickering, Mario Rapisarda, Francesco Rizzo and Dr. Carla Silva. Their presence in the office made me enjoy every day at work.

I would like to thank my girlfriend, Francesca Bull, the most wonderful person I have ever met. She is a tidal wave who has changed my life with her vitality and her joy of living. Meeting her has been the best thing that has ever happened to me.

Ma i ringraziamenti piú importanti vanno ai miei genitori, Michele e Anna, che hanno sempre creduto in me e hanno fatto ogni tipo di sacrificio per permettermi di arrivare dove sono ora. Tutto ció che sono, lo devo a loro.

Abstract

Structural health monitoring (SHM) systems and non-destructive evaluation (NDE) methods are commonly used to assess the integrity of aerospace structural components. These techniques allow a continuous and in-situ screening of both composite and metallic structures, thus saving operative costs and maintenance time. In order to collect large quantity of sensing data and due to the complexity of aerospace structures, surface bonded transducers need to be placed in a number of positions of an aircraft. However, transducer information on commercial airliners is still communicated to the user by costly and heavy cables. In the last decade, active wireless technology has been considered, even though all the energy available on aircrafts is already used for other purposes. Thus, energy harvesting systems are necessary to make the communication self-powered.

This work is organised in two main parts. In the first part of this work, three SHM systems for damage evaluation are introduced and validated. A novel nonlinear ultrasonic time domain approach, relying on the time of arrival estimation of the second harmonic nonlinear response, is presented and used to detect and localise material damage. Second order phase symmetry analysis filtering and burst excitation are used so that arrival times of the second order nonlinear elastic waves, measured by a number of receiver sensors, can be estimated through the Akaike Information Criterion approach. Then, Newton's method and unconstrained optimisation are used, in combination, to solve a system of nonlinear equations so that material damage coordinates can be obtained. The methodology was validated through a number of experiments on an impact damaged composite plate and the results showed that defect position can be detected through this method with high accuracy as the maximum error in damage localisation was approximately 5 mm. Furthermore, a novel nonlinear ultrasonic frequency approach, relying on the evaluation of the second order nonlinear response amplitude via two different non-dimensional parameters, is proposed in order to achieve both material damage detection and localisation. Surface bonded transmitting-receiving sensors, placed at opposite sides of the structure, are coupled and the damage position projection on each path between the coupled sensors is calculated through a reciprocal relationship of the nonlinear elastic parameters. All the

results, from each sensor pair, are averaged so that damage position is found. Experimental tests were performed on a damaged composite panel and the results showed that this technique provided high localisation accuracy as the maximum error between the real and the estimated damage location was approximately 13 mm. An evolution of this nonlinear ultrasonic method is also presented, allowing imaging of damage in composite structures. This novel technique considers either the second harmonic or the modulated elastic response, from pairs of surface bonded transducers, as input of a reciprocal relationship in order to find the damage position projection on the path between coupled sensors. A statistical approach is then used to select a cloud of points in order to picture the damaged area. The technique was validated on a complex damaged composite panel and the results showed accurate damage localisation and imaging as the maximum error between the real and the calculated damage area centres was only 1.3 mm. All the proposed SHM methods, unlike traditional linear ultrasonic techniques, allow detection and localisation of damage on composite materials without a priori knowledge of the ultrasonic wave velocity nor a baseline with the undamaged structure.

The second part of this work is focused on the development of thermo-electric energy harvesting in order to feed low-power wireless SHM systems. Temperature gradients, representing the heat waste produced by aircraft engines, are used as input of thermo-electric generators (TEGs) which transform thermal power into an electrical current. Considering that TEG power output can be enhanced by thermal diffusion systems, called heatsinks, a novel air cooling heatsink is here introduced and developed to further improve TEG performance. Numerical finite element thermal simulations were performed to assess the cooling performance of the proposed heatsink and experimental tests were carried out to validate simulation results. The results showed that the novel heatsink allowed an enhancement of TEG temperature difference and power output, in comparison with traditional cylindrical pin heat diffusion systems. In order to allow TEG achieving wireless SHM operative energy requirements of tens of mW, a heat dissipation system, composed by two novel heatsinks combined through a copper sheet and highly oriented pyrolytic graphite layers, was also here introduced and tested. Experimental results revealed that the considered heatsink-TEG arrangement was able to produce an output power over 25 mW, confirming the feasibility of a self-powered wireless SHM system for aerospace applications.

Contents

List of Figures

List of Tables

List of Acronyms

AIC	Akaike Information Criterion
BVID	Barely Visible Damage
CFD	Computer Fluid Dynamics
CFRP	Carbon Fibre Reinforced Plastic
CLE	Classic Linear Elasticity
CNC	Computer Numerical Control
CNE	Classic Nonlinear Elasticity
CPU	Computer Process Unit
GW	Guided Waves
HS	Heatsink
HOS	Higher Order Statistics
LRS	Linear Response Subtraction
MEMS	Micro Electro Mechanical System
NDE	Non-Destructive Evaluation
NEWS	Nonlinear Elastic Wave Spectroscopy
NEMI	Nonlinear Elastic Multi-path Imaging
NEMR	Nonlinear Elastic Multi-path Reciprocal
PGS	Pyrolytic Graphite Sheet
PSA	Phase Symmetry Analysis
PZT	Piezoelectric Transducer
QPC	Quadratic Phase Coupling
SHM	Structural Health Monitoring
SNR	Signal-to-Noise Ratio

TEG	Thermo-Electric Generator
TIM	Thermal Interface Material
TNEWS	Transient Nonlinear Elastic Wave Spectrosopy
ToA	Time of Arrival
WSN	Wireless Sensor Node

Chapter 1

Introduction

1.1 Motivation

In the last years, the increased complexity of modern aircrafts, has led to the necessity of automated health monitoring systems. Monitored data can be captured via a number of transducers, placed in different positions of the aircraft, and need to be communicated to a central computer so that information is available for the user. Historically, onboard aircraft data transfer is achieved using a significant number of wires going from each sensor group to the main computer process unit (CPU). Unfortunately, wires require an expensive maintenance, and, in addition, significantly contribute to the weight of the aircraft. Recently, new technologies, such as wireless communication, have been considered in order to overcome this set of problems. However, wireless technology can be defined as an "active" system which requires electrical power to work. In aerospace applications, all the available power is already used and, thus, the introduction of a self-powered wireless structural health monitoring (SHM) system may be an important novelty which would allow a decrease of both weight of aircrafts and flight costs.

Looking at Figure 1.1, this hypothetical system can be divided in three sections:

- Damage detection and localisation systems for SHM;

- Energy harvesting systems to power wireless units;

- Wireless communication network, which transmits the sensing data to a central unit (CPU).
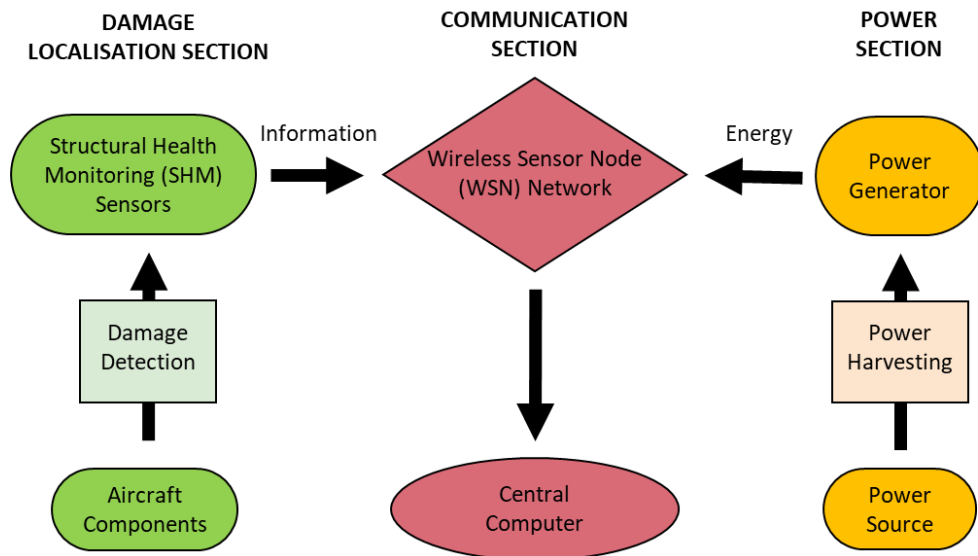
Figure 1.1. Block diagram of a structural health monitoring (SHM) system coupled with a self-powered wireless sensor node (WSN) network.

Considering that wireless technology is already well developed for several applications, the interest of recent studies is more focused on developing accurate and reliable methods for damage assessment as well as power harvesting solutions for aerospace applications.

The increased use of laminar composite materials in aerospace structures has led to the necessity of new rapid and built-in systems. Indeed, although carbon fibre reinforced plastic (CFRP) structures have excellent properties, such as high stiffness to weight and strength to weight ratios, they are subject to delamination, caused by low velocity impacts, which may lead to a catastrophic failure. In the last two decades, structural health monitoring (SHM) systems were developed in order to allow a real-time check, saving time and operative costs. SHM systems comprise a number of transducers, embedded or surface bonded on the structure, which supply continuous remote monitoring of large areas, even in locations with limited access.

On the other hand, wireless sensing networks need a power source in order to transmit sensing information to the user interface. Considering that supplying energy by wires

makes wireless data transmission useless, the most suitable option is harvesting ambient energy through micro-power generators. Even though energy harvesting has already been well developed for large-scale applications, aerospace technologies require small-scale devices which still need to be developed. In this way, part of the big amount of aircraft waste energy can be recovered and re-used for powering a number of applications, such as wireless SHM systems.

Finally, both SHM and power harvesting can be considered as useful technologies to be developed for aerospace applications, as they would help to reduce both operative and maintenance costs.

1.2 Structure

This study proposes two novel nonlinear ultrasonic damage localisation methods which do not rely on a priori knowledge of material features. Furthermore, this thesis, for the first time, shows how in-situ damage imaging is achieved through a nonlinear ultrasonic technique without knowing any material property. Additionally, for the first time, this work introduces the idea of natural convection air cooling to improve thermo-electric power harvesting on aerospace applications.

The work reported in this thesis started from the design and validation of a novel time-domain nonlinear technique able to detect and localise damage on composite structures through ultrasonic guided waves. Then, a new structural health monitoring method was introduced, based on an algorithm which allows damage localisation through the second order nonlinear parameter evaluated in frequency domain. The algorithm was thus extended to achieve damage imaging. Modulated responses of the ultrasonic waves, transmitted in a damaged composite structure, were used as input of a statistical process which allowed the creation of 2D maps of damage. The second part of this thesis shows the improvement of thermo-electric power harvesting through a novel air cooling heatsink system. This last research was carried out in parallel with damage localisation algorithm development to allow the creation of a self-powered structural health monitoring system.

This is a *thesis by publication*. Chapters 3 and 5 are submitted papers whilst chapters 4 and 6 are peer-reviewed papers. All of them are included blended into the style of

the thesis. Each paper is summarised and contextualised within the main narrative through a short introduction which provides continuity and cohesion.

Chapter 2 provides an overall review of relevant background work. In the first part of this chapter, linear and nonlinear damage localisation theory and techniques are evaluated and a selection of methods is studied more in detail in order to have a baseline for the development of new techniques. In the second part of this chapter, a trade-off of the most developed power harvesting technologies is performed in order to select the most reliable and effective way to recover aircraft energy waste. Accordingly, thermo-electric power harvesting is studied more in detail and air cooling methods are evaluated in order to improve harvesting efficiency for application in aircraft pylons. Chapter 3 describes the first structural health monitoring method developed, a novel time-domain damage localisation technique, and the related experimental validation. Chapter 4 introduces a second novel damage localisation method with the purpose of overcoming the limitations of the technique showed in Chapter 3. The novel method, validated on a composite panel, uses a new frequency-domain nonlinear approach which allows damage localisation in composite structures through second harmonic ultrasonic responses. This technique was further developed so that damage imaging could be achieved through a combination of nonlinear ultrasonic structural response and statistics. The novel damage imaging method and its application to a damaged composite structure are described in Chapter 5. Aiming to create a self-powered structural health monitoring system, thermo-electric generation has been introduced so that heat waste energy can be harvested from aircraft engines. Accordingly, Chapter 6 shows the improvement of thermo-electric power harvesting through the introduction of a novel air cooling heatsink system to be placed, together with the harvester, in the aircraft engine pylon. Finally, analysis of the results, strengths and limitations of this research are shown in Chapter 7 which provides also proposals for further work.

Chapter 2

Literature review

Part I: Structural health monitoring

2.1 Introduction to structural health monitoring studies

In order to develop the structural health monitoring (SHM) techniques shown in this thesis, a deep study of the existing damage localisation methods and tools was carried out. In paragraphs 2.2 and 2.3, theories, methods, applicability and limitations of both linear and nonlinear ultrasonic damage identification and localisation are introduced and discussed with appropriate detail. The related information was necessary to the development of the techniques shown in Chapters 3, 4 and 5. Paragraph 2.4 outlines theory and methods of nonlinear modulation wave spectroscopy, foundation of the nonlinear damage imaging technique introduced in Chapter 5. Finally, time of arrival estimation, crucial for the time-domain damage localisation method shown in Chapter 3, is introduced and discussed in paragraph 2.5.

2.2 Linear ultrasonic damage identification

2.2.1 Classical linear elasticity theory

Traditional linear ultrasonic damage detection includes local active structural health monitoring (SHM) techniques based on classical linear elasticity (CLE) theory [1]. In these techniques, multiple actuators are used to generate ultrasonic waves which propagate within the structure; sensors capture these waves in order to estimate the

structural damage through the analysis of the local wave response. When a structure is excited by a transducer, wave modes are generated and wave packets, propagating as superimposition of various modes, are called guided waves (GW) [2]. If the structure is very thin, so that the wavelength can be compared to the thickness, the induced GW are called Lamb waves [3]. These particular waves:

- are dispersive;
- depend on the product of frequency and thickness
- include an infinite number of symmetric and antisymmetric modes.

Lamb waves can be mathematically formulated through the elastic wave equation (Navier's equation) in an unbounded medium [1]:

$$\rho \frac{\partial^2 \mathbf{u}(\mathbf{r}, t)}{\partial t^2} = (\varsigma + \mu)\nabla[\nabla \cdot \mathbf{u}(\mathbf{r}, t)] + \mu \nabla^2 \mathbf{u}(\mathbf{r}, t) \qquad (2.1)$$

where ρ is the structure density, ς is the bulk modulus, μ is the shear modulus and $\mathbf{u}(\mathbf{r}, t)$ is the displacement in function of position $\mathbf{r}$ and time t. This equation is valid for linearly elastic, homogeneous and isotropic materials. After mathematical manipulations [4], the equations for ultrasonic guided Lamb waves in isotropic media, known as the dispersion equations, can be expressed as:

Symmetric Modes   *Anti-symmetric Modes*

$$\frac{\tan\left(\frac{qd}{2}\right)}{\tan\left(\frac{sd}{2}\right)} + \frac{4k^2 qs}{(q^2 - k^2)^2} = 0 \qquad\qquad \frac{\tan\left(\frac{qd}{2}\right)}{\tan\left(\frac{sd}{2}\right)} + \frac{(q^2 - k^2)^2}{4k^2 qs} = 0 \qquad (2.2)$$

where d is the thickness, $q = \sqrt{k_t^2 - k^2}$, $s = \sqrt{k_l^2 - k^2}$ whilst k_t, k_l and k are transversal, longitudinal and group wave numbers, respectively. Analogous expressions can be calculated for the wave group velocity V_g by assuming:

$$V_g = V_{ph} + k \frac{\partial V_{ph}}{\partial k} \qquad (2.3)$$

where V_{ph} is the wave phase velocity. Figure 2.1 shows phase and group velocity dispersion curves for an aluminium plate with thickness of 5 mm.
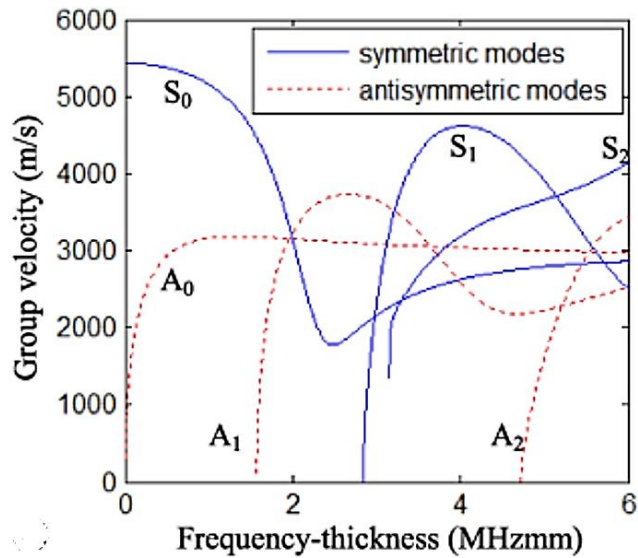
Figure 2.1. Lamb dispersion curves for an aluminium plate. S_i are the symmetric modes whilst A_i are the antisymmetric modes.

2.2.2 Linear damage localisation techniques

According to CLE theory, the change of wave velocity and amplitude can be studied in order to detect and localise damage. A number of techniques based on ultrasonic wave propagation approach have been developed for damage detection and visualisation [5], [6], [7]. Among the others, Tabatabaeipour et al. [8] introduced the Reconstruction Algorithm for the Probabilistic Inspection of Damage (RAPID) which evaluates the probability of damage between several transmitter-receiver pairs in an ultrasonic sparse array. This method allows to create a tomographic image of multiple defects although an a priori spatial probability distribution is needed. Flynn et al. [9] developed a method based on the Rayleigh maximum likelihood estimation, achieving an accurate damage localisation on a stiffened panel. Other authors, such as Michaels et al. [10], compared Lamb waves, captured from a damaged structure through sparse sensor arrays, to baseline signals in order to detect damage. These techniques need significant a priori information which is not always available. In addition, relying on the measurement of changes of macroscopic elastic features, caused by the presence of damage, linear ultrasonic techniques may lack of sensitivity to micro-flaws due to low acoustic impedance mismatch at damage location. In other words, if low frequency ultrasonic waves are used, linear methods can miss nonlinear micro-damage whilst, in the case of high frequency inputs, they can make it appear as a void [11]. These are

20

the main reasons why nonlinear SHM methods are superseding linear techniques in applications where high accuracy is essential, such as inside aircrafts and helicopters.

2.3 Nonlinear elastic wave spectroscopy

2.3.1 Classical nonlinear elasticity theory and second harmonic generation

In structures excited by an actuator, cracks and delamination generate nonlinear elastic responses, i.e. higher harmonics and sub-harmonics of the excitation frequency. This is due to "clapping" motion of the region normal to the crack interfaces or nonlinear friction (rubbing) between the defect surfaces excited by small tangential stresses. Nonlinear elastic parameters can be used in micro-damage detection methods, where linear techniques fail. Nonlinear interaction can be introduced by using the classical nonlinear elasticity (CNE) theory [12]. Considering the longitudinal wave propagation along the x-direction, the wave equation [Eq. (2.1)] can be expressed as the power series of the strain $\varepsilon_x = \partial u(x,t)/\partial x$ [13]:

$$\rho \frac{\partial^2 u(x,t)}{\partial t^2} = \frac{\partial \sigma}{\partial x} = (\varsigma + 2\mu) \left[\frac{\partial}{\partial x} \left(1 + \beta \varepsilon_x + \delta \varepsilon_x^2 \right) \varepsilon_x \right] \tag{2.4}$$

where σ is the stress whilst β and δ are the high order elastic coefficients. This equation is valid for bulk acoustic waves with moderate amplitude displacements, when the nonlinear terms are small compared with the linear ones. In case of dispersive guided Lamb waves, the generation of the second order nonlinear effect, i.e. second harmonic, grows linearly with the propagation distance and arises when the phase velocity of a primary Lamb mode is equal to the phase velocity of the double frequency Lamb wave (cumulative effect [71]). Furthermore, the generated second harmonic Lamb wave is symmetrical, even though Lamb waves are either symmetrical or anti-symmetrical [72]. A reliable damage detection can be achieved through the second order nonlinear coefficient β, strictly related to the second harmonic generation, which is typically two or three order of magnitude higher than third order coefficient δ. The nonlinear parameter β expression is generally deduced from eq. (2.4) via a perturbation theory:

$$\beta = \frac{8A_2}{A_1^2 x k^2} \tag{2.5}$$

In eq. (2.5), A_1 and A_2 are the fundamental and the second harmonic amplitudes, respectively, k is the wave number and x is the propagation distance of the waveform from the nonlinear source (i.e. damage location).

2.3.2 Filtering techniques: phased symmetry analysis

As the initial part of this research was focused on nonlinear damage localisation through a time domain approach, a filtering technique was necessary in order to isolate the nonlinear part of the waveforms recorded by receiver sensors on a damaged plate. The output signals $y_{OUT}(t)$ can be expressed through a Volterra functional series as follows [14], [15], [16]:

$$y_{OUT}(t) = y_1(t) + y_2(t) + \Lambda \tag{2.6}$$

In eq. (2.6), the linear contribution $y_1(t)$ can be calculated as:

$$
\begin{aligned}
y_1(t) &= \int_{-\infty}^{+\infty} h_1(\tau_1)u(t - \tau_1)d\tau_1 \\
&= \frac{U}{2}e^{j\varphi}\int_{-\infty}^{+\infty} h_1(\tau_1)e^{j\omega(t-\tau_1)}d\tau_1 + \text{conjugate term} \\
&= \frac{U}{2}H_1(\omega)e^{j(\omega t + \varphi)} + \text{conjugate term}
\end{aligned}
\tag{2.7}
$$

where h_1 and H_1 are the first order impulse response in time and frequency domain, respectively, U is the transmitted amplitude, φ is the phase, ω is the angular frequency and t is time. The second order term $y_2(t)$ can be expressed as:

$$
\begin{aligned}
y_2(t) &= \int_{-\infty}^{+\infty}\int_{-\infty}^{+\infty} h_2(\tau_1, \tau_2)u(t - \tau_1)u(t - \tau_2)d\tau_1 d\tau_2 \\
&= \int_{-\infty}^{+\infty}\int_{-\infty}^{+\infty} h_2(\tau_1, \tau_2)\frac{U}{2}\left[e^{j[\omega(t-\tau_1)+\varphi]}\right. \\
&\quad \left. + e^{-j[\omega(t-\tau_1)+\varphi]}\right]\frac{U}{2}\left[e^{j[\omega(t-\tau_2)+\varphi]} + e^{-j[\omega(t-\tau_2)+\varphi]}\right]d\tau_1 d\tau_2 \\
&= \frac{U^2}{4}H_2(\omega, \omega)e^{j[2(\omega t + \varphi)]} + \frac{U^2}{2}H_2(\omega, -\omega)e^{j[2(\omega t + \varphi)]} \\
&\quad + \text{conjugate terms}
\end{aligned}
\tag{2.8}
$$

where h_2 and H_2 are the second order impulse response in time and frequency domain, respectively. The linear part of wave signals can be discarded through phase symmetry analysis (PSA) so that the second order term is isolated. PSA is performed by simply imposing the second order symmetry condition, $2j\varphi = \pm 2\pi n j$ [14], with $n \in \mathbb{N}$, where

ℕ is the set of all the natural numbers. Hence, PSA requires two phase shifted waveforms to be sent into a damaged structure. The two output signals can be summed to extract only the nonlinear second order signature (Figure 2.2):

$$y_{PSA}(t) = \frac{y(t)|_{\varphi=0} + y(t)|_{\varphi=\pi}}{2} \qquad (2.9)$$
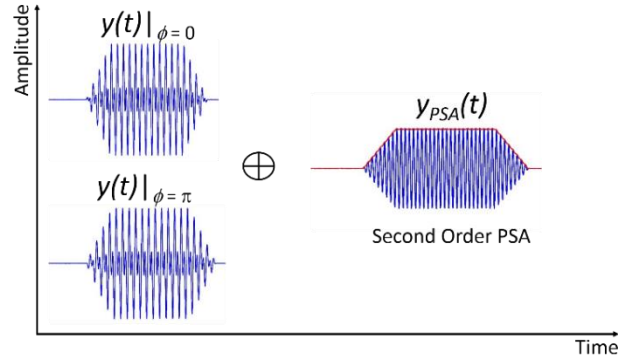
Figure 2.2. Illustration of the second order PSA process. Two tone bursts, transmitted at opposite phases (0 vs π), combine so that the fundamental parts cancel each other leaving only the second harmonic component.

2.3.3 Nonlinear damage localisation via second order elastic coefficient and higher order statistics

Nonlinear ultrasonic methodologies, also known as nonlinear elastic wave spectroscopy (NEWS) methods, rely on the estimation of either second or third order nonlinear parameters extracted from power [17], and higher order spectra [18] of the measured ultrasonic signals. Meo et al. [19], [20], assessed the accuracy of NEWS techniques on a number of different composite structures. Zumpano et al. [21] proposed a new transient non-linear elastic wave spectroscopy (TNEWS) able to detect and localise structural damage in a composite plate through analysis of the uncorrelations between two structural dynamic responses. In general, nonlinear SHM methods demonstrated better accuracy than linear techniques. However, second harmonics generated by instrumentation are considered as a limit for damage localisation accuracy, since they can combine with ultrasonic responses of damaged structures. A further improvement in accuracy of damage localisation methods can be achieved by introducing, as nonlinear inputs, higher order statistics and modulation, which are not affected by instrumentation noise. Among higher order statistics SHM methods, Ciampa et al. [22] proposed a technique, based on the bispectral analysis of

ultrasonic waves, which allowed a more accurate damage localisation in composite structures thanks to quadratic phase coupling.

2.4 Nonlinear modulation wave spectroscopy

2.4.1 Nonlinear acoustic interaction on contact interfaces and modulated wave generation

As mentioned in section 2.3.1, micro-cracks and delamination, when excited with ultrasonic waves, can cause ''clapping" or "rubbing" of the crack interfaces, that lead to nonlinear elastic effects. Nonlinear modulation occurs when two sinusoidal signals at distinctive frequencies are propagating through a media that has a nonlinear mechanism such as a crack; the mixing of these two propagating waves produces spectral sidebands at the sum and the difference between the two frequencies (Figure 2.3). This effect can be analytically expressed by introducing a two-dimensional model of a contact-type interface between two rough elastic surfaces [23]. The expression of the internal stress $\Delta\sigma$, showed by eq. (2.4) along the x-direction, can be rearranged by expanding the stiffness K in a Taylor series approximated to the first order:

$$\Delta\sigma = K\varepsilon = (K_0 + \lambda\varepsilon)\varepsilon = K_0\varepsilon + \lambda\varepsilon^2 \tag{2.10}$$

where ε is the variation of thickness of the contact-type interface whilst K_0 and λ are the linear and nonlinear stiffness coefficients [23]. If the transmitted ultrasonic wave has two driving frequencies, the internal stress can be defined as:

$$\begin{aligned}
\Delta\sigma = A_{0,0} &+ A_{1,0}\cos(\omega_1 t) + A_{0,1}\cos(\omega_2 t) + A_{2,0}\cos(2\omega_1 t) \\
&+ A_{0,2}\cos(2\omega_2 t) + A_{1,-1}\cos[(\omega_1 - \omega_2)t] \\
&+ A_{1,1}\cos[(\omega_1 + \omega_2)t]
\end{aligned} \tag{2.11}$$

where

$$A_{0,0} = \frac{\lambda}{2K_0}\left[A_{1,0}{}^2 + A_{0,1}{}^2\right] \qquad , \qquad A_{1,1} = A_{1,-1} = \frac{\lambda}{K_0{}^2}A_{1,0}A_{0,1}$$

$$A_{1,0} = K_0 D\left(\frac{\partial U_1}{\partial x}\right) \qquad , \qquad A_{0,1} = K_0 D\left(\frac{\partial U_2}{\partial x}\right) \tag{2.12}$$

$$A_{2,0} = \frac{\lambda}{2K_0}A_{1,0}{}^2 \qquad \text{and} \qquad A_{0,2} = \frac{\lambda}{2K_0}A_{0,1}{}^2$$

In eqs. (2.12), U_1 and U_2 are the amplitudes of the transmitted ultrasonic waves whilst D is the average thickness of the defect interface. All the main nonlinear parts of the

resulting ultrasonic wave, due to the presence of the defect, are highlighted in eq. (2.11). Each driving frequency leads to a related second harmonic component (having amplitude $A_{2,0}$ and $A_{0,2}$) and, in addition, two nonlinear modulated responses are generated at the combination frequencies $\omega_1 \pm \omega_2$. Both the amplitudes $A_{1,1}$ and $A_{1,-1}$ of the modulated terms can be used to assess the presence of a defect.
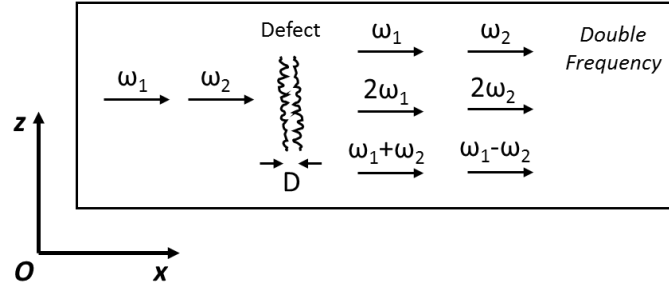
Figure 2.3. Double frequency wave interactions due to the presence of a defect which transfers part of the energy from the driving frequencies to the harmonic and modulation bands.

2.4.2 Nonlinear damage localisation via structural modulated response

According to eqs. (2.12), the second order harmonic amplitudes $A_{2,0}$ and $A_{0,2}$ are higher than the modulated response amplitudes $A_{1,1}$ and $A_{1,-1}$, as $\lambda \ll K_0$. However, signal generators can also produce second order harmonics which contribute to structural responses as instrumentation noise. Even if they are very small, modulated components are not affected by instrumentation noise. Hence, a number of authors are recently considering modulated responses from damaged structures as a more reliable nonlinear source for their SHM techniques [24], [25]. Sohn et al. [26] presented a fatigue crack detection method using nonlinear ultrasonic wave modulation evaluated via a combination of linear response subtraction (LRS) and synchronous demodulation (SD). Malfense Fierro et al. [27] proposed an approach based on the evaluation of nonlinear modulated acoustic moments for the assessment of the loosened state of bolts in a multi-bolted structure.

2.5 Time of arrival estimation

2.5.1 Impact and damage localisation via time of arrival estimation

In the last years, the estimation of time of arrival (ToA) of ultrasonic elastic waves has been the key issue of impact localisation techniques. An acoustic emission source,

such as an impact, generates ultrasonic waves and ToA of the signals received by sensors placed in different positions, can be used to locate impacts on both aluminium and composite structures [27]. Amongst the others, Kundu et al. [29] proposed an optimisation algorithm which identifies the impact point on aluminium and composite structures by minimising an error function based on the difference of ultrasonic wave ToAs. Further, De Simone et al. [30] introduced a methodology that locates impacts on aerospace components through ToA estimation via two different Akaike information criterion (AIC) pickers. Although time of arrival estimation has been widely used in impact localisation techniques, damage localisation might also be achieved through the same technology. Considering that nonlinear elastic waves are generated by cracks and delamination excited by ultrasonic signals, time of arrival of second harmonics can be used to find damage location.

2.5.2 Akaike information criterion

The time of arrival (ToA) of a measured waveform can be calculated through the Akaike information criterion (AIC) method [31]. A single tone burst input, $u(t)$ allows a clear differentiation of starting and ending points from the background noise. For a generic output signal $f[\vartheta]$ of length Ξ, with $\vartheta = 1, \dots, \Xi$, the AIC function $AIC[\vartheta]$ can be written as follows:

$$AIC[\vartheta] = \vartheta \log\big(\mathrm{var}(f[1,\vartheta])\big) + (\Xi - \vartheta - 1) \log\big(\mathrm{var}(f[\vartheta + 1, \Xi])\big) \qquad (2.13)$$

However, a low signal-to-noise ratio (SNR) does not allow the AIC function to perform accurately as the arrival time is not evident. Furthermore, to identify the proper ToA, a limited time window of data must be chosen for the AIC function (Figure 2.4). An improvement of ToA estimation is possible by substituting, in the formulation of $AIC[\vartheta]$, the specific characteristic function, $CF[\vartheta]$, of the filtered signals $y_{PSA}[\vartheta]$. This characteristic function is sensitive to the changes of frequency and can be expressed as follows:

$$CF[\vartheta] = |y_{PSA}[\vartheta]| + |y_{PSA}[\vartheta] - y_{PSA}[\vartheta - 1]| \qquad (2.14)$$

In order to correctly identify the ToA, the time window needs to begin in the non-informative part of the signal (noise) and to terminate in the significant part of the signal (real signal). Thus, the algorithm shortens the time interval of the original time window. The $CF[\vartheta]$ function [Eq.(2.14)] is computed on the shortened signal and introduced as input of the $AIC[\vartheta]$ formulation [Eq.(2.13)]. The global minimum of the

26

AIC function determines the first estimation of the arrival time. Then, the neighbourhood of the first estimation is considered as the new time interval. The CF is calculated in this new time window and the AIC function is applied once again. The ToA of the received signal is obtained as the new global minimum of $AIC[Я]$. For practical uses, every output signal can be Hilbert transformed in order to consider only its envelope. This operation can be useful for obtaining a more accurate ToA estimation [30].
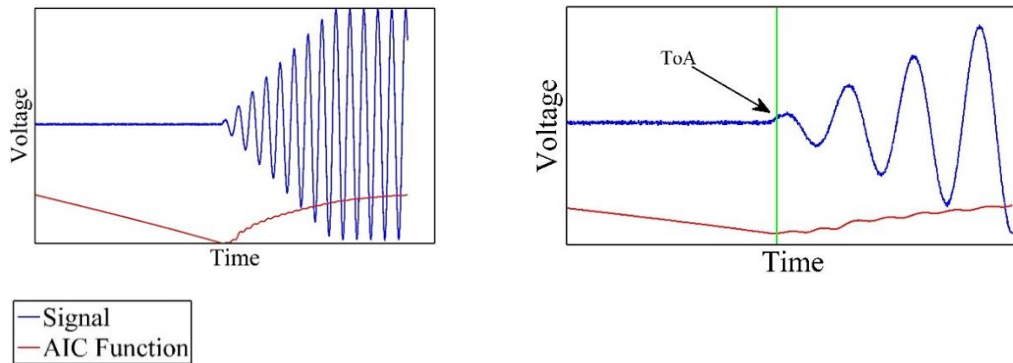
Figure 2.4. AIC method: (a) the first step is used to narrow the scanning region whilst (b) the second step allows time of arrival estimation.

Part II: Power harvesting systems

2.6 Introduction to power harvesting studies

A number of studies was carried out in order to develop a self-powered wireless structural health monitoring system. As specified in Chapter 1, wireless technology might be introduced to improve weight and reliability of aircraft internal communication. Accordingly, the generic layout for a wireless sensor node network is introduced in paragraph 2.7. Considering that wireless technology needs a power source in order to work, a trade-off of the main power harvesting methods was performed, as shown in paragraph 2.8, and thermo-electric generators were chosen as most suitable harvesters for aircraft applications. Paragraph 2.9 outlines theory and applications of the thermo-electric technology, showing the possibility of power output improvements through air cooling heatsinks. Finally, paragraph 2.10 shows the effects of heatsink materials and geometrical features on air cooling heat transfer mechanisms

in order to allow the development of a novel heatsink for thermo-electric generation improvement, as shown in Chapter 6.

2.7 Wireless sensor node network

Real time SHM for aerospace applications requires fast communication of data to the end user. Although communication by wires is the most used on aircrafts, wireless communication can be introduced to replace wires for weight optimisation purposes. A wireless sensor node (WSN) network is composed by a number of wireless sensor nodes that can communicate among each other and with a central control unit [32]. Each WSN is made of three sections: sensor section, communication section and power supply section (Figure 2.5).
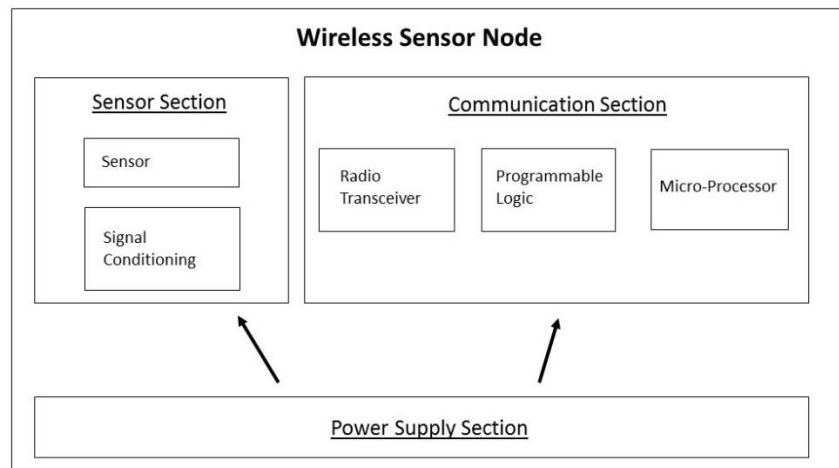
Figure 2.5. Wireless Sensor Node functional diagram. The power supply section provides energy to both sensor and communication sections.

2.7.1 Sensor section

The sensor section includes the sensors used to capture sensible data for structural health monitoring (SHM), such as computed damage and impact locations. Ultrasonic SHM techniques can comprise one or more transducers able to send and receive ultrasonic waveforms. Captured signals are sent to the signal conditioning segment for processing.

2.7.2 Communication section

The communication section, comprising a micro-processor, a programmable logic and a radio transceiver, is used to send sensor data. The transceiver, in addition to the transmitter (TX) and the receiver (RX), has a frequency synthesizer and a digital data interface. The micro-processor and the programmable logic are divided in several modules: the routing module, the positioning module, the network membership module and the media access module. The routing module defines the fastest route of information through the nodes to have the best link between the nodes and the control unit. The positioning module provides the node position, either fixed or variable, in order to know where the information comes from. The network membership module determines if the received data comes from a node that belongs to the network and how many nodes are involved in it. The media access module controls the time at which each node accesses the network, following an established schedule. If the node, after several attempt, cannot access the network, goes in sleep mode allowing the system to save power.

2.7.3 Power supply section

The previously described sections can be considered as 'active' as they need a power supply in order to work. Amongst many types of energy systems, rechargeable batteries are the most popular although, in some regions of the aircraft, their maintenance could be difficult. A way to ease the process could be the introduction of a system that can harvest energy from the engine heat waste and/or from aircraft vibrations. If a power scavenging system is considered, the micro electro mechanical system (MEMS) technology can be used for reducing the size of the nodes.

2.8 Energy harvesting technologies

Energy harvesting allows the conversion of unused ambient energy into electric energy that can be either stored in batteries or used to immediately feed sensor nodes. Main sources of energy present on an aircraft are (see Figure 2.6):

- Solar and artificial light radiation which can be captured by photovoltaic cells placed on the aircraft;

- Mechanical vibrations that can be converted by piezoelectric materials, electromagnetic and electrostatic generators;
- Engine heat waste which can be harvested through thermoelectric, thermionic or pyroelectric generators.
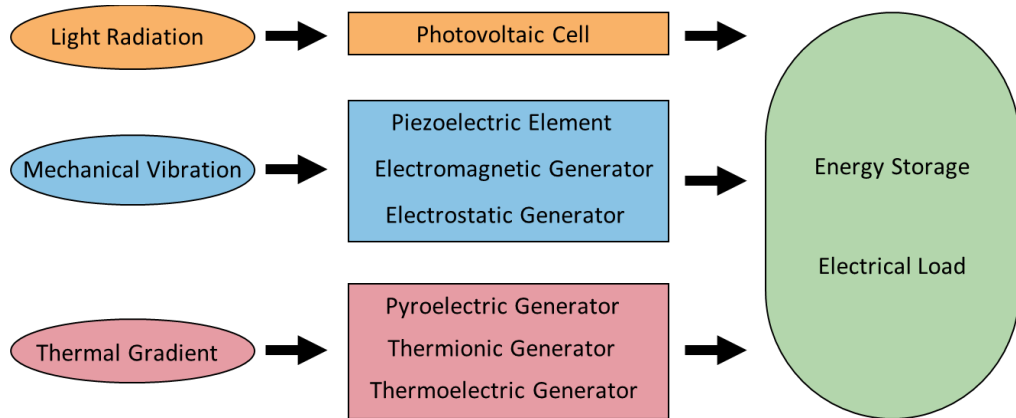
Figure 2.6. Energy sources and respective transducers to power wireless sensor nodes.

2.8.1 Solar energy harvesting: the photovoltaic cell

The photovoltaic effect allows the conversion of light in electricity [33]. Light striking on a silicon layer can be reflected, absorbed or transmitted. The absorbed part provides some of the silicon electrons with enough energy to leave its own atom and travel in the material. At the same time, a silicon atomic bond is left empty generating a 'hole'. Holes, as well as electrons, can travel in the material as empty bonds left by moving electrons. After some time, the system loses the acquired energy thermally and, thus, there is no generation of current. In order to generate electrical current, two silicon layers have to be doped in two different ways:

- Adding atoms having an additional electron (n-type);
- Adding atoms having an electron missing (p-type).

The two layers are placed as in Figure 2.7 making a photovoltaic cell.
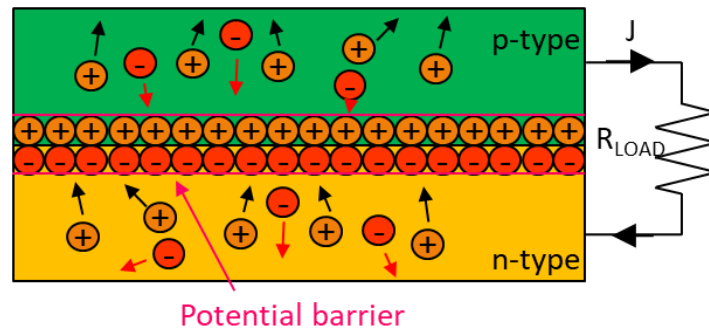
Figure 2.7. Schematic photovoltaic cell: the minus symbols are the electrons and the plus symbols correspond to the holes.

At the n-p junction, two materials with different charge come in contact and, thus, electrons do not leave their atom as they are in equilibrium. However, atom orientation changes in order to reach the state of minimum energy. Such a junction becomes a so called 'potential barrier'. When light strikes on the system, electrons and holes go in opposite directions due to the barrier, creating a potential difference which can be transformed in electrical current. This process allows reliable energy harvesting although only daylight provides enough energy to make the system effective. Unfortunately, artificial light is not as effective as daylight [34].

2.8.2 Energy harvesting from mechanical vibrations

In order to describe how energy can be harvested from mechanical vibrations, a one-dimensional system can be considered. Looking at Figure 2.8, when the generator vibrates, the mass m moves out of phase with the housing, and a transducer can be used to convert part of the damped energy in electrical current. There are several transducing methods [35]:

- a piezoelectric material can convert the strain in the spring into electricity (piezoelectric generator);
- a magnet can be attached to the mass to induce a voltage in a coil (electromagnetic generator);
- an electret can be embedded in the mass to induce a voltage in a capacitor (electrostatic generator).

31
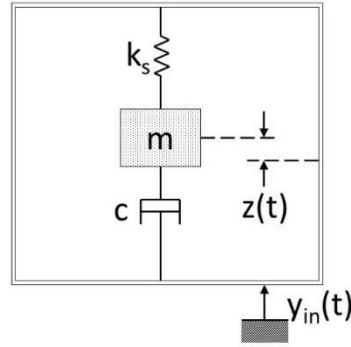
Figure 2.8. Schematic representation of a one-dimensional mechanical vibration energy harvester: m is the mass, k_s is the spring constant, c is the damping constant, z(t) and y_{in}(t) are the mass displacements in box and external system of reference, respectively.

When an external displacement $y_{in}(t)$ occurs, the mass moves of a distance $z(t)$ respect to the housing and the equation of motion is:

$$m\ddot{z}(t) + c\dot{z}(t) + k_s z(t) = -m\ddot{y}_{in}(t) \tag{2.15}$$

where m is the mass, c is the damping constant and k_s is the spring constant. The force on the mass can be expressed as:

$$F = -m\ddot{y}_{in}(t) \tag{2.16}$$

Thus, the power $p(t)$ can be expressed as the product of force and velocity as follows:

$$p(t) = -m\ddot{y}_{in}(t)[\dot{y}_{in}(t) + \dot{z}(t)] \tag{2.17}$$

If the excitation is sinusoidal $(y_{in}(t) = U\cos(\omega t))$, the generated electrical power is:

$$P_{OUT} = \frac{m\zeta U^2 \left(\frac{\omega}{\omega_n}\right)\omega^3}{\left[1 - \left(\frac{\omega}{\omega_n}\right)^2\right]^2 + \left[2\zeta\frac{\omega}{\omega_n}\right]^2} \tag{2.18}$$

where ζ is the transducer damping factor, ω_n is the resonance angular frequency, U is the amplitude of the excitation and ω is the angular frequency of the vibration. The damping factor is strictly related to the transducer choice whilst the power output P_{OUT} is maximum when $\omega = \omega_n$. An important feature is the cubic proportionality between the generated power and the angular frequency of the excitation which allows a much higher power output in environments with high frequency vibrations. If $\omega = \omega_n$, the power output becomes:

$$P_{OUT} = \frac{mU^2\omega_n{}^3}{4\zeta} \tag{2.19}$$

According to this equation, the output is high when the damping factor is low. Unfortunately, a damping factor equal to zero does not exist since a significant amount

32

of unwanted damping is present. This is the damping due to undesirable effects, such as air resistance, that reduces the electrical power output. Although a good amount of energy can be harvested by this system, moving parts are involved and, thus, the reliability of these devices is not as good as other systems such as thermo-electric generators (TEG).

2.8.3 Thermal energy harvesting

− *Pyroelectric materials*

A pyroelectric material has a spontaneous electrical polarisation as a function of temperature. If temperature changes in time, the induced charge in such a material variates as well, generating a current. The pyroelectric current is [36]:

$$I = \frac{dQ_C}{dt} = p_i S \frac{dT}{dt} \tag{2.20}$$

where Q_C is the electric charge, S is the electrode surface, T is the temperature and p_i is the pyroelectric coefficient given by:

$$p_i = \frac{dP_S}{dT} \tag{2.21}$$

where P_S is the magnitude of the electrical polarisation vector [37]. Thus, pyroelectric cells can be used as current sources in environments in which temperatures are variable.

− *Thermionic generators*

Thermionic generators consist in two electrodes at different temperature with a vacuum gap in between [38]. If the temperature T_1 of the cathode is high enough, a number of its electrons evaporate, go across the vacuum gap and condensate on the anode (Figure 2.9b) generating an electrical current. The anode temperature T_2 must be lower than T_1 to avoid back emission of electrons.
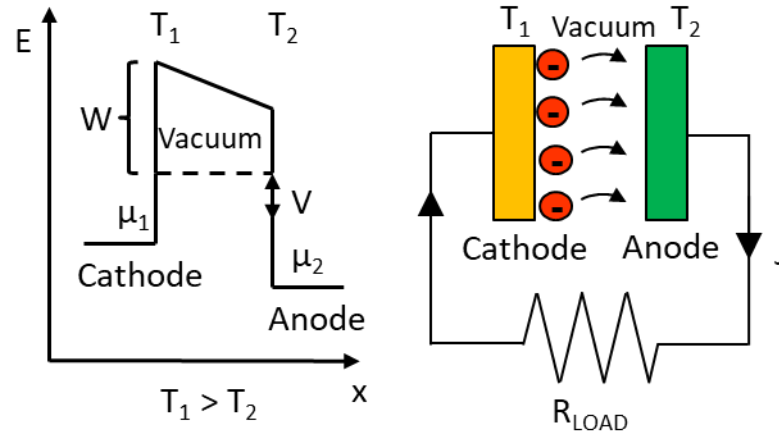
Figure 2.9. Thermionic effect: (a) band structure over the vacuum barrier where μ_1 and μ_2 are the electrochemical potentials, V is the potential difference and W is the work function; (b) schematic representation of a thermionic generator where minus symbols represent the electrons going across the vacuum gap.

Further, electrons to be emitted must have an energy higher than the work function W (Figure 2.9a). This last requirement means that the temperature on the cathode must be very high (more than 1200° C). This is the main drawback of such a harvesting method. The potential barrier W can be lowered by using pn-doping [39] or by reducing the vacuum gap [40].

    – *Thermo-electric generators*

Thermo-electric generators (TEG) harvest energy from a temperature difference. TEGs do not involve moving parts, can generate electrical power continuously and can thus be considered reliable and effective devices. Hence, in next sections, TEG mode of operation is studied more deeply: thermoelectric power harvesting basics are explained, and performance improvement solutions are evaluated.

2.9 Thermo-electric power harvesting

2.9.1 Seebeck effect and Peltier element

The thermoelectric phenomena are described by three effects: the Peltier effect, the Seebeck effect and the Thomson effect. The first two can occur when two dissimilar conductors (or semiconductors) are joined by their two ends forming a thermocouple. The Peltier effect is the generation of a temperature difference between the two ends of the thermo-couple when an electric current is passed through [41]. The Seebeck

effect is the reverse of the Peltier effect i.e. the generation of electric current when the two junctions of the thermocouple are placed at different temperature [42]. The Thomson effect occurs in a single conductor and consists in the generation or absorption of heat when both temperature gradient and electrical current are present. This last effect can be considered negligible [42]. The Seebeck effect as well as the Peltier effect can be studied by modifying Ohm's law. The current density **J** from a heat source can be expressed as:

$$\mathbf{J} = -\sigma_T \alpha \nabla T \tag{2.22}$$

where σ_T is the local electrical conductivity, ∇T is the temperature gradient and α is the Seebeck coefficient defined as:

$$\alpha = -\frac{dV}{dT} \tag{2.23}$$

that is the variation of potential V due to a variation of temperature T. Thermo-electric generators (TEGs), also known as Peltier elements (Figure 2.10), are the most common devices able to harvest energy through the Seebeck effect. They consist in a thermoelectric couple of n-type and p-type material [44] placed electrically in series and thermally in parallel. The aggregation of electrons and holes on the cold side (in the n- and p-type legs, respectively) and their diffusion on the hot side creates an electrical current that can feed a load.
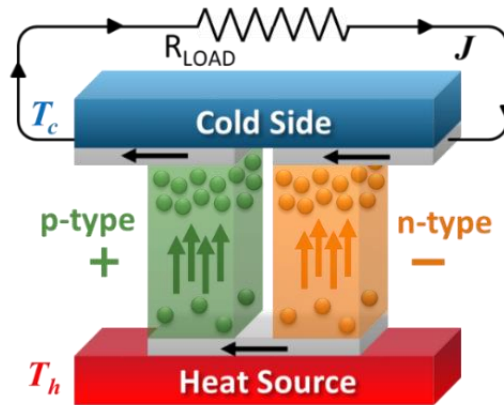
Figure 2.10. Peltier element: the particles (holes and electrons) tend to accumulate on the cold side creating a potential difference. If there is a circuit that links the two sides, an electrical current J is generated and a load R_LOAD (or R_L) can be fed.

2.9.2 TEG classification criteria: the figure of merit

According to section 2.7.1, a good thermoelectric material needs to have a high Seebeck coefficient, a high electric conductivity and a low thermal conductivity. Hence, the Figure of Merit *Z* has been introduced for TEG classification [45]:

$$Z = \frac{\alpha^2 \sigma_T}{k_J} \qquad (2.24)$$

where σ_T is the electric conductivity, k_J is the thermal conductivity and α is the Seebeck coefficient. Unfortunately, these coefficients are not supplied by TEG providers which furnish only their maximum voltage V_{max}, maximum current I_{max} and maximum temperature difference ΔT_{max} at temperature of the hot side T_h. However, this information can be used to extrapolate the parameters used for evaluating *Z* [45]:

$$\alpha = \frac{V_{max}}{T_h} \qquad k_J = \frac{I_{max}}{V_{max}} \frac{T_h}{(T_h - \Delta T_{max})} \qquad \sigma_T = \frac{V_{max}I_{max}}{\Delta T_{max}} \frac{(T_h - \Delta T_{max})}{2T_h} \qquad (2.25)$$

These equations can be used to classify the TEGs on the market.

2.10 Cooling technologies for thermo-electric generators

2.10.1 Introduction

The electric current generated by TEGs is proportional to the temperature difference between TEG hot and cold faces [46]. The hot face temperature of the Peltier element, depending on the heat source, cannot be controlled and, thus, the only way to increase the temperature difference is by decreasing the temperature on TEG cold face. Throughout the years a number of cooling techniques have been studied, developed and used in many different applications such as aerospace, automotive, nuclear and computer systems. Liquid cooling demonstrated to be the most effective technology, due to good conduction and convection properties [47]. However, liquid cooling is only possible through heavy and bulky systems that could be allowed in nuclear and computer applications but definitely excluded in aerospace applications. Hence, air cooling is the most suitable option for aerospace utilisations. Air cooling heatsinks are lightweight and reliable devices which can be easily tailored to the location of the heat source [48]. Thus, a heatsink can be mounted on the cold face of the TEG (Figure 2.11) with the aim of transferring as much heat as possible, increasing TEG temperature

difference and, accordingly, TEG power output. In general, there are three heat transfer modes: conduction, convection and radiation. In cooling applications, radiation is small if compared to the other two and can be neglected [49]. So, heat transfer can be improved by enhancing conduction and convection properties of the heatsink.

- Conduction is strictly related to density and thermal conductivity of the material [49]. However, since an increase of density would result in an increase of weight, heatsink cooling effect can be improved through a good material trade-off;

- Convection depends on convective heat transfer coefficient, temperature and external surface area of the heatsink [49]. Hence, low specific heat of the material and external surface maximisation would lead to heatsink performance improvements.
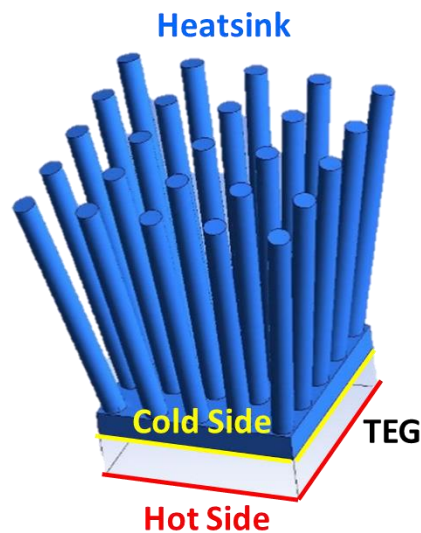
Figure 2.11. Most common TEG-Heatsink system. The heat from TEG upper face is gathered by the heatsink base and transferred to ambient through the pins.

2.10.2 *Heatsink materials*

According to section 2.8.1, a good heatsink material shall have high thermal conductivity and low specific heat (to quickly reach a high heatsink temperature). The high thermal conductivity material classification, showed in Table 2.1, was used as a starting point of the heatsink material choice procedure. The material with the highest thermal conductivity was first considered and its characteristics were studied to evaluate suitability for aerospace applications. If not suitable, the study was then focused on the next material of the table. A suitable heatsink material shall be:

- Cheap;
- Easily available;
- Ductile;
- Lightweight.

According to this procedure, graphene was the first material analysed. Graphene is a single layer of carbon atoms arranged in a hexagonal lattice (Figure 2.12a) which allows an extremely high thermal conduction [53]. However, its nature does not allow to build more than a layer-thick heatsink and, as TEG cold face surface is small, the heat exchange with ambient air (discussed in next paragraph) would be limited.

Table 2.1. High thermal conductivity materials [51], [52].

Material	Thermal Conductivity (W m^{-1} K^{-1})	Specific Heat (J kg^{-1} K^{-1})
Graphene	5300	-
Diamond	2000	516
Silver	430	235
Copper	400	385
Gold	320	129
Aluminium	235	897

Diamond (Figure 2.12b) can be quickly excluded as well as silver and gold due to the very high price. Copper and aluminium can be considered most suitable for heatsink applications due to their cheap price, ductility and availability. Alongside single material studies, hybrid solutions were examined with the aim of improving thermal properties. Vapour grown carbon fibre reinforced plastic [54] reached a high thermal conductivity of 695 W/mK. Copper coated with a high conductivity material using chemical vapour decomposition [55] also produced a good heatsink material as well as copper-diamond composite [56]. However, all these options were discarded because they require complex and expensive manufacturing processes. Hence, copper and aluminium were left as best options. Aluminium is lighter but with thermal properties worse than copper. Thus, aluminium is best when big heatsink volumes are allowed whilst copper can be used in applications with limited available space.
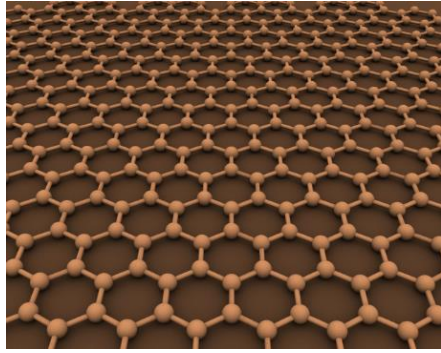
Figure 2.12. Best thermal conductive materials: (a) graphene, (b) diamond.

2.10.3 Heatsink geometry

According to Newton's cooling transfer law, the convective heat transfer rate dQ/dt depends on the heat transfer coefficient h, the exchange surface S and the difference between body temperature T_b and ambient temperature T_{amb}:

$$\frac{dQ}{dt} = hS(T_b - T_{amb}) \tag{2.26}$$

Since there is no control of ambient temperature which depends on the surrounding environment, the heat transfer rate can be improved by enhancing the other parameters. Body temperature can be increased by choosing a low specific heat material, as specified in section 2.8.1. The heat transfer coefficient, depending on several factors, i.e. airflow velocity, external surface, etc., is not easy to manage. Hence, from a geometrical point of view, external surface area is the parameter to be optimised. The most common heatsink configuration consists in a flat base with pins or fins on it (Figure 2.13 and Figure 2.14) [57]: heat source is collected by the flat base and dissipated in the coolant flow through a number of pins or fins.
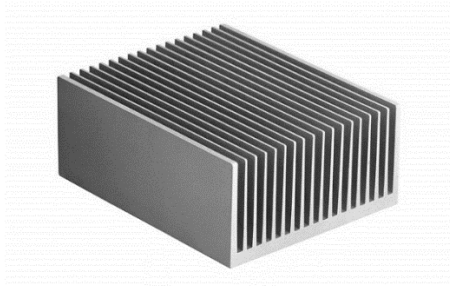
Figure 2.13. Heatsink with fins. Mostly used for applications with forced convection.
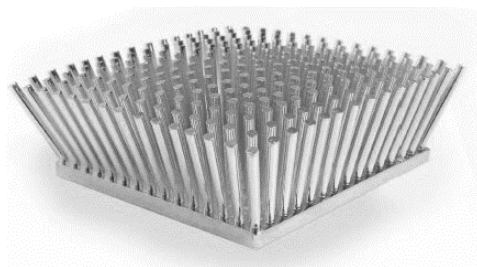
Figure 2.14. Heatsink with pins. Suitable for natural convection environments.

Fin configuration allows a better cooling performance, as the exchange surface is larger. However, considering same external dimensions, a fin heatsink is generally

heavier than a pin heatsink, and its cooling performance would be significantly higher only in forced convection environments [58] which would increase the heat transfer coefficient *h*. Since the idea is to place the TEG-heatsink system in a natural convection environment, i.e. inside the engine pylon, the pin configuration resulted to be more suitable for this application. Several studies have been made about the number and the shape of the pins [58], [60], [61]. Nevertheless, natural convection air cooling can be considered at an early stage.

2.10.4 Thermal Interface Material

Heatsink cooling performance might be jeopardised by poor coupling with TEG cold face. The roughness of both heatsink and TEG surfaces, without an expensive surface grinding, allows the creation of air-filled region at the interface. Air is a thermal insulant which obstructs heat transfer and creates a thermal resistance, decreasing system performance. Thus, a heatsink cannot be simply placed on the TEG but a thermal interface material (TIM) shall be used to improve thermal transmission. Several studies showed that the improvement of thermal coupling is proportional to TIM thermal conductivity and thickness [62]. Among TIMs, thermal compounds have been commonly used in cooling applications as they are cheap and easy to apply. However, their low thermal conductivity is a limiting factor for heatsink systems. In the last decade, new technologies have been developed to improve TIM effectiveness [63], [64]. The interface material selected in this project was pyrolytic graphite, due to its very high in-plane thermal conductivity (see Table 2.2) that allows an improved thermal transmission and a fast heat transfer. This means that pyrolytic graphite sheets (PGS) can be used both as a TIM and a mean to quickly transport heat far from the source. In addition, PGS, as well as thermal compounds, are cheap and easy to apply and, hence, if well used, can be considered the future of thermal management.

Table 2.2. Thermal Interface Material (TIM) properties.

Property	Silicon Thermal Paste	Pyrolytic Graphite Sheets
Density	-	2100 kg m^{-3}
Specific Gravity	2.14	-
Thickness	-	7 x 10^{-5} m
Thermal Conductivity	0.61 W m^{-1} k^{-1}	1500 W m^{-1} K^{-1} in plane 20 W m^{-1} K^{-1} out of plane

Chapter 3

Time domain approach for nonlinear damage localisation in composite materials

3.1 Motivation: nonlinear damage localisation without a priori knowledge of the material

The continuous improvements of the aerospace sector led to the necessity of advanced structural health monitoring (SHM) techniques which are accurate, reliable and, in addition, power saving. The initial purpose of this study was the achievement of damage detection and localisation on structures suitable for the upcoming aerospace applications such as composite panels and stiffeners. The preliminary part of the literature review showed that the nonlinear part of ultrasonic waves, captured from damaged structures, can be used as input for a number of SHM methods. However, most of them rely on a priori knowledge of structural properties such as group wave velocity, layup and/or thickness. This led to the idea of a new nonlinear technique that allows to accomplish the aforementioned task without baseline information.

3.2 Summary: damage localisation via phase symmetry analysis and time of arrival estimation

The novel method works through two sets of three surface attached acoustic emission PZT transducers placed on opposite edges of a composite panel. The transducers, in

each set, must be close to each other in order to neglect the effect of composite fibre orientation on wave group velocity. The technique was able to locate damage via a two-step process. In the first step, an ultrasonic wave input signal was sent from one transducer of the first set and received by all the sensors of the second set. Measured signals were Hilbert transformed and then filtered using phase symmetry analysis [14] to isolate the second harmonic contribution. The time of arrival (ToA), for each of the three received signals, was estimated via the Akaike information criterion method [31]. Then, two time differences Δt were calculated by subtracting one of the ToAs to the other two and were used as input of the following equations:

$$\Delta t_{54} \approx \frac{\sqrt{(x_D - x_5)^2 + (y_D - y_5)^2}}{V_{D5}^{(NL)}} + \frac{\sqrt{(x_D - x_4)^2 + (y_D - y_4)^2}}{V_{D4}^{(NL)}} \tag{3.1}$$

$$\Delta t_{64} \approx \frac{\sqrt{(x_D - x_6)^2 + (y_D - y_6)^2}}{V_{D6}^{(NL)}} + \frac{\sqrt{(x_D - x_4)^2 + (y_D - y_4)^2}}{V_{D4}^{(NL)}} \tag{3.2}$$

where (x, y) are coordinates in an appropriate Cartesian reference frame xOy, subscripts D, 4, 5, 6 denote damage and sensor numbers, respectively, V_{Di} is the wave group velocity and (NL) denotes the nonlinear elastic wave contribution after the PSA filtering. In the second step, the same operations were repeated for the signal sent from one transducer of the second set and received by the sensors of the first set feeding the following equations:

$$\Delta t_{21} \approx \frac{\sqrt{(x_D - x_2)^2 + (y_D - y_2)^2}}{V_{D2}^{(NL)}} + \frac{\sqrt{(x_D - x_1)^2 + (y_D - y_1)^2}}{V_{D1}^{(NL)}} \tag{3.3}$$

$$\Delta t_{31} \approx \frac{\sqrt{(x_D - x_3)^2 + (y_D - y_3)^2}}{V_{D3}^{(NL)}} + \frac{\sqrt{(x_D - x_1)^2 + (y_D - y_1)^2}}{V_{D1}^{(NL)}} \tag{3.4}$$

Since the receiving sensors are very close to each other, the wave group velocity of a transducer set can be assumed as a constant, i.e. $V_{D4}^{(NL)} \equiv V_{D5}^{(NL)} \equiv V_{D6}^{(NL)}$ and $V_{D1}^{(NL)} \equiv V_{D2}^{(NL)} \equiv V_{D3}^{(NL)}$. Hence, the problem is described by a system with four equations [Eqs. (3.1), (3.2), (3.3) and (3.4)] and four unknowns $\left(x_D, y_D, V_{D4}^{(NL)}, V_{D1}^{(NL)}\right)$. The system was solved via a combination of Newton's iterative method [65] and unconstrained optimisation [66] to obtain damage coordinates and group velocities.

3.3 Results: damage localisation and group wave velocity estimation

Experimental tests were performed on a damaged quasi-isotropic CFRP composite panel with delamination. The optimal second order harmonic response on the damaged composite plate was found through a series of ultrasonic sweeps between 150 and 500 kHz with a frequency step of 70 Hz. The highest maximum value was achieved at the fundamental frequency of 318.95 kHz that was chosen as driving frequency of the transmitted signals. Results are shown in Table 3.1.

Table 3.1. True and Calculated damage position and nonlinear group velocities.

	True	Calculated
x_D **(mm)**	120	120
y_D **(mm)**	130	125
$V_{D3}^{(NL)}$ **(m/s)**	n/a	2880
$V_{D1}^{(NL)}$ **(m/s)**	n/a	3139

The estimated point showed the presence of an error expressed by the following formula:

$$\Psi = \sqrt{(x_{real} - x_{calculated})^2 + (y_{real} - y_{calculated})^2} \tag{3.5}$$

where (x_{real}, y_{real}) and ($x_{calculated}$, $y_{calculated}$) are the coordinates of real and calculated damage positions, respectively. The results showed that damage location was found with satisfactory accuracy at the driving frequency of 319.85 kHz, with a maximum location error of ~5 mm.

3.4 Errata

Paragraph 2 of the paper specifies an incorrect formulation for the spectrum of a tone burst. A sine tone burst *f(t)* (normalised for simplicity) and its Fourier transform *F(jω)* can be expressed as follows [70]:

$$f(t) = \begin{cases} \sin \omega_0 t & |t| \leq T_p/2 \\ 0 & \text{otherwise} \end{cases} \tag{3.6}$$

$$F(j\omega) = -j\frac{T_p}{2}\left\{\frac{\sin[(\omega - \omega_0)\,T_p/2]}{(\omega - \omega_0)\,T_p/2} - \frac{\sin[(\omega + \omega_0)\,T_p/2]}{(\omega + \omega_0)\,T_p/2}\right\} \tag{3.7}$$

where T_p and ω_0 are the time length and the driving angular frequency of the burst, ω is the angular frequency, t is the time and j is the imaginary unit. Thus, the considered spectrum is represented by a purely imaginary odd function that is the sum of a pair of shifted imaginary sinc functions. Considering only positive angular frequencies (Figure 1b of the paper), the main lobe of the function crosses zero at $\omega_0 \pm 2\pi/T_p$ so that, if the duration (or number of cycles N as $T_p = 2\pi N$) of the tone burst is increased, its spectral width decreases. This demonstrates that, if the number of cycles is high ($T_p \to \infty$), the tone burst spectrum can be approximated to a continuous wave spectrum.

3.5 Paper: nonlinear damage detection and localization using a time domain approach

The novel damage detection and localisation technique, details of data collection, experiments and results were published by Nondestructive Characterization and Monitoring of Advanced Materials, Aerospace, and Civil Infrastructure [69]. The Statement of Authorship Form and the paper are shown in next pages.

This declaration concerns the article entitled:								
Nonlinear Damage Detection and Localisation using a Time Domain Approach								

Publication status (tick one)								
draft manuscript		**Submitted**		**In review**		**Accepted**		**Published** X

Publication details (reference)	Boccardi, S., Calla, D.B., Fierro, G.P.M., Ciampa, F. and Meo, M., 2016, April. Nonlinear damage detection and localization using a time domain approach. In Nondestructive Characterization and Monitoring of Advanced Materials, Aerospace, and Civil Infrastructure 2016 (Vol. 9804, p. 98040T). International Society for Optics and Photonics
Candidate's contribution to the paper (detailed, and also given as a percentage).	The candidate contributed to/ considerably contributed to/predominantly executed the… Formulation of ideas: 50% I proposed the idea of using time of arrival estimation of nonlinear ultrasonic waves. My supervisor introduced me to filtering via phase symmetry analysis and proposed the idea of close receivers to avoid composite fibre effect on ultrasonic wave velocity. Design of methodology: 95% I designed the methodology by creating a script able to implement the proposed technique. My co-authors contributed to the mathematical formulation. Experimental work: 85% I carried out all the experiments, implemented and performed the method in post-process. My co-authors collected most of data. Presentation of data in journal format: 95% I decided the structure, collated data, wrote all drafts, prepared all figures. My supervisor provided feedback on drafts and helped with submission process.
Statement from Candidate	This paper reports on original research I conducted during the period of my Higher Degree by Research candidature.
Signed	*Boccardi Salvatore* **Date** 04/06/2019

Nonlinear Damage Detection and Localisation Method using a Time Domain Approach

S. Boccardi, D. B. Callá, G. P. Malfense-Fierro, F. Ciampa, M. Meo

Material Research Centre, Department of Mechanical Engineering, University of Bath, Bath BA2 7AY, UK

Abstract

This paper presents a material damage detection and localisation technique based on nonlinear elastic waves propagation in a composite laminate. The proposed method relies on the time of arrival estimation of the second harmonic nonlinear response obtained with second order phase symmetry analysis filtering and burst excitation. The Akaike Information Criterion approach was used to estimate the arrival times of the second order nonlinear elastic waves, measured by six receiver transducers. Then, a combination of Newton's method and unconstrained optimisation was employed to solve a system of nonlinear equations in order to obtain the material damage coordinates. To validate this methodology, experimental tests were carried out on a damaged composite plate. The results showed that this technique allows detecting and localising the material defect position with high accuracy. In particular, the maximum error in the estimation of damage location at the driving frequency of 319.85 kHz was nearly 5 mm.

1. Introduction

Developments in carbon fibres reinforced plastic materials have allowed a radical advancement in lightweight aerospace applications. However, these components are sensitive to low-velocity impact damage, which can considerably degrade the structural integrity and, if not detected, it might result in catastrophic failures.

In the last decade, structural health monitoring (SHM) systems based on wave propagation approach have been used for damage detection and visualisation [1], [2], [3], [4], [5], [6]. Flynn et al. proposed a statistical method based on the maximum

likelihood estimation of the material defects location [7]. Velsor et al. [8] introduced the Reconstruction Algorithm for the Probabilistic Inspection of Damage (RAPID), which is used to construct tomographic images of multiple defects. Other authors, such as Yu et al. [9] and Purekar et al. [10], developed damage localisation systems based on ultrasonic phased arrays. All the above-mentioned techniques are based on linear elastodynamics and analyse the acoustic impedance contrast due to the presence of material damage.

However, a number of studies in literature have shown that a better sensitivity to structural defects and micro-cracks can be achieved by measuring the nonlinear response of damaged materials. In this regard, frequency domain methodologies, based on the calculation of either second or third order nonlinear parameters [11], [12], [13], [14], [15] and higher order approaches [16], [17], were used to determine the presence of material flaws.

This paper presents a novel nonlinear time domain approach for the detection and localisation of damage on a composite plate-like structure. This technique relies on the arrival time (ToA) measurements of the second order nonlinear response from six surface attached piezoelectric (PZT) transducers. The second harmonic signal is extracted by means of the second order phase symmetry analysis (PSA) method [18], [19]. Compared to standard digital filters (e.g. Butterworth and Chebyshev), PSA allows filtering the measured waveforms without any signal alteration. Indeed, by exploiting the invariant properties of the phase of ultrasonic waves, the second order material nonlinear response can be obtained from the sum of two opposite phase input signals. The arrival times of the waves are then calculated through the Akaike Information Criterion (AIC) method [20]. Finally, a system of nonlinear equations is solved using a combination of Newton's method and unconstrained optimisation in order to obtain the damage location coordinates.

The layout of the paper is as follows: in Section 2 the PSA for the signal filtering is presented. Section 3 outlines the main characteristics of AIC method for the time of arrival identification. In Section 4 the system of nonlinear equations for the damage localisation is deduced. Section 5 reports the experimental set-up and Section 6 presents the damage location results for a composite plate. Then, in Section 7, the conclusions of the adopted method are discussed.

2. Phase Symmetry Analysis

In order to perform the second order PSA with phase shifted driving signals, a single tone burst input, *u(t)*, with 200 cycles was chosen [Figure (1a)]. Such an input waveform allows a clear differentiation of the starting and ending points from the background noise, and the high number of cycles was set in order to assume the tone burst as a continuous signal, i.e. $u(t) = A\cos(\omega t + \varphi)$, where ω is the angular frequency, φ is the phase and *A* is the amplitude. Indeed, the spectrum *U(ω)* of a tone burst for a central angular frequency $\omega = 2\pi f$ is [21]:

$$U(\omega) = a\cos(\omega t) \tag{1}$$

where *a* is the input amplitude that can be expressed as:

$$a = A\frac{N}{N+M}\left(\frac{\sin q}{q} \mp \frac{\sin r}{r}\right) \tag{2}$$

where *N* is the number of cycles of the tone-burst, *M* is the number of cycles between two consecutive bursts, whilst *q* and *r* are defined as $q = N[1/(N+M) - 1]\pi$ and $r = N[1/(N+M) + 1]\pi$, respectively. The tone burst spectrum envelope is centred on the central frequency *f* of the cosine function. The bandwidth of the fundamental peak [Figure (1b)] depends on the number of cycles *N* through the ratio $2\frac{1}{N}f$ [21]. Clearly, increasing *N* up to 200 cycles, the spectrum approaches the case of a continuous waveform.
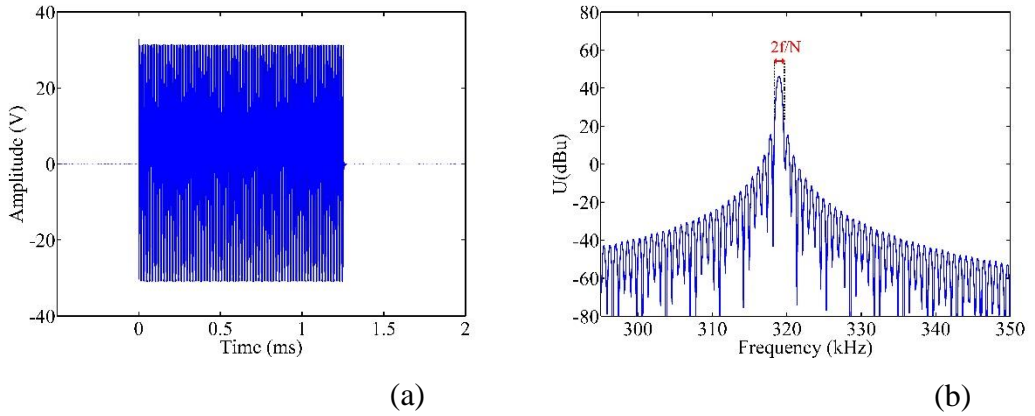
Figure 1. (a) Cycles burst; (b) N cycles burst spectrum.

The output signals *y(t)* recorded by the receiver sensors [Figure (2)] can be expressed through a Volterra functional series as follows [18], [19], [22]:

$$y(t) = y_1(t) + y_2(t) + \cdots \tag{3}$$

Where the linear contribution $y_1(t)$ is:

$$y_1(t) = \int_{-\infty}^{+\infty} h_1(\tau_1)u(t - \tau_1)d\tau_1$$

$$= \frac{A}{2}e^{j\varphi} \int_{-\infty}^{+\infty} h_1(\tau_1)e^{j\omega(t-\tau_1)}d\tau_1 + \text{conjugate term} \qquad (4)$$

$$= \frac{A}{2}H_1(\omega)e^{j(\omega t+\varphi)} + \text{conjugate term}$$

and the second order term $y_2(t)$:

$$y_2(t) = \int_{-\infty}^{+\infty}\int_{-\infty}^{+\infty} h_2(\tau_1,\tau_2)u(t - \tau_1)u(t - \tau_2)d\tau_1 d\tau_2$$

$$= \int_{-\infty}^{+\infty}\int_{-\infty}^{+\infty} h_2(\tau_1,\tau_2)\frac{A}{2}\left[e^{j[\omega(t-\tau_1)+\varphi]}\right.$$

$$+ \left. e^{-j[\omega(t-\tau_1)+\varphi]}\right]\frac{A}{2}\left[e^{j[\omega(t-\tau_2)+\varphi]} + e^{-j[\omega(t-\tau_2)+\varphi]}\right]d\tau_1 d\tau_2 \qquad (5)$$

$$= \frac{A^2}{4}H_2(\omega,\omega)e^{j[2(\omega t+\varphi)]} + \frac{A^2}{2}H_2(\omega,-\omega)e^{j[2(\omega t+\varphi)]}$$

$$+ \text{conjugate terms}$$

where $h_1(\tau_1)$ and $h_2(\tau_1,\tau_2)$ are the impulse responses for the first and second order, respectively.

The PSA method can be used to eliminate the linear part from the signals acquired by simply imposing the second order symmetry condition, $2j\varphi = \pm 2\pi kj$ [18], with $k \in \mathbb{N}$, where $\mathbb{N}$ is the set of all natural numbers. Thus, PSA consists in sending two phase shifted waveforms into the damaged structure. The two output signals are summed to extract only the nonlinear second order signature [Figure (3)]:

$$y_{PSA}(t) = \frac{y(t)|_{\varphi=0} + y(t)|_{\varphi=\pi}}{2} \qquad (6)$$

For practical uses, the output signals are Hilbert transformed in order to consider only their envelope. This operation is useful for obtaining a more accurate ToA estimation.
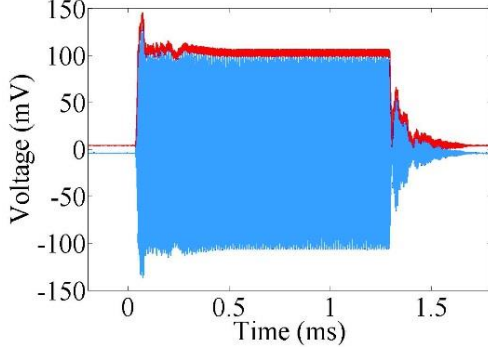
Figure 2. Measured signal and its envelope.
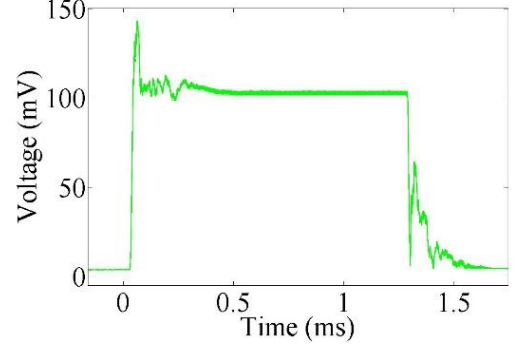
Figure 3. Envelope of the signal after the PSA.

3. Time of Arrival estimation

The filtered signals are analysed, in order to calculate the ToA of the measured waveforms, using the Akaike Information Criterion (AIC) method [20]. For a generic output signals $f[\vartheta]$ of length Ξ, with $\vartheta = 1, \dots, \Xi$, the AIC function $AIC[\vartheta]$ can be written as follows:

$$AIC[\vartheta] = \vartheta \log\big(\mathrm{var}(f[1,\vartheta])\big) + (\Xi - \vartheta - 1) \log\big(\mathrm{var}(f[\vartheta + 1, \Xi])\big) \qquad (7)$$

However, if the signal-to-noise ratio (SNR) is low, the *AIC* function does not perform well and the arrival time is not evident. Furthermore, to identify the proper ToA, a limited time window of data must be chosen for the *AIC* function.

An improvement of the ToA estimation is possible by substituting in the formulation of $AIC[\vartheta]$ the specific characteristic function, $CF[\vartheta]$, of the filtered signals $y_{PSA}[\vartheta]$. These characteristic functions are sensitive to the changes of frequency and can be expressed as follows:

$$CF[\vartheta] = |y_{PSA}[\vartheta]| + |y_{PSA}[\vartheta] - y_{PSA}[\vartheta - 1]| \qquad (8)$$

In order to have a correct identification of the ToA, the time window has to start in the non-informative part of the signal (noise) and to end in the significant part of the signal (real signal). Thus, the algorithm shortens the time interval of the original time window.

The $CF[\vartheta]$ function [Eq. (8)] is computed on the shortened signal and it is used in the $AIC[\vartheta]$ formulation [Eq. (7)]. The global minimum of the *AIC* function determines the first estimation of the arrival time. Thereafter, the neighbourhood of the first estimation is considered. The *AIC* function is applied once again on the *CF* in this new time

50

interval. The global minimum of $AIC[\vartheta]$ is calculated again and it defines the ToA of the received signal. Finally, it is necessary to consider the beginning of the transmitted signal as the reference initial time. For this purpose, the final ToA value is tuned as shown in Figure (4).

(a)   (b)
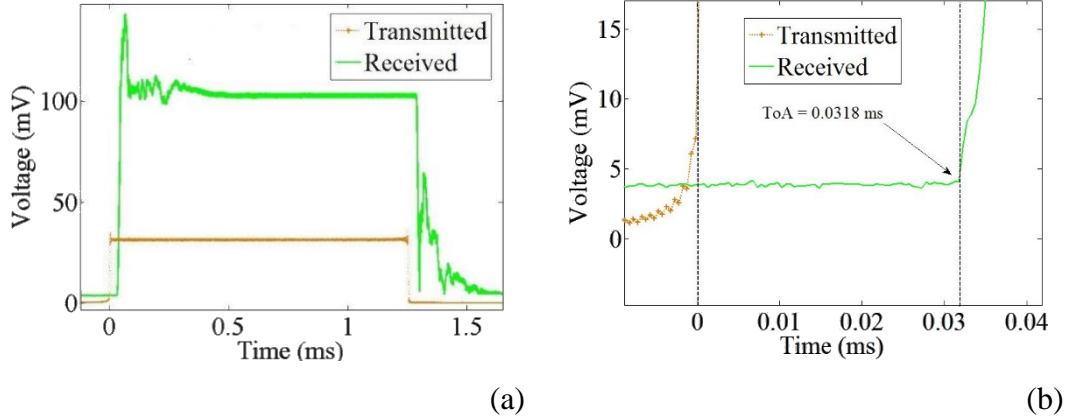
Figure 4. (a) ToA between the transmitted signal (cross marked line) and the received one (continue line); (b) focus on the beginning of the signals for the estimation.

4. Damage localisation algorithm

The method for the damage localisation consists in two steps and can be explained by referring to Figure (5).

(a)

(b)
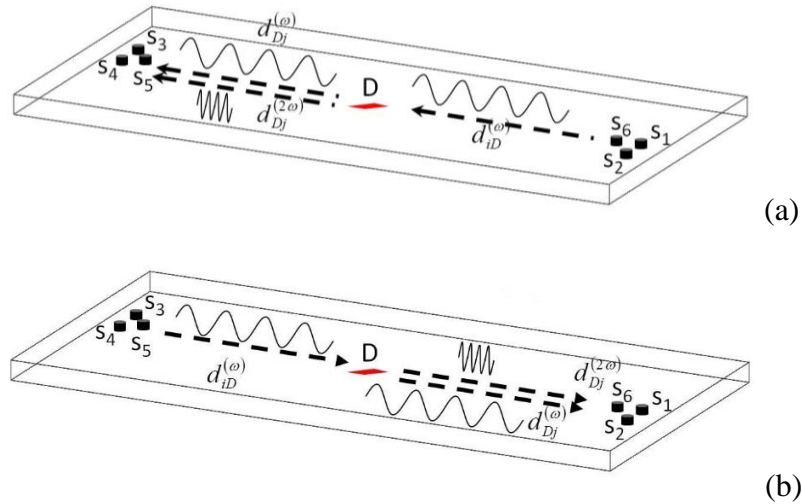
Figure 5. First step (a) and second step (b) of the damage localisation method.

In the first step, an ultrasonic wave input signal is sent from the transducer S_1 and received by the sensors S_3, S_4 and S_5. The ToA of each received signal can be expressed as follows:

$$t_{13} = t_{1D}^{(L)} + t_{D3}^{(L,NL)}$$

$$= \frac{\sqrt{(x_1 - x_D)^2 + (y_1 - y_D)^2}}{V_{1D}^{(L)}} + \frac{\sqrt{(x_D - x_3)^2 + (y_D - y_3)^2}}{V_{D3}^{(L,NL)}} \quad (9)$$

$$t_{14} = t_{1D}^{(L)} + t_{D4}^{(L,NL)}$$

$$= \frac{\sqrt{(x_1 - x_D)^2 + (y_1 - y_D)^2}}{V_{1D}^{(L)}} + \frac{\sqrt{(x_D - x_4)^2 + (y_D - y_4)^2}}{V_{D4}^{(L,NL)}} \quad (10)$$

$$t_{15} = t_{1D}^{(L)} + t_{D5}^{(L,NL)}$$

$$= \frac{\sqrt{(x_1 - x_D)^2 + (y_1 - y_D)^2}}{V_{1D}^{(L)}} + \frac{\sqrt{(x_D - x_5)^2 + (y_D - y_5)^2}}{V_{D5}^{(L,NL)}} \quad (11)$$

Where (x_i, y_i) are the sensors and damage coordinates in a Cartesian reference frame [see Figure (6)], t_{iD} and V_{iD} are the arrival times and group velocities of the propagating waves from the transmitter transducer to the damage location, t_{Dj} and V_{Dj} are the arrival times and group velocities of the propagating waves from the damage to the receiver sensors, (L) corresponds to the linear elastic wave contribution and (L, NL) denotes the linear and nonlinear elastic waves propagating from the damage.

As seen in Section 2, the measured signals are filtered with the PSA to have only the second harmonic contribution. Then, the ToA are calculated with the AIC method (see Section 3).

Subtracting Eq. (9) from Eqs. (10) and (11) to eliminate the contribution of the signal from the transmitter sensor to the damage, yields:

$$\Delta t_{43} \approx \frac{\sqrt{(x_D - x_4)^2 + (y_D - y_4)^2}}{V_{D4}^{(NL)}} + \frac{\sqrt{(x_D - x_3)^2 + (y_D - y_3)^2}}{V_{D3}^{(NL)}} \quad (12)$$

$$\Delta t_{53} \approx \frac{\sqrt{(x_D - x_5)^2 + (y_D - y_5)^2}}{V_{D5}^{(NL)}} + \frac{\sqrt{(x_D - x_3)^2 + (y_D - y_3)^2}}{V_{D3}^{(NL)}} \quad (13)$$

where (NL) denotes the nonlinear elastic wave contribution after the PSA filtering.

In the second step, the same operations are repeated for the signal sent from S_4 and received by S_1, S_2 and S_6:

$$t_{41} = t_{4D}^{(L)} + t_{D1}^{(L,NL)}$$

$$= \frac{\sqrt{(x_4 - x_D)^2 + (y_4 - y_D)^2}}{V_{4D}^{(L)}} + \frac{\sqrt{(x_D - x_1)^2 + (y_D - y_1)^2}}{V_{D1}^{(L,NL)}} \quad (14)$$

$$t_{42} = t_{4D}^{(L)} + t_{D2}^{(L,NL)}$$

$$= \frac{\sqrt{(x_4 - x_D)^2 + (y_4 - y_D)^2}}{V_{4D}^{(L)}} + \frac{\sqrt{(x_D - x_2)^2 + (y_D - y_2)^2}}{V_{D2}^{(L,NL)}} \quad (15)$$

$$t_{46} = t_{4D}^{(L)} + t_{D6}^{(L,NL)}$$

$$= \frac{\sqrt{(x_4 - x_D)^2 + (y_4 - y_D)^2}}{V_{4D}^{(L)}} + \frac{\sqrt{(x_D - x_6)^2 + (y_D - y_6)^2}}{V_{D6}^{(L,NL)}} \quad (16)$$

As before, the PSA filtering is applied and Eq. (14) is subtracted from Eqs. (15) and (16):

$$\Delta t_{21} \approx \frac{\sqrt{(x_D - x_2)^2 + (y_D - y_2)^2}}{V_{D2}^{(NL)}} + \frac{\sqrt{(x_D - x_1)^2 + (y_D - y_1)^2}}{V_{D1}^{(NL)}} \quad (17)$$

$$\Delta t_{61} \approx \frac{\sqrt{(x_D - x_6)^2 + (y_D - y_6)^2}}{V_{D6}^{(NL)}} + \frac{\sqrt{(x_D - x_1)^2 + (y_D - y_1)^2}}{V_{D1}^{(NL)}} \quad (18)$$

Since the receiving sensors are very close each other [see Figure (5)], it is possible to assume $V_{D3}^{(NL)} \equiv V_{D4}^{(NL)} \equiv V_{D5}^{(NL)}$ and $V_{D1}^{(NL)} \equiv V_{D2}^{(NL)} \equiv V_{D6}^{(NL)}$ neglecting the fibre orientation effect of the composite plate. Hence, the problem is described by a system with four equations [Eqs. (12), (13), (17) and (18)] and four unknowns $\left(x_D, y_D, V_{D3}^{(NL)}, V_{D1}^{(NL)} \right)$.

Then, similarly to Ciampa and Meo [23], the Newton-Raphson or Newton's method can be used to solve this nonlinear problem. It is an iterative algorithm for finding the roots of a nonlinear homogenous system of equations $\mathbf{F}(\mathbf{x}) = 0$, where $\mathbf{F}(\mathbf{x})$ is the vector of the functions F_i with $i = (1,2,3,4)$ and $\mathbf{x}$ is the vector of unknowns $x = \left[x_D, y_D, V_{D3}^{(NL)}, V_{D1}^{(NL)} \right]$.

This method converges quadratically to the result from an initial guess point close enough to the solution. The Newton iteration $\mathbf{x}^{n+1}$ from a current point $\mathbf{x}^n$ is given by:

$$\mathbf{x}^{n+1} = \mathbf{x}^n + \delta \mathbf{x}^n = \mathbf{x}^n - J(\mathbf{x}^n)^{-1} \mathbf{F}(\mathbf{x}^n) \quad (19)$$

where $J(\mathbf{x})$ is the Jacobian matrix. In this case, $J(\mathbf{x})$ is related to the four unknowns considered:

$$J(\mathbf{x}) = \frac{\partial \mathbf{F}(\mathbf{x})}{\partial \mathbf{x}} = \begin{bmatrix} \dfrac{\partial F_1(\mathbf{x})}{\partial x_D} & \dfrac{\partial F_1(\mathbf{x})}{\partial y_D} & \dfrac{\partial F_1(\mathbf{x})}{\partial V_{D3}^{(NL)}} & \dfrac{\partial F_1(\mathbf{x})}{\partial V_{D1}^{(NL)}} \\[2mm] \dfrac{\partial F_2(\mathbf{x})}{\partial x_D} & \dfrac{\partial F_2(\mathbf{x})}{\partial y_D} & \dfrac{\partial F_2(\mathbf{x})}{\partial V_{D3}^{(NL)}} & \dfrac{\partial F_2(\mathbf{x})}{\partial V_{D1}^{(NL)}} \\[2mm] \dfrac{\partial F_3(\mathbf{x})}{\partial x_D} & \dfrac{\partial F_3(\mathbf{x})}{\partial y_D} & \dfrac{\partial F_3(\mathbf{x})}{\partial V_{D3}^{(NL)}} & \dfrac{\partial F_3(\mathbf{x})}{\partial V_{D1}^{(NL)}} \\[2mm] \dfrac{\partial F_4(\mathbf{x})}{\partial x_D} & \dfrac{\partial F_4(\mathbf{x})}{\partial y_D} & \dfrac{\partial F_4(\mathbf{x})}{\partial V_{D3}^{(NL)}} & \dfrac{\partial F_4(\mathbf{x})}{\partial V_{D1}^{(NL)}} \end{bmatrix} \tag{20}$$

The strategy adopted in this paper was to combine the Newton's method applied to the system [Eqs. (12), (13), (17) and (18)] with the unconstrained problem of minimizing the objective function $\mathbf{F}$:

$$\min_{x \in \mathbb{R}^n} \mathbf{F} : \mathbb{R}^n \to \mathbb{R} \tag{21}$$

In unconstrained optimization, the most widely used function to be minimised (also known as merit function) is a scalar-valued function of $\mathbf{F}$, i.e. the squared norm of $\mathbf{F}$:

$$g(\mathbf{x}) = \frac{1}{2} \|\mathbf{F}(\mathbf{x})\|^2 = \frac{1}{2} \mathbf{F}(\mathbf{x}) \cdot \mathbf{F}(\mathbf{x}) \tag{22}$$

where the factor 1/2 is introduced for convenience. The unconstrained algorithm chosen was a line search method because of its simplicity. It consists in using only a fraction of the Newton step:

$$\mathbf{x}^{n+1} = \mathbf{x}^n + \lambda^n \partial \mathbf{x}^n \qquad 0 < \lambda \leq 1 \tag{23}$$

where λ is called step length. The strategy for reducing λ guarantees that the Newton step is not too large and is performed through a *polynomial backtracking line search method* [24]. This procedure allows obtaining a very robust algorithm since it requires little computational time (less than 1 sec) and it is able to converge from almost any guess point.

5. Experimental Set-Up

The algorithm for the damage detection was experimentally validated on a carbon fibre–reinforced plastic (CFRP) composite panel [290x290 mm], made of 25 layers with [0, 90, 0, 90, 0] fibre orientation. A barely visible impact damage (BVID) was

generated by a low-velocity impact at the energy of 12 J. The geometry of the specimen is shown in Figure (6).

Table 1. Receiver sensors coordinates.

Sensor	x coordinate (mm)	y coordinate (mm)
1	263.5	143
2	263	123
3	29	140
4	29	120
5	39	130
6	253	133

Figure 6. Experimental Set-Up.

Six piezoelectric sensors (AmericanPiezo transducers with a central frequency of 330 kHz) were surface bonded on the composite structure as shown in Figure (6) and their positions are reported in Table 1, considering the bottom left corner of the plate as origin of the xOy reference frame.

Ultrasonic bursts of 200 cycles with phases of 0 and 180 degrees were used to excite the specimen at multiple frequencies. The responses of these excitations were then measured with a sampling frequency of 10MHz. Due to the difficulty in accurately triggering the acquisition of numerous independent excitation signals and the importance of correctly determining the ToA of these signals with respect of one another, an algorithm was implemented in Matlab to align any two signals of opposite phase. The implemented algorithm shifted (in time) one of the two experimental data sets in order to minimise the sum of the two signals (i.e. $y_{PSA}(t) \cong \min[(y(t)|_{\varphi=0} + y(t)|_{\varphi=\pi})/2]$. This method ensured that the phase shift between any two signals would be as close to 180 degrees regardless of the triggering of the

equipment. The signal generator (TTI 50 MHz Pulse Generator T6501) was linked to an amplifier (Falco Systems DC 5 MHz High Voltage WMA-300). The received signals were recorded with a Pico Scope instrument (PICO TECHNOLOGY pc oscilloscope 100V max input, Model 4424).

The damage location algorithm was performed using a Matlab code as post-processing manipulation of the recorded signals and the computational time was less than 1 sec.

6. Experimental Results

As shown in Section 5, the signals were managed through the piezoelectric sensors and then they were Hilbert transformed in order to obtain the envelopes [Figure (2)]. The PSA was used on the envelopes for filtering the outputs [Figure (3)] and the AIC method was exploited to calculate the ToA of the signals [Figure (4)]. Finally, the damage detection algorithm, shown in Section 4, was performed. In order to find the optimal second order harmonic response on the damaged composite plate, a series of ultrasonic sweeps between 150 and 500 kHz with a frequency step of 70 Hz was sent. Such a frequency range was tuned to find local maxima in the second order nonlinear response of the sample. The highest maximum value was achieved at the fundamental frequency of 318.95 kHz [Figure (7)].
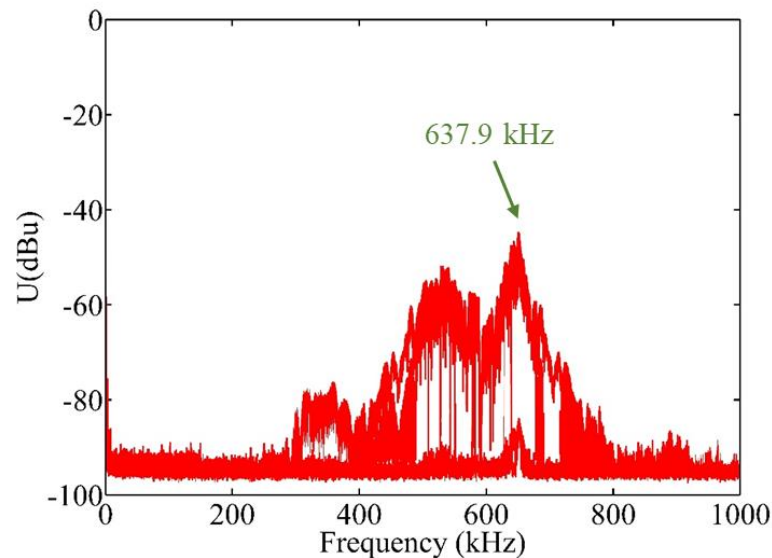
Figure 7. Sweep plot after damage.

The nonlinear wave velocities and the damage location coordinates are shown in Table 2. The extimated point showed the presence of an error expressed by the following formula:

56

$$\Psi = \sqrt{(x_{real} - x_{calculated})^2 + (y_{real} - y_{calculated})^2} \tag{24}$$

where (x_{real}, y_{real}) are the coordinates of the real damaged position and ($x_{calculated}$, $y_{calculated}$) are the coordinates of the calculated one. As shown in Figure (8), the result was very close to the reality (the error Ψ was ~ 5 mm).

Table 2. True and Calculated damage position and nonlinear group velocities.

	True	Calculated
x_D (mm)	120	120
y_D (mm)	130	125
$V_{D3}^{(NL)}$ (m/s)	n/a	2880
$V_{D1}^{(NL)}$ (m/s)	n/a	3139
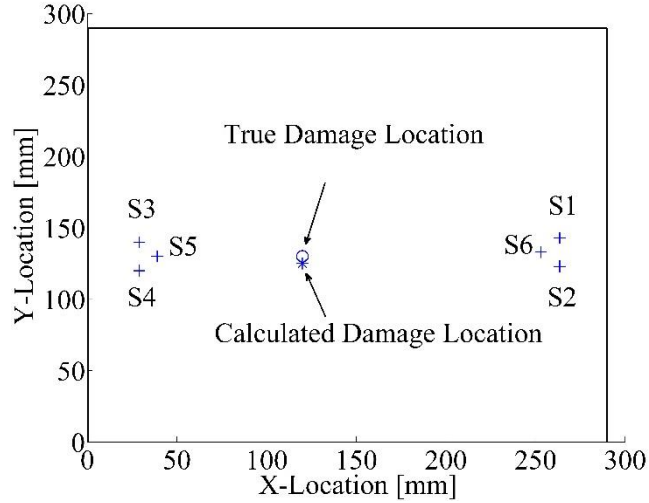
Figure 8. Damage Localisation.

7. Conclusions

This paper proposed, for the first time, an ultrasonic nonlinear time domain method for damage detection and localisation in a composite plate-like structure. This methodology is based on the ToA estimation of the second order nonlinear response measured by six surface attached acoustic emission PZT receiver sensors. The acquired waveforms were first Hilbert transformed and then filtered at the second harmonic using the PSA method. The AIC method was then used to estimate the arrival times of the nonlinear waveforms originated by the damage. The coordinates of the defect location were obtained by solving a system of nonlinear equations, which was solved via a combination of Newton's iterative method and unconstrained

57

optimisation. To validate this methodology, experimental tests were performed on a damaged quasi-isotropic CFRP composite panel with delamination. The results showed that the damage location was found with satisfactory accuracy at the driving frequency of 319.85 kHz, with a maximum location error of ~5 mm. The proposed method, in contrast to previous damage localisation algorithms, does not require a priori knowledge of the anisotropy group velocities of the propagating waveforms, as well as the structural lay-up and thickness.

References

[1] Kessler, S., Spearing ,M., Soutis, C., *Damage Detection in Composite Materials using Lamb Wave Methods*. Proceedings of the American Society for Composites, 2001.

[2] Mal, A.K, Ricci, F., Gibson, S., Banerjee, S., *Damage detection in structures from vibration and wave propagation data*. Smart Nondestructive Evaluation and Health Monitoring of Structural and Biological Systems II, 2003 **202**.

[3] Hall, J.S. and Michaels, J.E., *Multipath ultrasonic guided wave imaging in complex structures*. Structural Health Monitoring 2015 **1–14**.

[4] Michaels, J.-E., Michaels, T.-E., *Guided wave signal processing and image fusion for in situ damage localization in plates*. Wave Motion 2007 **44**: pp. 482-492.

[5] Michaels, J.-E., Michaels, T.-E., *Damage Localization in Inhomogeneous Plates Using a Sparse Array of Ultrasonic Transducers*. AIP Conference Proceedings, 2007 **894**: pp. 846-853.

[6] Gao, H., Shi, Y., Rose, J. *Guided wave tomography on an aircraft wing with leave in place sensors*. AIP Conf. Proc., 2005 **760**: pp. 1788-1794.

[7] Flynn, E.B., Todd, M.D., Wilcox, P.D., Drinkwater, B.W., and Croxford, A.J., *Maximum-likelihood estimation of damage location in guided-wave structural health monitoring*. Proceedings of the Royal Society A: Mathematical, Physical and Engineering Sciences, 2011. **467**(2133): pp. 2575-2596.

[8] Velsor, J.K. Van, Gao, H., Rose, J.L., *Guided-wave tomographic imaging of defects in pipe using a probabilistic reconstruction algorithm*. Insight - Non-Destructive Testing and Condition Monitoring, 2007 **49**(9): pp. 532-537.

[9] Yu, L., Giurgiutiu, V., *In situ 2-D piezoelectric wafer active sensors arrays for guided wave damage detection*. Ultrasonics, 2008 **48**: pp. 117–134.

[10] Purekar, A.S. and Pines, D.J., *Damage Detection in Thin Composite Laminates Using Piezoelectric Phased Sensor Arrays and Guided Lamb Wave Interrogation*. Journal of Intelligent Material Systems and Structures, 2001 **21**.

[11] Landau, L.D., Lifshitz, E. M., *Theory of Elasticity*, *Chap. III*. Pergamon, 1986, Oxford.

[12] Meo, M., Polimeno, U., Zumpano, G., *Detecting Damage in Composite Material Using Nonlinear Elastic Wave Spectroscopy Methods*. Applied Composite Materials, 2008. **15**(3): pp. 115-126.

[13] Zumpano, G., Meo, M., *Damage localization using transient non-linear elastic wave spectroscopy on composite structures*. International Journal of Non-Linear Mechanics. International Journal of Non-Linear Mechanics, 2008. **43**(3): pp. 217-230.

[14] Van Den Abeele, K.E.-A., Van de Velde, K., Carmeliet, J., *Inferring the degradation of pultruded composites from dynamic nonlinear resonance measurements*. Polym. Compos. 2001. **22**: pp. 555–567.

[15] Nagy, P.-B., Adler, L., *Acoustic nonlinearity in plastics*. In Thompson, D. O., Chimenti, D. E. (eds.) Review of Progress in Quantitative Nondestructive Evaluation, 1992. Plenum, New York **I IB**: pp. 2025–2032.

[16] Ciampa, F., Pickering, S., Scarselli, G., Meo, M., and Kundu, T., *Nonlinear damage detection in composite structures using bispectral analysis.* 2014. **9064**: pp. 9064-02.

[17] Chen, J., Hagiwara, I., Su, X. and Shi, Q., *A Bispectrum Feature Extraction Enhanced Structure Damage Detection Approach.* JSME International Journal, 2002. **45**(1).

[18] Ciampa, F., Scarselli, G. and Meo, M., *Nonlinear Imaging Method Using Second Order Phase Symmetry Analysis and Inverse Filtering.* Journal of Nondestructive Evaluation, 2015. **34**(2).

[19] Ciampa, F. and Meo, M., *Nonlinear elastic imaging using reciprocal time reversal and third order symmetry analysis.* J Acoust Soc Am, 2012. **131**(6): pp. 4316-23.

[20] Sedlak, P., Y. Hirose, M. Enoki, and J. Sikula, *Arrival time detection in thin multilayer plates on the basis of akaike information criterion.* J. Acoustic Emission, 2008. **26**: p. 6.

[21] General Radio Company, *The frequency spectrum of a tone burst.* Instrument Notes, 1965 **IN-105**.

[22] Bussang, J.J., Ehrman, L. and Graham, J.W., *Analysis of nonlinear systems with multiple inputs.* Proc. IEEE, 1974 **62**: pp. 1088–1119.

[23] Ciampa, F., Meo, M., *Acoustic emission source localization and velocity determination of the fundamental mode A0 using wavelet analysis and a Newton-based optimization technique.* Smart Mater. Struct., 2010 **19**.

[24] Dennis, J. E. and Schnabel, R. B., *Numerical Methods for Unconstrained Optimization and Nonlinear Equations.* Prentice-Hall, Englewood Cliffs, NJ, 1983.

Chapter 4

Frequency domain nonlinear parameters for damage localisation in composite materials

4.1 Motivation: overcoming time of arrival estimation inaccuracies

Chapter 3 showed a technique which allows damage localisation in composite structures through the time of arrival estimation of the nonlinear ultrasonic response. However, time of arrival estimation techniques, such as Akaike method, may lack of accuracy when applied to low amplitude waveforms leading to unsteadiness in damage localisation. Although this unsteadiness can be mitigated by performing several experiments and averaging the results, this problematic was the drive towards a new damage localisation technique, which does not rely on time of arrival estimations. Working in frequency domain was considered to be the right alternative to time calculations and, thus, the following studies were focused on the conception of a damage localisation technique based on nonlinear parameters extracted from ultrasonic wave spectra.

4.2 Summary: damage localisation via nonlinear parameters from frequency domain

The aim of this stage of the project was the introduction and development of a novel in-situ nonlinear ultrasonic approach for the localisation of micro-damage in composite components. The technique, called nonlinear elastic multi-path reciprocal (NEMR) method, works through a sparse array of N surface bonded sensors which are used to transmit and receive ultrasonic waves in a composite plate-like structure with impact damage. This novel method introduced a reciprocal relationship based on the assumption that, due to attenuation, the closer the receiving sensor is to damage, the higher will be the acquired second order nonlinear response. Hence, considering a suitable Cartesian reference frame xOy, the closest point to damage along the path between multiple transmitter-receiver pairs (x_{Dij}, y_{Dij}) was calculated as follows:

$$x_{D_{ij}} = x_i - \frac{\xi_i}{\xi_i + \xi_j}\left(x_i - x_j\right)$$

(4.1)

$$y_{D_{ij}} = y_i - \frac{\xi_i}{\xi_i + \xi_j}\left(y_i - y_j\right)$$

(4.2)

where i and j identify the transmitting and receiving sensor, respectively, ξ identifies the nonlinear coefficient and (x, y) are the coordinates of the sensor. By finally considering all the possible paths between multiple transducers pairs, damage coordinates were calculated as follows:

$$x_D = \frac{1}{Q}\left[\sum_{\substack{i,j \\ i \neq j}} x_{D_{ij}}\right] \qquad y_D = \frac{1}{Q}\left[\sum_{\substack{i,j \\ i \neq j}} y_{D_{ij}}\right]$$

(4.3)

where $Q = N(N-1)/2$ is the number of possible paths between reciprocal transducers. Following the studies showed in Chapter 2, a normalised version of the second order nonlinear parameter β was introduced to take into account material attenuation and initially considered as the nonlinear input ξ. However, this parameter, called $\bar{\beta}$, relies on magnitude ratios and discards all phase information contained in the acquired waveforms. Bispectral analysis was used as an alternative to the second order nonlinear coefficient [22]. In this case, the phase relation of frequency components, called quadratic phase coupling (QPC), allows the identification of structural nonlinearity by discarding the signal noise that, differently, is not quadratic phase

coupled. The bispectrum was replaced by its normalised non-dimensional counterpart, the bicoherence coefficient b^2.

4.3 Results: damage localisation at different signal-to-noise ratios

The second order harmonic response was initially found by using an ultrasonic sweep with a frequency range between 150 and 500 kHz and a frequency step of 70 Hz. The highest nonlinear responses were achieved at the fundamental frequencies of 218.5 kHz and 318.95 kHz. These frequencies were then selected to transmit ultrasonic bursts. The signal-to-noise-ratio (SNR) evaluated in the recorded structural responses at the input frequencies of 218.5 kHz and 318.95 kHz, was ~11.2 dB and ~1.8 dB, respectively. Using the normalised nonlinear second order parameter $\bar{\beta}$ as algorithm input, the most accurate damage localisation (maximum error of ~13 mm) was achieved with a SNR of ~11.2 dB at the driving frequency of 218 kHz. Conversely, by using the bicoherence parameter b^2, the most accurate result (maximum error of ~14.4 mm) was achieved in the case of higher noise (SNR = ~1.8 dB) with a driving frequency of 318 kHz. Hence, bicoherence, taking into account phase information, resulted to be more sensitive to nonlinearities discriminating the material nonlinear features with respect to both experimental and environmental noise sources. Since the impact energy in composites produces a delamination all around the impact point, the accuracy of this method can be considered more than satisfactory even though it does not require a priori knowledge of structural properties.

4.4 Paper: nonlinear elastic multi-path reciprocal method for damage localisation in composite materials

The proposed damage localisation method, details of data collection, experiments and results were published by the journal Ultrasonics [67]. The Statement of Authorship Form and the paper are shown in next pages.

This declaration concerns the article entitled:								
Nonlinear elastic multi-path reciprocal method for damage localisation in composite materials								

Publication status (tick one)								
draft manuscript		**Submitted**		**In review**		**Accepted**		**Published**	X

Publication details (reference)	Boccardi, S., Callá, D.B., Ciampa, F. and Meo, M., 2018. Nonlinear elastic multi-path reciprocal method for damage localisation in composite materials. Ultrasonics, 82, pp.239-245.
Candidate's contribution to the paper (detailed, and also given as a percentage).	The candidate contributed to/ considerably contributed to/predominantly executed the… Formulation of ideas: 60% I proposed the idea of multi-path approach and how to use it to find damage location. My supervisor proposed the idea of proportional attenuation of the nonlinear material responses. Design of methodology: 95% I designed the methodology by creating a script able to implement the proposed technique. My co-authors contributed to the mathematical formulation. Experimental work: 90% I carried out all the experiments, implemented and performed the method in post-process. My co-authors collected most of data. Presentation of data in journal format: 95% I decided the structure, collated data, wrote all drafts, prepared all figures and responded to reviews. My supervisor provided feedback on drafts and helped with publication process.
Statement from Candidate	This paper reports on original research I conducted during the period of my Higher Degree by Research candidature.
Signed	Date 04/06/2019

Nonlinear Elastic Multi-Path Reciprocal Method for Damage Localisation in Composite Materials

S. Boccardi, D.B. Callá, F. Ciampa, M. Meo

Department of Mechanical Engineering, University of Bath, Bath BA2 7AY, UK

Abstract

Nonlinear ultrasonic techniques rely on the measurement of nonlinear elastic effects caused by the interaction of ultrasonic waves with the material damage, and have shown high sensitivity to detect micro-cracks and defects in the early stages. This paper presents a nonlinear ultrasonic technique, here named *nonlinear elastic multi-path reciprocal* method, for the identification and localisation of micro-damage in composite laminates. In the proposed methodology, a sparse array of surface bonded ultrasonic transducers is used to measure the second harmonic elastic response associated with the material flaw. A reciprocal relationship of nonlinear elastic parameters evaluated from multiple transmitter-receiver pairs is then applied to locate the micro-damage. Experimental results on a damaged composite panel revealed that an accurate damage localisation was obtained using the normalised second order nonlinear parameter with a high signal-to-noise-ratio (~11.2 dB), whilst the use of bicoherence coefficient provided high localisation accuracy with a lower signal-to-noise-ratio (~1.8 dB). The maximum error between the calculated and the real damage location was nearly 13 mm. Unlike traditional linear ultrasonic techniques, the proposed *nonlinear elastic multi-path reciprocal* method allows detecting material damage on composite materials without a priori knowledge of the ultrasonic wave velocity nor a baseline with the undamaged component.

Keywords

1. Introduction

In the last decade, carbon fibre–reinforced plastic (CFRP) composite materials have been increasingly used in different sectors, from aerospace to automotive and civil, due to their good in-plane mechanical and lightweight properties. However, composites are susceptible to low velocity impacts that can generate barely visible impact damage (BVID), micro-cracks and delamination, which can irreparably affect the integrity of the structure. In particular, if the impact occurs at very low velocity, damage can be a mixture of splitting between fibres, matrix cracking, fibres fracture and internal delamination due to inter-laminar shear and tension. These damaged modes weaken the mechanical properties of the structure and can be completely invisible when viewed from the external impacted surface. Hence, both linear and nonlinear ultrasonic structural health monitoring (SHM) techniques based on sparse transducer arrays have been developed in the last few years to provide an early warning and increase of safety of composite components [1-6]. Linear beamforming techniques, such as the statistical maximum-likelihood estimation [7] and the reconstruction algorithm for probabilistic inspection of damage (RAPID) [8] have shown a high level of accuracy for the detection and localisation of damage in composites. However, linear ultrasonic techniques typically rely on the measurement of wave scattering and reflections, as well as changes of macroscopic elastic features caused by the presence of damage such as wave attenuation and group velocity. Hence, these methodologies may lack of sensitivity to micro-flaws due to low acoustic impedance mismatch at damage location. Moreover, linear ultrasonic methodologies with sparse transducer arrays require the knowledge of waveforms associated to the undamaged component, which is generally difficult to obtain.

On the other hand, ultrasonic waves propagating in a damaged structure at a particular driving frequency can generate "clapping" motion of the region normal to the crack interfaces or nonlinear friction (rubbing) between the defect surfaces excited by small tangential stresses. This result in the creation of nonlinear elastic effects such as higher harmonics and sub-harmonics of the excitation frequency, which can be used as signature for micro-damage detection. A number of authors have recently focused their studies on the nonlinear behaviour of ultrasonic waves in composites, both numerically and experimentally [9, 10]. Typically, both the second and third order nonlinear elastic responses are used for material damage identification and localisation [11]. Ciampa et

al. [12, 13] and Malfense-Fierro and Meo [14] use the second order harmonic response and nonlinear inverse filtering technique in order to detect damage in multi-layered media.

This paper presents a novel in-situ nonlinear ultrasonic approach, here called nonlinear elastic multi-path reciprocal (NEMR) method, for the localisation of micro-damage in composite components. A sparse array of surface bonded ultrasonic transducers is here used to measure the second harmonic nonlinear elastic response associated with the material damage by means of the normalised classical second order nonlinear coefficient and the bicoherence parameter. The micro-damage localisation is then achieved by analysing the reciprocal relationship of these nonlinear coefficient calculated from multiple transmitter-receiver pairs. The paper is outlined as follows: in Section 2 there is an introduction to the nonlinear parameters involved; in Section 3 the NEMR technique is explained in detail; Section 4 shows the experimental set-up; in Section 5 it is possible to read the experimental results; in Section 6 the main conclusions are discussed.

2. Nonlinear Parameters

According to Section 1, both micro-cracks and delamination, when excited by ultrasonic waves can generate nonlinear material responses. These elastic effects can be analytically modelled by using the classical nonlinear elasticity (CNE) theory [15]. Assuming a one-dimensional longitudinal wave propagation along the x-direction, the elastodynamic wave equation [16] can be expressed as the power series of the strain $\varepsilon_x = \partial u(x,t)/\partial x$ as follows

$$\rho \frac{\partial^2 u(x,t)}{\partial t^2} = \frac{\partial \sigma}{\partial x} = (\lambda + 2\mu) \left[\frac{\partial}{\partial x} \left(1 + \beta \varepsilon_x + \delta {\varepsilon_x}^2 \right) \varepsilon_x \right] \tag{1}$$

where σ is the stress and β and δ are second and third order elastic coefficients, respectively. The second order nonlinear parameter β is typically two or three order of magnitude higher than γ and it can be used as a reliable signature for damage detection. Equation (1) is generally solved via a perturbation theory that leads to the following expression of the nonlinear parameter β:

$$\beta = \frac{8A_2}{A_1^2 x k^2} \tag{2}$$

In Eq. (2), A_1 and A_2 are the fundamental and the second harmonic amplitudes, respectively, k is the wave number and x is the propagation distance of the propagating waveform from the nonlinear source (i.e. damage location). The second order nonlinear parameter β is a material property (it is constant all over the material) and its formulation [Eq. (2)] is obtained by assuming no material attenuation. To overcome this limitation, in this paper a normalised version of β is used, here defined as $\bar{\beta}$, which is only function of the fundamental and second harmonic amplitudes and may change from point to point within the medium, with the highest value at the damage location. This new normalised second order nonlinear coefficient $\bar{\beta}$ is defined as follows:

$$\bar{\beta} = \frac{A_2}{A_1} = \sqrt{\frac{|P(2\omega_1)|}{|P(\omega_1)|}} \tag{3}$$

where $|P(\omega_1)|$ and $|P(2\omega_1)|$ are the magnitudes of the power spectral densities associated with the fundamental angular frequency ω_1 and the second harmonic angular frequency $2\omega_1$. However, $\bar{\beta}$ relies on magnitude ratios and discards all phase information contained in the acquired waveforms. Higher order statistics (HOS), such as the bispectral analysis, are a valid alternative to the second order nonlinear coefficient as they can be used to measure both the magnitude and phase of the higher order harmonic frequency components [17]. Particularly, the bispectrum B is the two-dimensional Fourier Transform of the third order correlation function and, for a real, zero-mean stationary random process $s(t)$, it is given by:

$$B(\omega_m, \omega_n) = \iint\limits_{-\infty}^{+\infty} R_{sss}(\tau_1, \tau_2) e^{j(\omega_m \tau_1 + \omega_n \tau_2)} d\tau_1 d\tau_2 \tag{4}$$

where $R_{sss}(\tau_1, \tau_2)$ is the third order auto-correlation function of $s(t)$. In the frequency domain, Eq. (4) can be rewritten as:

$$B(\omega_m, \omega_n) = \mathrm{E}[S(\omega_m)S(\omega_n)S^*(\omega_m + \omega_n)] \tag{5}$$

where $S(\omega)$ is the Fourier Transform of the measured signal $s(t)$ and the asterisk sign "*" corresponds to a complex conjugate operation. The three frequency components ω_n, ω_m and $\omega_n + \omega_m$ have a special phase relation, called quadratic phase coupling (QPC) [17], which defined as follows:

$$\varphi_m + \varphi_n = \varphi_{m+n} \tag{6}$$

where φ_n and φ_m are the phases of the signal at frequencies ω_n and ω_m, respectively, and φ_{m+n} is the phase of the signal at frequency $\omega_n + \omega_m$. QPC allows the identification of structural nonlinearity by discarding the signal noise that, differently, is not quadratic phase coupled [18]. Similarly to the second order nonlinear parameter β, also the bispectrum B can be replaced by its normalised non-dimensional counterpart, the bicoherence coefficient b^2, which is defined as follows [17]:

$$b^2 = \frac{|B(\omega_1, \omega_1)|^2}{P(\omega_1)P(\omega_1)P(2\omega_1)} \tag{7}$$

with $B(\omega_m, \omega_n) = \mathrm{E}[S(\omega_m)S(\omega_n)S^*(\omega_m + \omega_n)]$ the bispectrum calculated at the fundamental frequency ω_1. The NEMR damage localisation technique will use either the coefficient $\bar{\beta}$ or b^2 as input and is reported in next Section.

3. Nonlinear Multi-Path Reciprocal (NEMR) method

The NEMR method allows the estimation of damage location on composite panels. A number N of ultrasonic sensors is surface bonded on a composite plate-like structure with impact damage. The NEMR technique is based on the assumption that the closer the receiving sensor is to damage, the higher will be the acquired second order nonlinear response. Hence, a reciprocal relationship is here introduced in order to retrieve the closest point to damage along the path between multiple transmitter-receiver pairs.
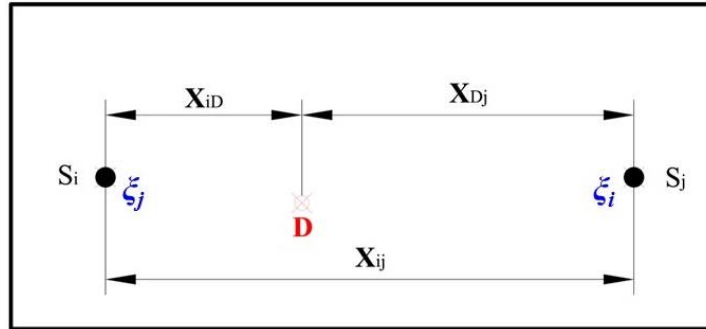
Figure 1. Scheme for a couple of sensors and relative wave path.

According to Figure 1, X_{ij} is the distance between two sensors S_i and S_j, and the sensor-damage distances are X_{iD} and X_{Dj} with $i,j = 1, 2, \ldots, N$. The reciprocal relationship between each sensor-damage path and the associated ultrasonic nonlinear response is given by:

$$X_{iD} = \frac{X_{Dj}\xi_i}{\xi_j} \tag{8}$$

In Eq. (8), the parameter ξ was used to identify either the normalised second order nonlinear coefficient $\bar{\beta}$ or the bicoherence b^2. By substituting the total distance X_{ij} in Eq. (8), the distance between the sensor S_i and the point closest to damage, D_{ij}, is:

$$X_{iD} = \frac{X_{ij}\xi_i}{\xi_j + \xi_i} \tag{9}$$

Similarly, the reciprocal distance between the sensor S_j and the damage is:

$$X_{Dj} = \frac{X_{ij}\xi_j}{\xi_j + \xi_i} \tag{10}$$

The transducers-damage distances can be geometrically considered as the radii of circumferences located in a Cartesian reference frame xOy with the origin at the bottom left corner of the panel. The damage location on each single path can be calculated as the intersection point of two tangent circumferences as follows:

$$(x - X_i)^2 + (y - Y_i)^2 = r_{iD} \tag{11}$$

where $r_{iD} = X_{iD}$.

Substituting Eq. (9) into (11), yields:

$$(x - X_i)^2 + (y - Y_i)^2 = \left(\frac{X_{ij}\xi_i}{\xi_j + \xi_i}\right)^2 \tag{12}$$

For each pair of transmitter-receiver transducer, it is now possible to calculate the coordinates x_{Dij} and y_{Dij} associated with the damage location as follows

$$x_{D_{ij}} = x_i - \frac{\xi_i}{\xi_i + \xi_j}(x_i - x_j) \tag{13a}$$

$$y_{D_{ij}} = y_i - \frac{\xi_i}{\xi_i + \xi_j}(y_i - y_j) \tag{13b}$$

By finally considering all the possible paths and tangent circumferences between multiple transducers pairs, damage coordinates can be calculated as follows:

$$x_D = \frac{1}{Q}\left[\sum_{\substack{i,j \\ i \neq j}} x_{D_{ij}}\right] \qquad\qquad y_D = \frac{1}{Q}\left[\sum_{\substack{i,j \\ i \neq j}} y_{D_{ij}}\right] \tag{14}$$

where $Q = N(N-1)/2$ is the number of possible paths between reciprocal transducers. Figure 2 shows an example of the NEMR image with multiples paths and tangential circumferences for two pairs of transducers.
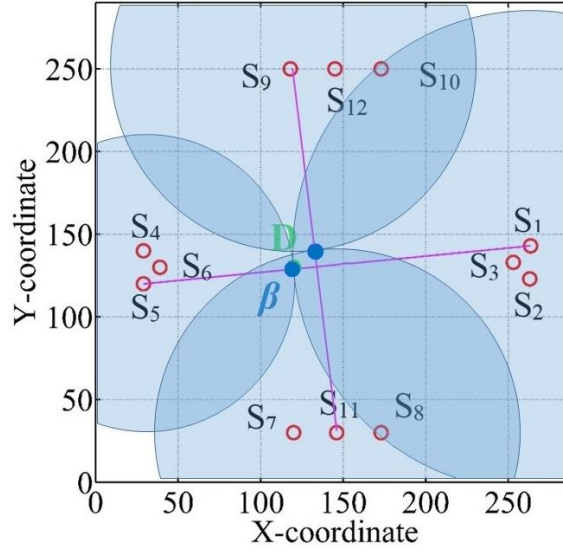
Figure 2. Example of tangent circumferences in NEMR method for two pairs of transducers.

4. Experimental Set-up

The NEMR algorithm for damage localisation, introduced in Section 3, was experimentally validated on a composite panel with dimensions 290 x 290 x 3 mm, made of twenty-five layers of prepreg T800-M21 (see Table 1) with a stacking sequence of $[(0/90)_6/\overline{0}]_s$. In order to obtain barely visible impact damage, a low-velocity impact at the energy of 12 J was applied on the panel (Figure 3). Twelve surface bonded piezoelectric sensors (AmericanPiezo transducers with a central frequency of 330 kHz) were placed on the specimen as shown in Figure 4 and their positions are reported in Table 2. Ultrasonic bursts of 200 cycles were used to excite the specimens at multiple frequencies (Figure 5). The responses of these excitations were then measured with a sampling frequency of 10 MHz. The signal generator (TTI 50 MHz Pulse Generator T6501) was linked to an amplifier (Falco Systems DC 5 MHz High Voltage WMA-300) and the received signals were recorded with a Pico Scope instrument (Pico Technology pc oscilloscope 100V max input, Model 4424).

Table 1. M21/T800 prepreg sheet properties.

Properties	Value
Young's modulus	$E_{11} = 157$ GPa
	$E_{22} = E_{33} = 8.5$ Gpa
Poisson's ratio	$\nu_{12} = 0.35$
Shear modulus	$G_{12} = 4.5$ Gpa

Table 2. Piezoelectric sensors coordinates on the composite plate

Sensor	x coordinate (mm)	y coordinate (mm)
1	263.5	143
2	263	123
3	253	130
4	29	140
5	29	120
6	39	130
7	120	30
8	173	30
9	118	250
10	173	250
11	146	30
12	145	250
Dam.	120	130
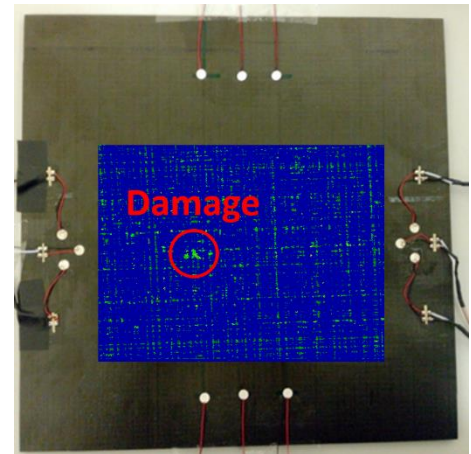
Figure 3. C-Scan of the panel after impact. Damage is barely visible.
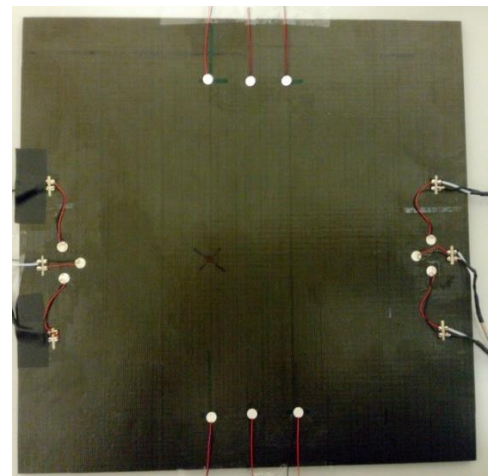
Figure 4. Composite plate experimental set-up.

It should be noted that the transmitted frequency plays an important role in NEMR method since the most accurate results are achieved when the damaged region is vibrating so that nonlinear material response is high enough to display harmonic frequencies. The NEMR damage location algorithm was performed using a Matlab code as post-processing manipulation of the recorded signals.

5. Experimental Results

The second order harmonic response was initially found by using an ultrasonic sweep with a frequency range between 150 and 500 kHz and a frequency step of 70 Hz. The highest nonlinear responses were achieved at the fundamental frequencies of 218.5 kHz and 318.95 kHz (Figure 6). These frequencies were then selected to transmit ultrasonic bursts as in Section 4. A representative ultrasonic wave response using a burst input signal is shown in Figure 5.
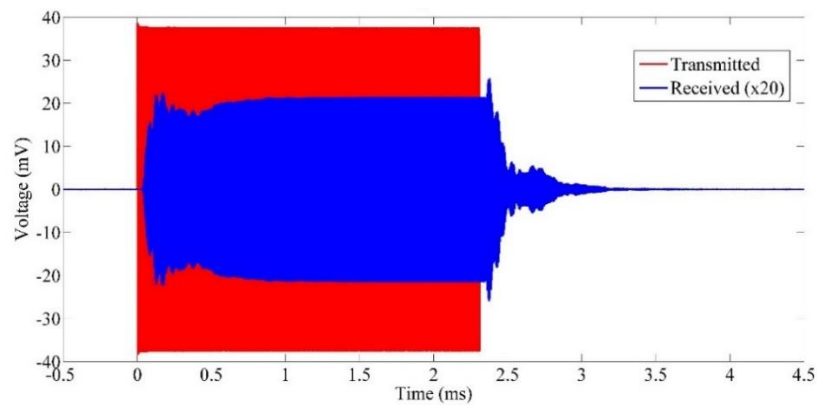
Figure 5. Ultrasonic burst (red line) sent at 218.5 kHz and received response (blue line).
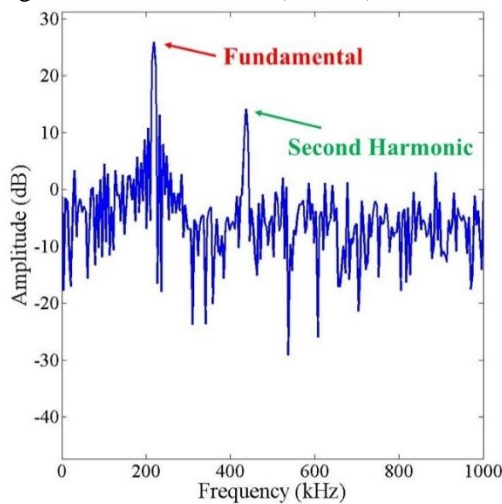
Figure 6a. Spectrum of a received signal (input at a frequency of 218.5 kHz).
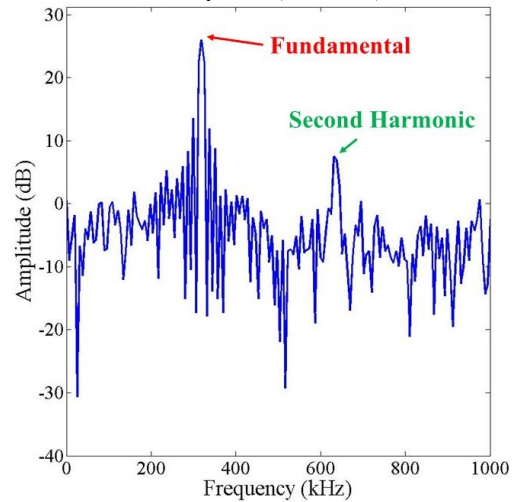
Figure 6b. Spectrum of a received signal (input at a frequency of 318.95 kHz).

The signal-to-noise-ratio (SNR) evaluated in the recorded structural responses at the input frequencies of 218.5 kHz and 318.95 kHz was ~11.2 dB and ~1.8 dB, respectively. SNR, the ratio of the power of the signal (meaningful information) and the power of background noise (unwanted signal), was calculated through the

MATLAB function *"snr"*. The error ψ between the calculated and the real damage position was found through the following equation:

$$\psi = \sqrt{\left(x_{real} - x_{calculated}\right)^2 + \left(y_{real} - y_{calculated}\right)^2} \tag{15}$$

The different SNR affected the damage localisation results and it was analysed with the NEMR method. Using the normalised nonlinear second order parameter $\bar{\beta}$ as algorithm input, the most accurate damage localisation was achieved with a SNR of ~11.2 dB at the driving frequency of 218 kHz. Conversely, by using the bicoherence parameter b^2, the most accurate result was achieved in the case of higher noise (SNR = ~1.8 dB) with a driving frequency of 318 kHz. This was in accordance with Section 2 since bicoherence allowed the detection of damage nonlinearities even in the presence of elevated level of noise due to QPC. Hence, according to Eqs. (13), the damage closest point D_{ij} was calculated on the path between each pair of sensors and two locations were found: one with the $\bar{\beta}$ parameter and the other with the bicoherence b^2, respectively (Figures 7-10).
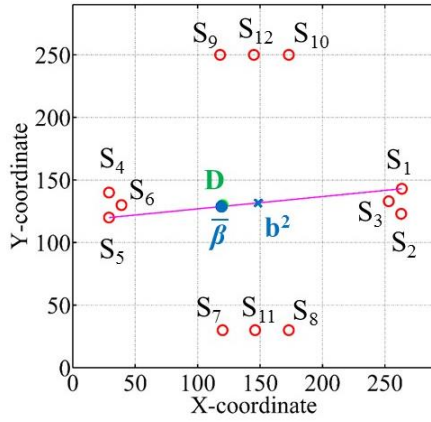
Figure 7. Reciprocal relationship applied to a horizontal path with a frequency of 218.5kHz.
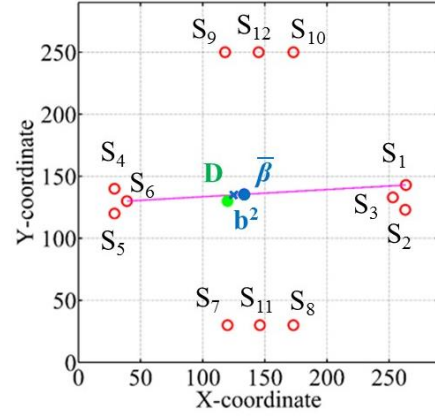
Figure 8. Reciprocal relationship applied to a horizontal path with a frequency of 318.95 kHz.

Figure 7 shows an example of horizontal path between sensors S_1 and S_5 (hollow circles) where the use of nonlinear parameter $\bar{\beta}$ resulted in a more accurate damage localisation (full dark circles) with an error ψ of nearly 2 mm [see Eq. (15)]. In Figure 8, instead, the bicoherence parameter b^2 was the best option (x signs, ψ ~6 mm). Even when the damage was not located along the straight line between the transmitter and receiver transducers, as in the vertical paths of Figure 9 and 10, the NEMR technique

73

was able to find the coordinates closest to damage location (i.e. the errors were ~30 mm and ~24 mm, respectively).
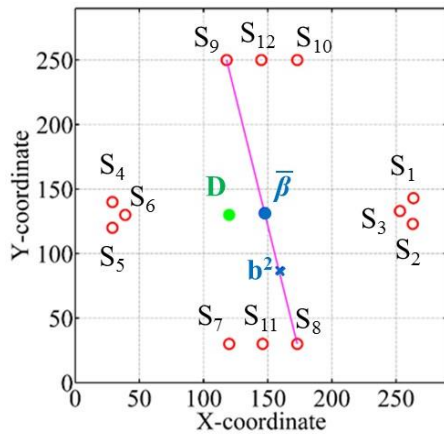
Figure 9. Reciprocal relationship applied at vertical path n°12 at frequency 218.5 kHz.
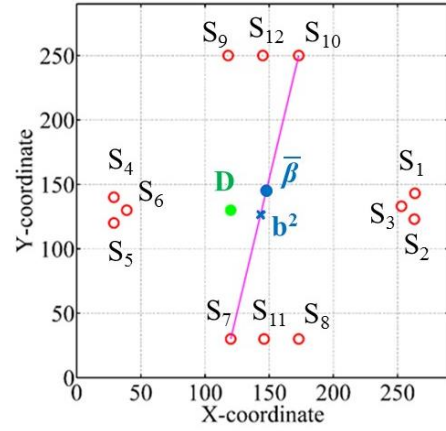
Figure 10. Reciprocal relationship applied at vertical path n°11 at frequency 318.95 kHz.

Figure 11 shows the results by using 218.5 kHz as transmitting frequency where the closest values to the damaged region were those relative to $\bar{\beta}$.
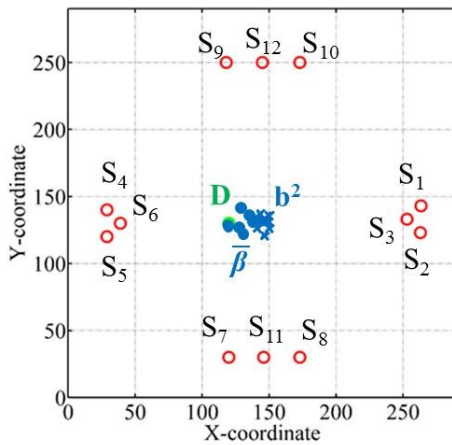
Figure 11. NEMR best values with 218.5 kHz as transmitting frequency.
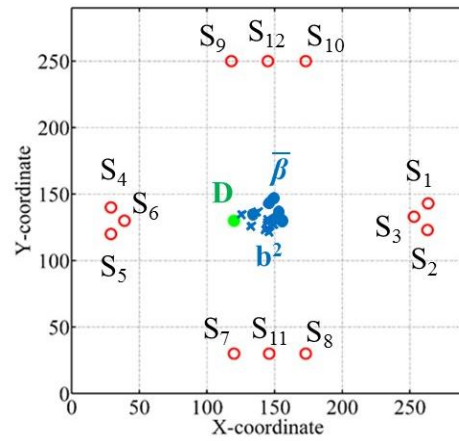
Figure 12. NEMR best values with 318.95 kHz as transmitting frequency.

In Figure 12, the best results were obtained by considering 318.95 kHz as transmitting frequency and the most accurate damage localisation was achieved through the bicoherence b^2. According to Section 3, once all coordinates were calculated on each single path, Eq. (14) was used to reveal the actual damage location. Eq. (14) was performed a second time excluding the results from the paths in which $d_{D_{ij}} > 3\sigma$

where $d_{D_{ij}} = \sqrt{\left(x_{D_{ij}} - x_D\right)^2 + \left(y_{D_{ij}} - y_D\right)^2}$ and $\sigma = \sqrt{\frac{1}{Q}\sum_{\substack{i,j \\ i \neq j}} d_{D_{ij}}^2}$. Hence, the

damage position was identified for all nonlinear responses (see Figure 13 and 14) and the results showed a maximum error of ~13 mm for the frequency of 218.5 kHz with $\bar{\beta}$ and ~14.4 mm for the frequency of 318.95 kHz with b^2. These results are more than satisfactory even though this technique does not use any baseline and does not need a priori knowledge of the wave velocity.
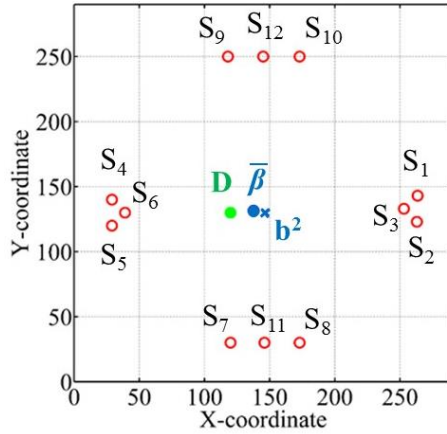
Figure 13. NEMR method damage positions at frequency 218.5 kHz.
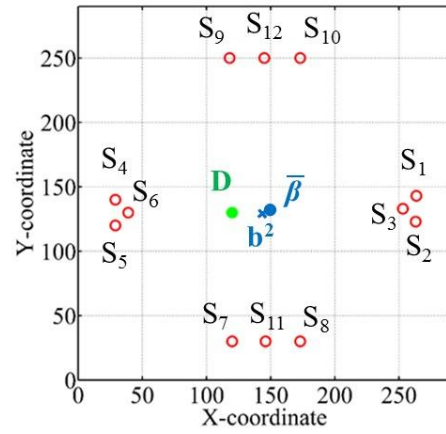
Figure 14. NEMR method damage positions at frequency 318.95 kHz.

6. Conclusions

In this paper, a novel nonlinear damage localisation technique was presented. It allows damage localisation on composite structures by sending and receiving an ultrasonic signal from a number of surface bonded sensors placed close to the edge of a panel. Opposite sensors are coupled and the point closest to damage is found on the path between them through a reciprocal relationship involving the nonlinear parameters β and B (see Section 2 and 3). Finally, the damage location is found by considering the calculated positions on every path and discarding the worst cases. The second parameter is more sensitive to nonlinearities since it takes in account the quadratic phase coupling effect at the second harmonic. This information is useful to discriminate the material nonlinear features with respect to both experimental and environmental noise sources. The proposed method was experimentally validated on a damaged anisotropic plate-like structure that presented different fibre orientations,

thus various attenuation effects of the original wave with respect to the path angle. During the experimental validation, the two nonlinear parameters were replaced by their corresponding dimensionless coefficients, i.e. the normalised second order nonlinear parameter $\bar{\beta}$ and the bicoherence b^2. Experimental results demonstrated that the anisotropy and different wave attenuations on the structure did not affect damage localisation. Surely, the technique requires a distribution of sending and receiving sensors able to cover the delaminated area. The results showed that an accurate damage localisation was achieved through $\bar{\beta}$ when the SNR was higher (SNR = 11.2 dB at a transmitting frequency of 218.5 kHz) whilst the use b^2 of was useful when the SNR was lower (SNR = 1.8 at a frequency of 318.95 kHz). The maximum error between the calculated and the impact locations was ~13 mm. Since the impact energy in composites produces a delamination all around the impact point, the accuracy of this method can be considered more than satisfactory even though, in contrast to previous damage localisation algorithms, it does not require a priori knowledge of structural lay-up and thickness, as well as group velocities of the propagating waveforms.

References

[1] Yu, L. and V. Giurgiutiu, In situ 2-D piezoelectric wafer active sensors arrays for guided wave damage detection. Ultrasonics, 2008. **48**(2): p. 117-134.

[2] Kessler, S.S., S.M. Spearing, and C. Soutis, Damage detection in composite materials using Lamb wave methods. Smart Materials and Structures, 2002. **11**(2): p. 269.

[3] Mal, A.K., F. Ricci, S. Gibson, and S. Banerjee. Damage detection in structures from vibration and wave propagation data. in NDE for Health Monitoring and Diagnostics. 2003. International Society for Optics and Photonics.

[4] Antonucci, V., M. Ricciardi, F. Caputo, A. Langella, V. Lopresto, V. Pagliarulo, A. Rocco, C. Toscano, P. Ferraro, and A. Riccio, Non destructive techniques for the impact damage investigation on carbon fibre laminates. Procedia Engineering, 2014. **88**: p. 194-199.

[5] Pagliarulo, V., A. Rocco, A. Langella, A. Riccio, P. Ferraro, V. Antonucci, M. Ricciardi, C. Toscano, and V. Lopresto, Impact damage investigation on composite laminates: comparison among different NDT methods and numerical simulation. Measurement Science and Technology, 2015. **26**(8): p. 085603.

[6] Riccio, A., F. Caputo, G. Di Felice, S. Saputo, C. Toscano, and V. Lopresto, A joint numerical-experimental study on impact induced intra-laminar and inter-laminar damage in laminated composites. Applied Composite Materials, 2016. **23**(3): p. 219-237.

[7] Flynn, E.B., M.D. Todd, P.D. Wilcox, B.W. Drinkwater, and A.J. Croxford. Maximum-likelihood estimation of damage location in guided-wave structural health monitoring.

in Proceedings of the Royal Society of London A: Mathematical, Physical and Engineering Sciences. 2011. The Royal Society.

[8]   Tabtabaeipour, M., J. Hettler, S. Delrue, and K. Van Den Abeele. Reconstruction Algorithm for Probabilistic Inspection of Damage (RAPID) in Composites. in 11th European Conference on Non-Destructive Testing (ECNDT 2014). 2014.

[9]   Boccardi, S., D.-B. Calla, G.-P.M. Fierro, F. Ciampa, and M. Meo. Nonlinear damage detection and localization using a time domain approach. in SPIE Smart Structures and Materials+ Nondestructive Evaluation and Health Monitoring. 2016. International Society for Optics and Photonics.

[10]   Fierro, G.M., F. Ciampa, D. Ginzburg, E. Onder, and M. Meo, Nonlinear ultrasound modelling and validation of fatigue damage. Journal of Sound and Vibration, 2015. **343**: p. 121-130.

[11]   Ciampa, F., G. Scarselli, S. Pickering, and M. Meo, Nonlinear elastic wave tomography for the imaging of corrosion damage. Ultrasonics, 2015. **62**: p. 147-155.

[12]   Ciampa, F., G. Scarselli, and M. Meo, Nonlinear imaging method using second order phase symmetry analysis and inverse filtering. Journal of Nondestructive Evaluation, 2015. **34**(2): p. 1-6.

[13]   Ciampa, F., E. Barbieri, and M. Meo, Modelling of multiscale nonlinear interaction of elastic waves with three-dimensional cracks. The Journal of the Acoustical Society of America, 2014. **135**(6): p. 3209-3220.

[14]   Fierro, G.P.M. and M. Meo, Nonlinear imaging (NIM) of flaws in a complex composite stiffened panel using a constructive nonlinear array (CNA) technique. Ultrasonics, 2017. **74**: p. 30-47.

[15]   Ostrovsky, L. and P. Johnson, Dynamic nonlinear elasticity in geomaterials. Rivista del nuovo cimento, 2001. **24**(7): p. 1-46.

[16]   Guyer, R.A. and P.A. Johnson, Nonlinear mesoscopic elasticity: Evidence for a new class of materials. Physics today, 1999. **52**: p. 30-36.

[17]   Ciampa, F., S. Pickering, G. Scarselli, and M. Meo. Nonlinear damage detection in composite structures using bispectral analysis. in SPIE Smart Structures and Materials+ Nondestructive Evaluation and Health Monitoring. 2014. International Society for Optics and Photonics.

[18]   Ciampa, F., S.G. Pickering, G. Scarselli, and M. Meo, Nonlinear imaging of damage in composite structures using sparse ultrasonic sensor arrays. Structural Control and Health Monitoring, 2016.

Chapter 5

Frequency domain nonlinear parameters for damage imaging in composite materials

5.1 Motivation: from nonlinear damage localisation to nonlinear damage imaging

Chapter 4 showed a technique which allows damage localisation in composite structures through nonlinear ultrasonic response evaluated in frequency domain. Once achieved accurate and reliable damage localisation in composite materials, the next step was to go beyond localisation and create an image of the damaged region. More information was necessary in order to obtain this result. The idea was to transmit, in the scanned structure, a frequency sweep instead of a single frequency ultrasonic wave so that the structural response is spread across frequency windows. Hence, a new technique, based on the nonlinear response to a frequency sweep sent in a damaged structure, was developed in order to achieve nonlinear damage imaging in composite structures for aerospace applications.

5.2 Summary: ultrasonic frequency sweeps and statistical approach for nonlinear damage imaging

NEMR technique [67], showed in Chapter 4, was considered as a baseline for a new method, called nonlinear elastic multi-path imaging (NEMI). As well as its predecessor, the proposed technique works through a sparse array of N surface bonded sensors which are used to transmit and receive ultrasonic waves in a composite plate-like structure with impact damage. As NEMR method, NEMI technique applies a reciprocal relationship along the path between transmitter-receiver pairs in order to localise the point closest to damage D_{ij} [67]. Introducing a suitable Cartesian reference frame xOy, the coordinates of point D_{ij} (x_{Dij}, y_{Dij}) were calculated for each transmitter-receiver pair:

$$x_{Dij} = x_i - \frac{\eta_i}{\eta_i + \eta_j}\left(x_i - x_j\right) \tag{5.1}$$

$$y_{Dij} = y_i - \frac{\eta_i}{\eta_i + \eta_j}\left(y_i - y_j\right) \tag{5.2}$$

where i and j identify the transmitting and receiving sensor, respectively, η identifies the nonlinear coefficient and (x, y) are the coordinates of the sensor. These relationships accept nonlinear responses in place of the parameter η of eqs. (5.1) and (5.2). In NEMI technique, a single frequency ultrasonic wave was combined to a frequency sweep in order to obtain, in addition to the second harmonic generation, the modulated responses of the damaged specimen.
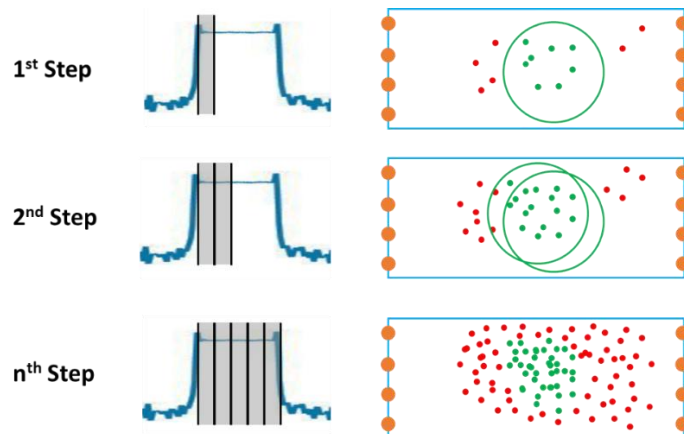
Figure 5.1. NEMI statistical process. At each step, all the points closest to damage from each sensor-to-sensor path are used to create a circle having its centre on the average point position and the standard deviation as radius. All the points outside this circle are excluded.

The response frequency bands were split in a number of sub-windows (Figure 5.1) which were analysed individually. The acoustic moment [see eq (5.3)], introduced to evaluate the energy of each sub-window, was calculated and used as input of the reciprocal relationship.

$$\eta = \int_{\omega_0}^{\omega_0 + \Delta\omega} P(\omega) d\omega \tag{5.3}$$

where ω_0 is the initial angular frequency, $\Delta\omega$ is the width of the integration window and $P(\omega)$ is the power spectral density [27]. A cloud of estimated damage locations D_{ij} was generated and refined via a statistical approach which allowed the removal of wrongly located points due to instrumentation faults. Finally, each acoustic moment value was assigned to its respective point D_{ij} and an image of the damaged region was generated.

5.3 Results: modulation bands compared to second harmonic window as nonlinear input

NEMI method was performed on a region of a stiffened composite specimen. A 50% threshold was used to evaluate damaged areas (estimated, $S_{calculated}$, and real, S_{real}) so that the results could be compared to a classical C-scan. The accuracy of the technique was quantified through two error functions:

$$\Psi_{LOC} = \sqrt{(x_{calculated} - x_{real})^2 + (y_{calculated} - y_{real})^2} \tag{5.4}$$

$$\Psi_{AREA} = \left(1 - \frac{S_{calculated} \cap S_{real}}{S_{calculated}}\right) \times 100\% \tag{5.5}$$

where Ψ_{LOC} is the distance between the centre of the real damaged area, (x_{real}, y_{real}), and the centre of the estimated damaged area, $(x_{calculated}, y_{calculated})$, and represents the error in calculating damage location whilst Ψ_{AREA} is the percentage of calculated area that does not overlap the real damaged area, used to evaluate the error in calculating damage area imaging. The transmitted double frequency signal was composed of a continuous signal at a frequency of 155 kHz and a sweep having a frequency between 185 kHz and 195 kHz. First, the second harmonic window of the ultrasonic sweep was used to extrapolate the nonlinear inputs of the technique. Then, modulation bands were considered as nonlinear inputs of the method. The results showed how the introduction of modulated responses led to a general improvement of damage imaging.

Table 5.1. NEMI localisation and area errors using different nonlinear parameters.

Nonlinear Parameter	Localisation error ξ_{LOC} (mm)	Area error ξ_{AREA} (%)
Second harmonic	6.3	21
Low modulation band	1.8	6
High modulation band	3.2	29
Average of modulation bands	1.3	13

5.4 Paper: nonlinear elastic multi-path reciprocal imaging for damage localisation in composite materials

The proposed damage imaging method, details of data collection, experiments and results are currently in draft format and will soon be submitted for publication. The Statement of Authorship Form and the paper are shown in next pages.

This declaration concerns the article entitled:								
Nonlinear elastic multi-path reciprocal imaging for damage localisation in composite materials								

Publication status (tick one)								
draft manuscript	X	**Submitted**		**In review**		**Accepted**		**Published**
Publication details (reference)	N/A							
Candidate's contribution to the paper (detailed, and also given as a percentage).	The candidate contributed to/ considerably contributed to/predominantly executed the… Formulation of ideas: 90% I proposed the idea of statistical approach for damage imaging. My supervisor proposed the idea of nonlinear modulation as input of the technique. Design of methodology: 100% I designed the methodology by creating a script able to implement the proposed technique. Experimental work: 90% I carried out all the experiments, implemented and performed the method in post-process. My co-authors helped me with data collection. Presentation of data in journal format: 95% I decided the structure, collated data, wrote all drafts, prepared all figures and responded to reviews. My co-authors provided feedback on drafts and helped with publication process.							
Statement from Candidate	This paper reports on original research I conducted during the period of my Higher Degree by Research candidature.							
Signed	*Beccard Salvatore*					**Date**	04/06/2019	

Nonlinear damage imaging in composite materials using a multi-path reciprocal method

Salvatore Boccardi, Gian Piero Malfense Fierro, Michele Meo

Department of Mechanical Engineering, University of Bath, Claverton Down BA2 7AY, UK

Abstract

Nonlinear ultrasonic methods measure nonlinear elastic effects caused by the interaction of ultrasonic waves with material damage and show high sensitivity in detecting micro-cracks and defects in the early stages. This paper presents a nonlinear ultrasonic method, here named nonlinear elastic multi-path imaging, which allows the imaging of damage in composite structures. In the proposed methodology a sparse array of surface bonded ultrasonic transducers were used to evaluate the second harmonic and modulated elastic responses from a damaged medium, in this case a complex composite stiffened panel with barely visible impact damage (BVID). The points closest to damage are found on the paths between transmitter-receiver pairs through a reciprocal relationship of nonlinear elastic parameters and a statistical approach was used to select the cloud of point so that a 2D image of the damaged region is created. Experimental results revealed that the second order nonlinear parameter provided accurate damage localisation and imaging and the use of modulation bands further improved imaging accuracy and damage localisation. The maximum error between the calculated and the real damage area centres was only 1.3 mm. The proposed nonlinear elastic multi-path imaging technique, unlike traditional linear ultrasonic methods, provides an image of structural damage on composite materials without *a priori* knowledge of the ultrasonic wave velocity nor a baseline with the undamaged component.

Keywords

Composite materials, Structural health monitoring (SHM), Nonlinear damage imaging, Nonlinear Ultrasound, Ultrasound Array, Baseline-Free, Impact Damage, Nonlinear imaging, Modulation, Nonlinear Modulation

1. Introduction

In the last two decades, carbon fibre–reinforced plastic (CFRP) composite materials have been increasingly used in the aerospace sector due to their lightweight and good in-plane properties. However, low velocity impacts can affect composite structural integrity as they can generate barely visible impact damage (BVID), micro-cracks and delamination. These damage modes result in a weakening of the mechanical properties of the structure which can be totally invisible when observed from the external impacted surface. Hence, in the last few years, the development of ultrasonic structural health monitoring (SHM) techniques based on *in situ* sparse transducer arrays for early damage detection have improved the safety of composite materials [1][2]. Linear methods, such as the reconstruction algorithm for probabilistic inspection of damage (RAPID) [3] and the statistical maximum-likelihood estimation [4], have shown a high level of accuracy for the detection and localisation of damage in composites. Linear ultrasonic techniques depend on the measurement of changes of macroscopic elastic features due to damage, such as wave attenuation and group velocity, and, thus, are sensitive to gross defects or open cracks, where there is an effective barrier to transmission (requiring a large impedance miss-match). However, this is a limit as these methods are less sensitive to micro-cracks and small delamination. Furthermore, linear ultrasonic methodologies with sparse transducer arrays require *a priori* knowledge of waveforms associated to the undamaged component, which are generally difficult to obtain. Conversely, when excited with ultrasonic waves, micro-cracks and delamination can generate ''clapping" or "rubbing" of the crack interfaces that lead to nonlinear elastic effects such as higher harmonics and modulation, which can be used as signature for damage detection and imaging. In particular, nonlinear modulation occurs when two sinusoidal signals at distinctive frequencies are propagating through a media that has a nonlinear mechanism such as a crack; the mixing of these two propagating waves produces spectral sidebands at the sum and difference between the two frequencies. Lately, the nonlinear behaviour of ultrasonic

waves in composite materials has been the main topic of SHM [5][6][7]. Usually, the second order nonlinear elastic response is used for material damage localisation [8][9][10]. Some authors have also considered nonlinear structural responses as sources for damage imaging techniques [11][12][13] even if this technology can still be considered at an early stage. However, second order nonlinear responses can be generated laboratory instrumentation which, if not previously calibrated, can disturb the measurements leading to wrong results. Recently, several authors, such as Malfense-Fierro and Meo [14], in order to detect damage in multi-layered media, have focused their studies on the modulation effect as it is not affected by instrumentation noise. In this paper, modulation effects are used to improve an existing technique proposed by Boccardi et al., called nonlinear elastic multi-path reciprocal (NEMR) technique [15]. This method was able to localise micro-damage in composite components through a sparse array of surface bonded ultrasonic transducers used to measure the second harmonic nonlinear elastic response associated with the material damage. Although NEMR method was demonstrated to be a reliable and accurate damage localisation technique, it relies on second and higher nonlinear harmonic responses and does not allow damage size estimation.

In this paper, a novel nonlinear ultrasonic structural health monitoring (SHM) technique, here called nonlinear elastic multi-path imaging (NEMI) method, is introduced as a natural development of NEMR technique. A sparse array of surface bonded ultrasonic transducers is used to measure the nonlinear elastic responses associated with the material damage. A statistical calculation, applied to the reciprocal relationship of these nonlinear contributions calculated from multiple transmitter-receiver pairs, allows 2-D damage imaging on composite components without *a priori* knowledge of structural properties. Hence, the proposed technique allows *both* damage localisation *and* imaging.

The paper is outlined as follows: in section 2 the nonlinear parameters involved are introduced and the NEMI method is explained in detail; section 3 shows the experimental set-up; in section 4 it is possible to read the experimental results; in section 5 the main conclusions are discussed.

2. Nonlinear damage imaging for structural health monitoring

2.1 Nonlinear elasticity theory

According to section 1, composite materials can be affected by contact-type defects, such as micro-cracks and delamination. This kind of defects can be easily understood by introducing a two-dimensional simple model of a contact-type interface (figure 1a) between two rough elastic surfaces [16]. When a stress is applied, the deformation of two opposite sides of the interface (here defined as U_+ and U_-) leads to a change of contact area, generating a nonlinear elastic behaviour. Considering $\varepsilon = U_+ - U_-$ as the variation of thickness of the interface, the internal stress $\Delta\sigma$ can be expressed as a nonlinear spring whose stiffness parameter K is proportional to ε so that $K = K(\varepsilon)$ [16]. The expression of the internal stress $\Delta\sigma$ can be obtained from the spring model by expanding K in a Taylor series approximated to the first order:

$$\Delta\sigma = K\varepsilon = (K_0 + \lambda\varepsilon)\varepsilon = K_0\varepsilon + \lambda\varepsilon^2 \tag{1}$$

where K_0 and λ are the linear and nonlinear coefficients, respectively. Analysing the interaction of longitudinal ultrasonic waves transmitted along the x-direction (figure 1a) of the composite component, the presence of a defect can be assessed. Thus, a single frequency input wave $u_{SF}(x,z,t)$ is defined as:

$$u_{SF}(x, z, t) = U(x,z)\cos(\omega t) \tag{2}$$

where $U(x,z)$ is the amplitude of the deformation, $\omega = 2\pi f$ is the angular frequency, f is the frequency and t is the time. The effective thickness of the crack D is changed by the ultrasonic wave and the variation ε can be expressed as:

$$\varepsilon = D\frac{\partial u_{SF}}{\partial x} = D\frac{\partial U}{\partial x}\cos(\omega t) \tag{3}$$

Substituting eq. (3) into eq. (1) leads to:

$$\Delta\sigma = A_0 + A_1\cos(\omega t) + A_2\cos(2\omega t) \tag{4}$$

where

$$A_1 = K_0 D\frac{\partial U}{\partial x} \qquad \text{and} \qquad A_0 = A_2 = \frac{\lambda D^2}{2}\left(\frac{\partial U}{\partial x}\right)^2 = \frac{\lambda}{2K_0}A_1^{\,2} \tag{5}$$

Eq. (4) shows how the defect transforms part of the transmitted wave into a nonlinear wave having double of the input frequency (2ω). This is the second order harmonic and its amplitude A_2 can be used as an indication of the presence of a crack. If the

transmitted ultrasonic wave has two driving frequencies, in addition to the second harmonic generation, there is another phenomenon, called modulation. A double frequency input wave $u_{DF}(x,z,t)$ can be defined as:

$$u_{DF}(x,z,t) = U_1(x,z)\cos(\omega_1 t) + U_2(x,z)\cos(\omega_2 t) \tag{6}$$

where $U_1(x,z)$ and $U_2(x,z)$ are the amplitudes of the deformation due to the excitation at angular frequencies ω_1 and ω_2, respectively. At this point, the variation of thickness ε can be now expressed as:

$$\varepsilon = D\frac{\partial u_{DF}}{\partial x} = D\frac{\partial U_1}{\partial x}\cos(\omega_1 t) + D\frac{\partial U_2}{\partial x}\cos(\omega_2 t) \tag{7}$$

The internal stress for this case can now be defined by substituting eq. (7) into eq. (1):

$$\begin{aligned}
\Delta\sigma = A_{0,0} &+ A_{1,0}\cos(\omega_1 t) + A_{0,1}\cos(\omega_2 t) + A_{2,0}\cos(2\omega_1 t) \\
&+ A_{0,2}\cos(2\omega_2 t) + A_{1,-1}\cos[(\omega_1 - \omega_2)t] \\
&+ A_{1,1}\cos[(\omega_1 + \omega_2)t]
\end{aligned} \tag{8}$$

where

$$A_{0,0} = \frac{\lambda D^2}{2}\left[\left(\frac{\partial U_1}{\partial x}\right)^2 + \left(\frac{\partial U_2}{\partial x}\right)^2\right] \quad , \qquad
\begin{aligned}
A_{1,1} = A_{1,-1} &= \lambda D^2 \left(\frac{\partial U_1}{\partial x}\right)\left(\frac{\partial U_2}{\partial x}\right) \\
&= \frac{\lambda}{K_0{}^2} A_{1,0} A_{0,1}
\end{aligned}$$

$$A_{1,0} = K_0 D\left(\frac{\partial U_1}{\partial x}\right) \quad , \qquad A_{0,1} = K_0 D\left(\frac{\partial U_2}{\partial x}\right) \tag{9}$$

$$A_{2,0} = \frac{\lambda D^2}{2}\left(\frac{\partial U_1}{\partial x}\right)^2 = \frac{\lambda}{2K_0} A_{1,0}{}^2 \quad \text{and} \quad A_{0,2} = \frac{\lambda D^2}{2}\left(\frac{\partial U_2}{\partial x}\right)^2 = \frac{\lambda}{2K_0} A_{0,1}{}^2$$

Eq. (8) highlights all the nonlinear parts of the ultrasonic wave due to the presence of the defect. As mentioned before, when a dual frequency ultrasonic wave is transmitted into a damaged medium, each driving frequency leads to a second harmonic component (having amplitude $A_{2,0}$ and $A_{0,2}$) and, in addition, two nonlinear modulated responses are generated at the combination frequencies $\omega_1 \pm \omega_2$. Both the amplitudes $A_{1,1}$ and $A_{1,-1}$ of the modulated terms can be used to assess the presence of a defect. Since $\lambda \ll K_0$, the second order harmonic amplitudes $A_{2,0}$ and $A_{0,2}$ are higher than the modulated responses $A_{1,1}$ and $A_{1,-1}$ (see eqs. (9)) and are usually preferred as nonlinear source for SHM techniques [8][9]. However, second order harmonics can also be generated by the transmitting instrumentation so that the nonlinear response contains combinations of structural responses and instrumentation noise. Modulated components, even if very small, are not affected by the instrumentation noise and can be considered as a more reliable nonlinear source. In order to allow a higher energy

distribution to the modulated bands (figure 1b), the double frequency signal can be created by adding a continuous wave to a sweep. The energy of both the second harmonic and modulated windows can be analysed using the acoustic moment α that can be introduced as [17]:

$$\alpha = \int_{\omega_0}^{\omega_0 + \Delta\omega} P(\omega)d\omega \tag{10}$$

where ω_0 is the initial angular frequency, $\Delta\omega$ is the width of the integration window and $P(\omega)$ is the power spectral density.
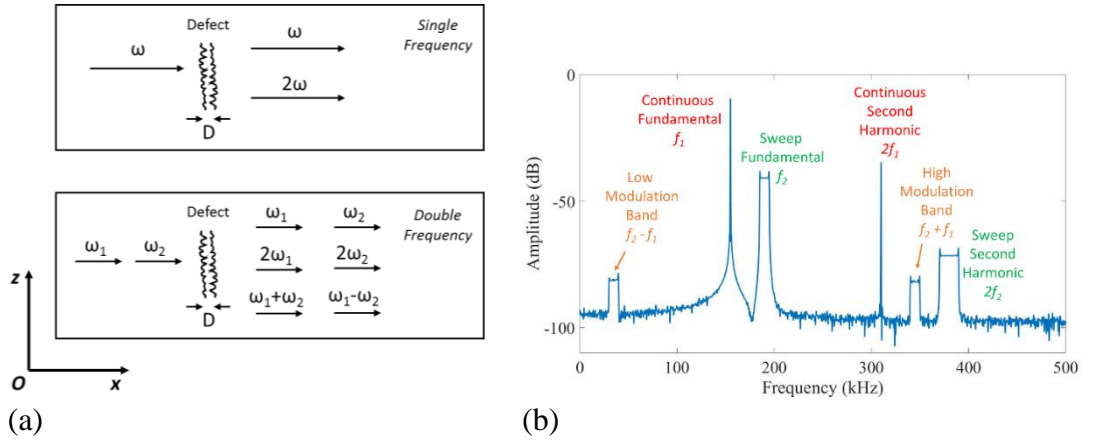
Figure 1. (a) Wave interactions due to the presence of a defect; (b) example of an expected received signal in frequency domain.

2.2 *Nonlinear elastic multi-path imaging (NEMI)*

The nonlinear elastic multi-path imaging (NEMI) method is based on the nonlinear elastic multi-path reciprocal (NEMR) method [15] (briefly described in section 1) and allows the imaging of damage on composite panels. A number N of ultrasonic transducers is placed on a composite plate-like structure with impact damage so that a scanning window is created around the damaged region (figure 2a). As NEMR method, NEMI technique assumes that, due to attenuation, the closer the receiving sensor is to damage, the higher the nonlinear response. Hence, along the path between transmitter-receiver pairs, the point closest to damage (here named point D, see figure 2a) can be localised through a reciprocal relationship [15]. Considering the path between sensor i and sensor j (having length L_{ij}), the distance between point D and sensors i and j (L_{iD} and L_{Dj}, respectively) can be calculated as follows [15]:

$$L_{iD} = \frac{L_{ij}\alpha_i}{\alpha_i + \alpha_j} \qquad \text{and} \qquad L_{Dj} = \frac{L_{ij}\alpha_j}{\alpha_i + \alpha_j} \tag{11}$$

where α_i and α_j are the nonlinear responses received by sensor i and sensor j, respectively. Introducing a Cartesian reference frame xOy with origin at the bottom left of the scanning window (see figure 2a), the coordinates of point D (x_{Dij}, y_{Dij}) can be calculated for each transmitter-receiver pair:
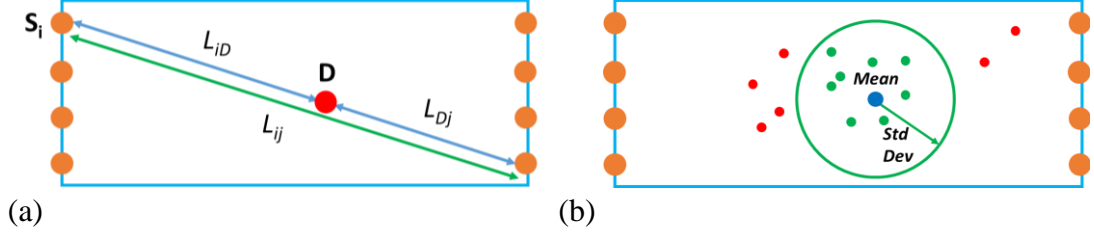
Figure 2. (a) NEMI distance notation in the scanning window and (b) NEMI statistical approach.

$$x_{Dij} = x_i - \frac{L_{iD}}{L_{ij}}(x_i - x_j) = x_i - \frac{\alpha_i}{\alpha_i + \alpha_j}(x_i - x_j) \tag{12a}$$

$$y_{Dij} = y_i - \frac{L_{iD}}{L_{ij}}(y_i - y_j) = y_i - \frac{\alpha_i}{\alpha_i + \alpha_j}(y_i - y_j) \tag{12b}$$

where (x_i, y_i) and (x_j, y_j) are the coordinates of sensor i and j, respectively. According to section 2, either second harmonic or modulation response can be used in place of α as input of NEMI method. Eqs. (12) find the point closest to damage on a single sensor-to-sensor path. Thus, when the nonlinear parameter α is set, the number of D points $n_{D\alpha}$ corresponds to the number of paths between sensor pairs and, if N sensors are placed on the scanned panel, $n_{D\alpha}$ can be calculated as follows:

$$n_{D\alpha} = \frac{N!}{2!\,(N-2)!} \tag{13}$$

If the transmitted signal includes a sweep, the damaged structure will distribute energy to known frequency bands such as the second harmonic and, if the wave has two driving frequencies, high and low modulation (see section 2.1 and figure 1b). Once the frequency band is chosen, it can be split in k smaller windows on which the acoustic moment integration can be applied to calculate the nonlinear input parameter α. Hence, there will be $n_{D\alpha}$ points for each window, leading to a total number of D points n_D that can be expressed as:

$$n_D = k\frac{N!}{2!\,(N-2)!} \tag{14}$$

A statistical approach introduced in order to discard points D that are wrongly located due to instrumentation faults. At each frequency window, all the point D positions are

used to create a circular area built by considering their average as a centre $C_\alpha = (x_{C\alpha}, y_{C\alpha})$ and their standard deviation as a radius r_α as follows (figure 2b):

$$x_{C\alpha} = \frac{1}{n_{D\alpha}} \sum_{i=1}^{N} \sum_{j=1}^{i-1} x_{Dij}$$

$$x_{STD\alpha} = \sqrt{\frac{1}{n_{D\alpha}} \sum_{i=1}^{N} \sum_{j=1}^{i-1} (x_{Dij} - x_{C\alpha})^2}$$

$$y_{C\alpha} = \frac{1}{n_{D\alpha}} \sum_{i=1}^{N} \sum_{j=1}^{i-1} y_{Dij} \quad \text{where}$$

$$y_{STD\alpha} = \sqrt{\frac{1}{n_{D\alpha}} \sum_{i=1}^{N} \sum_{j=1}^{i-1} (y_{Dij} - y_{C\alpha})^2}$$

$$r_\alpha = \sqrt{x_{STD\alpha}^2 + y_{STD\alpha}^2}$$

(15)

All the points D outside this circle are discarded. Likewise, another circular area is created from all the averaged C_α points and, if a C_α point is outside the circle, all the points related to its frequency window are discarded. After this process, the output is a cloud of points placed in a smaller region that includes damage. Finally, considering each path of the remaining points D, the mean value of the nonlinear contributions α_i and α_j is assigned to the corresponding point D so that an image of damage can be created (figure 3).
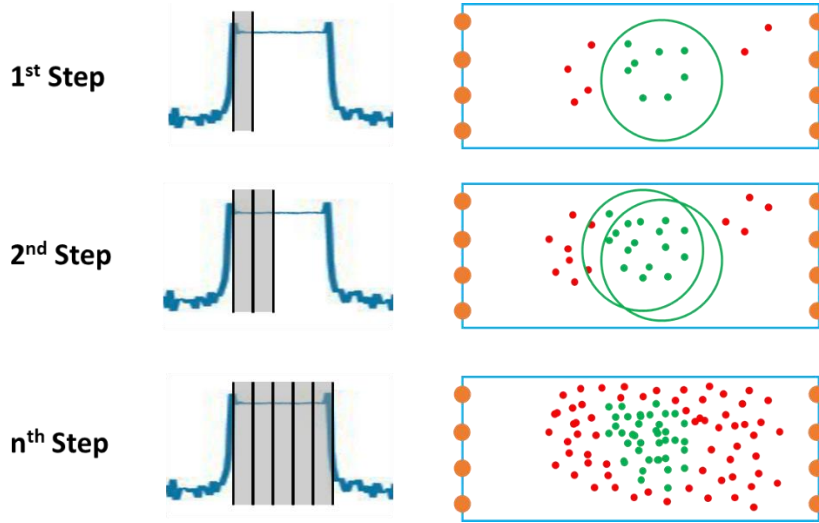
Figure 3. NEMI statistical process.

3. Experimental set-up

The NEMI algorithm for damage imaging, introduced in section 2.2, was experimental validated on an aerospace component. The specimen was an 80 cm x 57.5 cm x 0.5 cm composite curved panel with an unknown lamination sequence, reinforced by three stiffeners and having barely visible damage in three different points (figure 4a). The algorithm was applied on a 14 cm x 30 cm scanning window set between two stiffeners

and containing one of the impacted points (C dashed circle in figure 4a). A number of ultrasonic waves were transmitted and received through McWade Acoustic Emission Sensors (dimension of 2 cm x 2.3 cm x 1 cm) having a central frequency of 150 kHz that were placed on two opposite sides of the scanning window (sensor coordinates in table 1). Transducers and sensors were coupled to the sample using ultrasound gel and connected to a National Instruments device used to generate the input signals and capture the received signals (NI PXI-5105 as a waveform generator and NI PXI-5421 as a receiver). A Falco Systems DC 5 MHz High Voltage (WMA-300) amplifier was used to amplify the driving signals whilst a McWade pre-amplifier was introduced to enhance receiving sensor outputs. Three different ultrasonic bursts (time length of 30 ms and amplitude of 300 V peak to peak) were transmitted from each sensor location and received on the opposite side of the scanning region (figure 4b). The first signal was a sine wave sent at a driving frequency of 155 kHz. The second signal was a sweep transmitted by varying the frequency from 185 kHz to 195 kHz. The third signal was built as the average of the first two in order to have modulation. The driving frequencies were chosen so that the nonlinear responses could match as much as possible the central band of the transducers. The structural responses of these excitations were then measured with a sampling frequency of 5 MHz. The NEMI algorithm was performed using a Matlab code as post-processing manipulation of the recorded signals.

Table 1. Sensor coordinates: the origin of the xOy cartesian reference frame is the bottom left corner of the scanning window.

Sensor	x coordinate (cm)	y coordinate (cm)
1	30	11
2	30	8.3
3	30	5.7
4	30	3
5	0	11
6	0	8.3
7	0	5.7
8	0	3
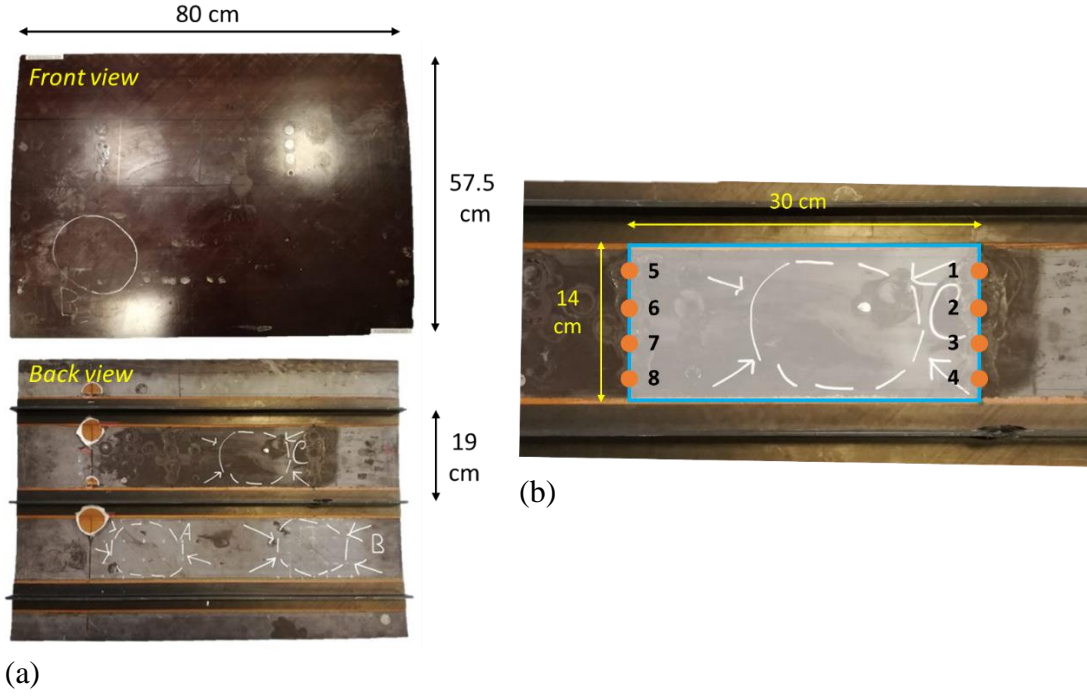
Figure 4. (a) Stiffened composite panel dimensions; (b) scanning window dimensions and sensor positions.

4. Experimental Results

4.1   Second harmonic as nonlinear input of NEMI method

NEMI method was performed on a region of a stiffened composite specimen (section 3). The second harmonic window of the 185 kHz – 195 kHz sweep was used to extrapolate the nonlinear inputs of the technique. According to section 2.2, the second harmonic frequency band (between 370 kHz and 390 kHz) was split in $k = 10$ small windows having a width of 2 kHz ($\Delta\omega$ in eq. 10) so that $n_D = 160$ points D were located in the scanned region (the paths between sensors on the same side were excluded, see figure 4b). After the statistical cut-out, 19 points D were left, and the image of the damaged region was created by assigning the corresponding nonlinear values. A 50% threshold was used to evaluate the damaged areas (estimated, S_{calc}, and real, S_{dam}) so that the results could be compared to a classical C-scan (figures 5a and 5e, respectively) and the accuracy of the technique could be quantified through two error functions:

$$\xi_{LOC} = \sqrt{(x_{calc} - x_{dam})^2 + (y_{calc} - y_{dam})^2} \tag{16a}$$

$$\xi_{AREA} = \left(1 - \frac{S_{calc} \cap S_{dam}}{S_{dam}}\right) \times 100\% \tag{16b}$$

The function in eq. (16a), ξ_{LOC}, is the distance between the centre of the real damaged area, (x_{dam}, y_{dam}), and the centre of the estimated damaged area, (x_{calc}, y_{calc}), and represents the error in calculating damage location. The function in eq. (16b), ξ_{AREA}, is the percentage of calculated area that does not overlap the real damaged area, used to evaluate the error in calculating damage area imaging and it will be referred as "area imaging error". In the second harmonic case, the maximum localisation error, ξ_{LOC}, was 6.3 mm whilst the maximum area imaging error, ξ_{AREA}, was 21%. This was due to the second harmonic contributions introduced by instrumentation and, in particular, by both McWade and Falco Systems amplifiers.

4.2   *Modulated responses as nonlinear input of NEMI method*

In order to avoid errors due to instrumentation faults, modulation bands were considered as nonlinear inputs of the method. Since the double frequency signal was composed of a continuous signal at 155 kHz and a sweep between 185 kHz and 195 kHz, the low modulation band resulted to be between 30 kHz and 40 kHz whilst the high modulation band was between 340 kHz and 350 kHz. Both single frequency continuous (155 kHz) and sweep (185 kHz to 195 kHz) responses were subtracted from the multiple frequency signals to eliminate any single frequency nonlinearity. Then, each modulation band was split in k = 10 small windows having a width of 1 kHz and NEMI technique was performed. In the first experiments, the nonlinear input was extrapolated from the low modulation band (figure 5b) whilst the second tests involved the high modulation band (figure 5c). Finally, an average of the two modulation contributions was calculated and then used as input of the method (figure 5d). Table 2 shows localisation and area errors for all cases. The results showed how the introduction of modulated responses led to a general improvement of damage imaging. When high modulation band was used as nonlinear input of NEMI method, although damage localisation error (3.2 mm) resulted decreased in comparison with the second harmonic case (6.3 mm), the error in damage area imaging was higher (29% instead of 21%). This was due to the very low amplitude of the high modulated response since the frequencies involved are far from the central frequency of the transducers. However, when low modulation band was involved, the result was much closer to the real case as damage localisation and imaging errors reduced to 1.8 mm and 6%, respectively. The low amplitude of the high modulated response also affected

the imaging from the averaged nonlinear modulated contributions ($\xi_{LOC} = 1.3$ mm and $\xi_{AREA} = 13\%$).

Table 2. NEMI localisation and area errors using different nonlinear parameters.

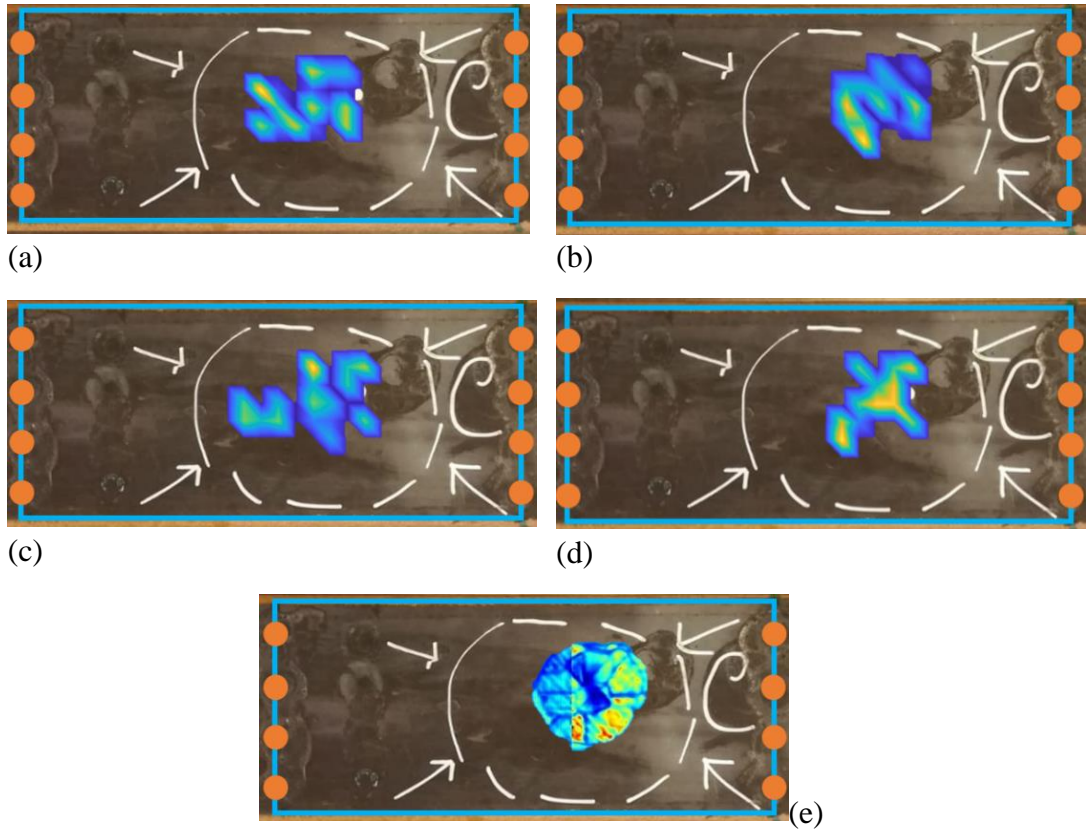| Nonlinear Parameter	Localisation error ξ_{LOC} (mm)	Area error ξ_{AREA} (%)
Second harmonic	6.3	21
Low modulation band	1.8	6
High modulation band	3.2	29
Average of modulation bands	1.3	13

(a)

(b)

(c)

(d)

(e)

Figure 5. Damage imaging through NEMI method by using different nonlinear contributions: (a) second harmonic, (b) low, (c) high and (d) average modulation bands. The results are compared to a (e) classic C-scan. A linear interpolation was used as a smoothing algorithm to create a clearer image.

5. Conclusions

This paper introduced a novel nonlinear damage imaging technique for aerospace composite structures, here named nonlinear elastic multi-path imaging (NEMI). This technique can be considered as a development of the nonlinear elastic multi-path reciprocal (NEMR) method and, thus, damage imaging is allowed on composite structures by sending and receiving ultrasonic signals from several surface bonded sensors. Nonlinear parameters, obtained from either second harmonic or modulation bands, are used as input of a reciprocal relationship applied on every path between coupled sensors in order to find the points closest to damage (points *D*, see section 2.2). Once the worst cases are discarded through a statistical approach, the nonlinear parameters are averaged on each path and their values are assigned to the corresponding point *D* so that an image of the damaged component can be built. The second order harmonic is often preferred as nonlinear source for SHM methods since the involved amplitudes are usually the highest. However, modulated responses are also considered for the NEMI technique as, unlike the second order harmonics, they are not affected by instrumentation noise and, thus, they can be considered as a more reliable nonlinear source. The proposed method was experimentally validated on a curved composite structure reinforced by three stiffeners and having barely visible damage in three different locations (see section 3). During the first part of the experimental validation, the energy distributed to the second harmonic frequency band was used as nonlinear input of the technique. Comparing the results to a classical C-scan, the calculated damaged area resulted slightly shifted leading to a maximum damage localisation error of 6.3 mm. The error was caused by the second harmonic contributions introduced by instrumentation. The second part of the experimental campaign involved the use of modulation bands as nonlinear input of the method. Low and high modulation bands, and their average, were used, respectively, to carry out three different sets of experiments. The introduction of modulated responses led to an improvement of damage imaging since the error was reduced to the 1.3 mm by using the low band of the nonlinear modulated contribution. The accuracy of NEMI technique can be considered more than satisfactory albeit it does not require a priori knowledge of structural properties such as thickness and group velocities of the propagating waveforms. The proposed method leads to better imaging of damaged

regions in complex aeronautical structures, resulting in improved reliability and accuracy of aircraft inspection procedures.

References

[1]   L. Yu, V. Giurgiutiu, In situ 2-D piezoelectric wafer active sensors arrays for guided wave damage detection, Ultrasonics 48 (2) (2008) 117–134.

[2]   S.S. Kessler, S.M. Spearing, C. Soutis, Damage detection in composite materials using Lamb wave methods, Smart Mater. Struct. 11 (2) (2002) 269.

[3]   M. Tabtabaeipour, J. Hettler, S. Delrue, K. Van Den Abeele, Reconstruction Algorithm for Probabilistic Inspection of Damage (RAPID) in Composites, in: 11th European Conference on Non-Destructive Testing (ECNDT 2014), 2014.

[4]   E.B. Flynn, M.D. Todd, P.D. Wilcox, B.W. Drinkwater, A.J. Croxford, Maximum likelihood estimation of damage location in guided-wave structural health monitoring, in: Proceedings of the Royal Society of London A: Mathematical, Physical and Engineering Sciences, 2011. The Royal Society.

[5]   F. Ciampa, E. Barbieri, M. Meo, Modelling of multiscale nonlinear interaction of elastic waves with three-dimensional cracks, J. Acoust. Soc. Am. 135 (6) (2014) 3209–3220.

[6]   F. Ciampa, S. Pickering, G. Scarselli, M. Meo, Nonlinear damage detection in composite structures using bispectral analysis, in: SPIE Smart Structures and Materials+Nondestructive Evaluation and Health Monitoring, International Society for Optics and Photonics, 2014.

[7]   K.-Y. Jhang, Nonlinear ultrasonic techniques for non-destructive assessment of micro damage in material: a review, International journal of precision engeneering and manufacturing 10 (1) (2009): 123-135.

[8]   S. Boccardi, D.-B. Calla, G.-P.M. Fierro, F. Ciampa, M. Meo, Nonlinear damage detection and localization using a time domain approach, in: SPIE Smart Structures and Materials+Nondestructive Evaluation and Health Monitoring. International Society for Optics and Photonics, 2016.

[9]   F. Ciampa, G. Scarselli, M. Meo, Nonlinear imaging method using second order phase symmetry analysis and inverse filtering, J. Nondestr. Eval. 34 (2) (2015) 1–6.

[10]   G.M. Fierro, F. Ciampa, D. Ginzburg, E. Onder, M. Meo, Nonlinear ultrasound modelling and validation of fatigue damage, J. Sound Vib. 343 (2015) 121–130.

[11]   G.P.M. Fierro, M. Meo, Nonlinear imaging (NIM) of flaws in a complex composite stiffened panel using a constructive nonlinear array (CNA) technique, Ultrasonics 74 (2017) 30–47.

[12]   F. Ciampa, G. Scarselli, S. Pickering, M. Meo, Nonlinear elastic wave tomography for the imaging of corrosion damage, Ultrasonics 62 (2015) 147–155.

[13]   F. Ciampa, S.G. Pickering, G. Scarselli, M. Meo, Nonlinear imaging of damage in composite structures using sparse ultrasonic sensor arrays, Struct. Control Health Monit. (2016).

[14]   G.P. Malfense Fierro, D. Dionysopoulos, M. Meo, F. Ciampa, Damage detection in composites using nonlinear ultrasonically modulated thermography. Nondestructive

Characterization and Monitoring of Advanced Materials, Aerospace, Civil Infrastructure, and Transportation XII 2018 Mar (Vol. 10599).

[15]   S. Boccardi, D.B. Callá, F. Ciampa, M. Meo, Nonlinear elastic multi-path reciprocal method for damage localisation in composite materials. Ultrasonics. 2018 Jan 1;82:239-45.

[16]   D. Donskoy, A. Sutin, A. Ekimov. Nonlinear acoustic interaction on contact interfaces and its use for nondestructive testing. Ndt & E International. 2001 Jun 1;34(4):231-8.

[17]   I. Solodov, J. Bai, S. Bekgulyan, G. Busse, A local defect resonance to enhance acoustic wave-defect interaction in ultrasonic nondestructive evaluation, Applied Physics Letters 99, pp. 211911 (2011).

Chapter 6

Thermo-electric power harvesting in aerospace applications

6.1 Motivation: powering a wireless structural health monitoring system

Nowadays, modern aircrafts comprise a big number of SHM systems which allow monitoring of the structural conditions of several critical regions, such as wings, engine bays and fuselage. Real time communication of SHM systems has, thus, become an important feature so that, if any problem occurs, the pilot is aware of what is happening. The technologies developed in the last two decades have allowed new ways of communication, such as wireless transmission which is slowly replacing communication by wires in order to decrease aircraft weight. Wireless technology, differently from communication by wires, needs a power source in order to function. Providing power by cable makes useless the wireless technology since data can be transmitted in the same way. Hence, the second part of the project, developed in parallel with the SHM part, was focused on the development of a power harvesting technique able to harvest ambient energy and use it as a local power source for aerospace wireless SHM applications. After an accurate study of the existing options, thermo-electric energy harvesting resulted to be the most suitable for aerospace application as heat waste from the engine is a reliable power source.

6.2 Summary: natural convection air cooling for thermo-electric generator

This part of the research was focused on the improvement of thermo-electric power harvesting for wireless SHM applications. An analytical characterisation of thermo-electric generator (TEG) power output behaviour was performed in order to set up the experiments and post process power generation results. Since TEG power output is proportional to the temperature difference between its top and bottom faces [46], the idea was placing the TEG on a heat source and decreasing the temperature of TEG cold face through an air cooling heatsink. Heat transfer was enhanced by improving both conductive and convective properties of the heatsink. Conduction could be increased by choosing the right material and, after a meticulous trade-off study, copper was chosen as a heatsink material, due to its ductility and high thermal conductivity. Convection is strictly related to the external surface of the heatsink and, hence, an optimisation process was performed to find the best heatsink geometry, taking into account environmental restrictions. The most common heatsink configuration consists of a flat base with surface-mounted pins, so that the study could be focused on pin geometry. A classic cylindrical pin heatsink (Figure 6.1a) was set as a reference and, considering manufacturing limitations, a novel heatsink was created by keeping same weight and height (Figure 6.1b).
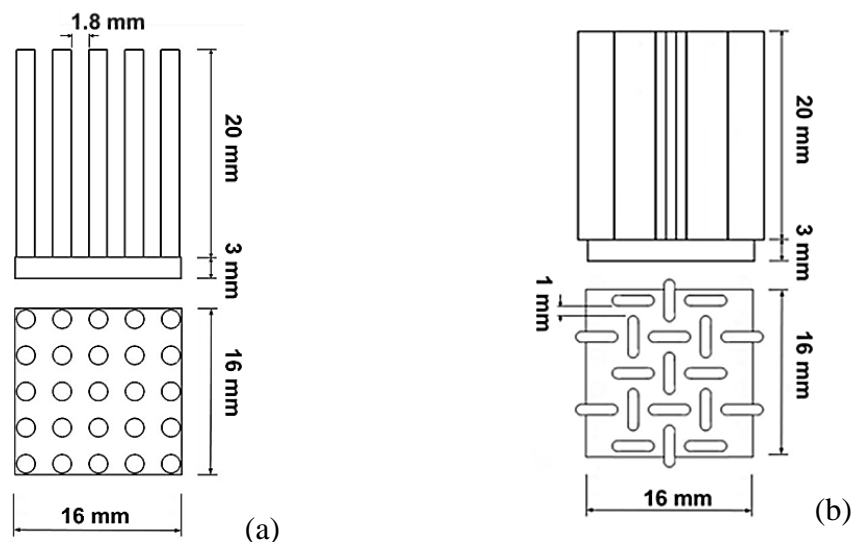

Figure 6.1. Heatsink geometries with (a) classic cylindric pin and (b) novel pin arrangements.

The effects of the novel heatsink geometry on TEG power output were examined through a number of 3D CFD simulations so that fluid-structure interactions could be

numerically analysed. The TEG-heatsink assembly was set in a natural convection environment, considering an input temperature of 100°C on TEG lower face and 25°C as ambient temperature. Then, the heatsinks involved in the numerical study were manufactured and simulation results were experimentally validated using the same boundary conditions. Further, an experimental campaign was conducted to evaluate the effects of different input temperatures on the power generation via novel TEG-heatsink assembly. The final part of the study was focused on the creation of a heatsink assembly able to feed a low-power electronic system, such as a wireless structural health monitoring (SHM) device. Two new heatsinks were combined through a copper sheet and then placed on TEG top side. The cooling performance of the assembly was improved by adding, to the copper sheet, a layer of super-conductive material, Pyrolytic graphite sheets (PGS), which allow a faster heat transfer. The assembly was tested to estimate experimental TEG temperatures and power outputs were measured.

6.3 Results: a novel heatsink design for an improved thermo-electric power output

Considering a pin-fin heatsink, two basic pin cross-sections, circular and rectangular, were chosen and analysed in order to maximise external surface. The optimal characteristic dimensions (the radius of the circular pin section and the length of the rectangular pin section, see Figure 6.2) were calculated keeping constant height (20 mm) and volume (62.8 mm^3) and resulted to be 1 mm and 3.2 mm for circular and rectangular pin sections, respectively. The rectangular pin showed a higher external surface and, thus, it was chosen as a pin shape for the novel heatsink. However, its characteristic dimension had to be increased to $L = 4$ mm due to manufacturing limitations. Therefore, a further study was necessary to address the resulting increase of volume and, accordingly, the number of pins was decreased from 25 (chosen baseline number) to 19.

Figure 6.2. Considered pin shapes. The circular section is commonly used whilst a rectangular section is proposed to enhance pin external surface.

Once the shape and the number of pins was chosen, thermal CFD simulations were performed in order to optimise pin arrangement by comparing the cooling effect of the proposed pin dispositions to a classic cylindrical pin heatsink. The mixed rectangular pin disposition resulted to be more effective than the aligned rectangular pin heatsink as TEG temperature difference was 22.7°C against 22°C. TEG temperature difference due to the cylindrical pin heatsink resulted to be the lowest (ΔT = 18.7°C). Such an increase of thermal difference is due to the enhanced thermal exchange surface of new pin geometry and the reduced size of the hot air region by means of the new pin arrangement. Numerical temperature differences were used to analytically obtain power outputs at different load resistances. The maximum TEG power outputs were 7.9 mW, 10.9 mW and 11.6 mW by using cylindrical pin heatsink, aligned and mixed rectangular pin heatsink. Thus, the idea of aligned rectangular pin was discarded and the cylindrical pin heatsink was kept as a baseline for comparison.

Hence, the two different heatsink geometries were manufactured, and simulation results were validated through a number of experiments. Considering same boundary conditions as the numerical model, experimental tests showed that the introduction of the novel heatsink improved TEG natural convection cooling, since it led to a measured temperature difference of ΔT of 20°C, nearly 2.3°C higher than cylindrical pin heatsink configuration. This corresponded to a measured maximum power output of 7.3 mW and 8.9 mW using classic and novel heatsink, respectively. Experimental temperature differences were slightly lower than the numerical results as, in order to save time, temperature losses caused by manufacturing defects and material impurities were not considered in the numerical CFD model.

Several experiments were carried out in order to estimate the effect of different input temperature on TEG temperature difference and, accordingly, TEG power output. The hot plate temperature was increased in steps of 25°C between 50°C and 150°C and both the classic and novel heatsinks were tested.

Table 6.1. TEG temperature differences and power output at different input temperatures.

TEG hot temperature T_{hot} (°C)	Temperature difference ΔT (°C)		Maximum power output P_{max} (mW)	
	Classic heatsink	Novel heatsink	Classic heatsink	Novel heatsink
50	4.3	4.8	0.6	0.8
75	11.5	13.3	3.1	4.2
100	17.7	20.1	7.3	8.9
125	24	26.2	12	14.1
150	31.7	34	20.2	23.8

Thermal results (see Table 6.1) confirmed the higher cooling effect of the novel heatsink applied on the TEG cold face.

In order to power a wireless SHM system [32], two novel heatsinks were combined through a copper sheet and PGS were introduced to improve heat transfer. The proposed assembly (Figure 6.3) was tested at the same boundary conditions as previous experiments in three configurations:

- No PGS
- PGS between copper sheet and heatsinks
- PGS between TEG and copper sheet
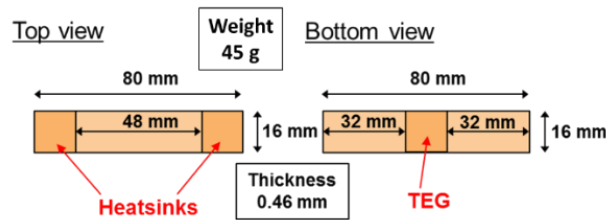
Figure 6.3. TEG-heatsink assembly geometry. Two novel heatsink are placed on a copper sheet which, in turn, is placed on the TEG.

TEG temperature difference achieved with two heatsinks placed on a copper sheet was 29.3°C and the maximum power output of the device was 20.1 mW. The PGS layer applied on the copper sheet below the heatsinks led to an increase of TEG temperature difference to 29.8°C and, thus, the maximum power output increased to 20.5 mW. The PGS applied between copper sheet and TEG increased, once again, both TEG temperature difference and maximum power output to a maximum of 30.4°C and 21.4 mW, respectively.

6.4 Paper: Design and development of a heatsink for thermo-electric power harvesting in aerospace applications

The proposed heatsinks and heatsink assemblies and details of data collection, experiments and results are going to be published soon as the manuscript was accepted by the journal Smart Materials and Structures [68]. The Statement of Authorship Form and the paper are shown in next pages.

This declaration concerns the article entitled:							
Design and development of a heatsink for thermo-electric power harvesting in aerospace applications							

Publication status (tick one)							
draft manuscript		**Submitted**		**In review**		**Accepted**	X	**Published**	
Publication details (reference)	Boccardi, S., Ciampa, F. and Meo, M., 2018. Design and development of a heatsink for thermo-electric power harvesting in aerospace applications. Smart Materials and Structures.							
Candidate's contribution to the paper (detailed, and also given as a percentage).	The candidate contributed to/ considerably contributed to/predominantly executed the… Formulation of ideas: 90% I proposed material and new geometries of heatsinks and heatsink assemblies. My supervisor proposed the idea of thermoelectric power harvesting for structural health monitoring. Design of methodology: 100% I decided the model-experiment approach, designed the experimental setup and created a script able to post-process experimental data. Experimental work: 100% I carried out all the experiments, collected all data, post-processed and evaluated experimental results. Presentation of data in journal format: 95% I decided the structure, collated data, wrote all drafts, prepared all figures and responded to reviews. My supervisor provided feedback on drafts and helped with publication process.							
Statement from Candidate	This paper reports on original research I conducted during the period of my Higher Degree by Research candidature.							
Signed	*Boccardi Salvatore*				**Date**	04/06/2019		

Design and development of a heatsink for thermo-electric power harvesting in aerospace applications

Salvatore Boccardi, Francesco Ciampa, Michele Meo

Department of Mechanical Engineering, University of Bath, Bath BA2 7AY, UK

Abstract

In recent years, the growing interest of aerospace companies in wireless structural health monitoring systems has led to the research of new energy efficient sources and power harvesting solutions. Among available environmental power sources, temperature gradients originated at different locations of the aircraft can be used by thermo-electric generators (TEGs) to create electrical voltage. TEGs are lightweight, provide high-energy conversion and do not contain movable parts. Thermal diffusion systems, commonly known as heatsinks, can be combined with TEGs to enhance their performance by increasing heat dissipation from a high temperature surface to the ambient air.

This paper focused on the enhancement of TEG performance by developing an air-cooled heatsink for low-power wireless structural health monitoring applications. The design, manufacturing and testing of the proposed thermal diffusion system was investigated by evaluating the increase of the temperature gradient between the opposite surfaces of a commercial TEG element. The thermal performance of the heatsink was assessed with numerical finite element thermal simulations and validated with experimental tests. Experimental results revealed that the proposed thermal diffusion system provided higher temperature differences and, therefore, higher output power in comparison with traditional cylindrical pin-fin heatsinks. A hybrid heat diffusion system composed by copper heatsinks and highly oriented pyrolytic graphite layers was also here proposed in order to allow TEG reaching wireless SHM operative power requirements of tens of mW and, at the same time, adapt the assembly to the complexity of aerospace SHM arrangements. Experimental results revealed that the proposed heatsink-TEG arrangement was able to generate an output power over 25 mW.

1. Introduction

Aircraft system complexity has increased year by year leading to the necessity of automated prognostic and structural health monitoring (SHM) systems. In order to execute the monitoring of aircraft components, a number of sensing devices are needed at different locations of the aerospace vehicle where sensible data can be captured. The communication among sensors and a central computer (or other sensors) is then necessary to make information available for end-users. On operating aircraft, data is transferred by wires that, unfortunately, provide a large contribution to the overall weight and require expensive maintenance. Thus, in recent times, aircraft companies are interested to sensing networks able to transmit information wirelessly. Since wireless systems require electrical power-on-demand for a variety of sensing applications, micro-power generators can be considered as a valuable alternative to current sources of energy such as batteries and power supplies, as they can extract energy from the surrounding environment. However, whilst power harvesting systems have been widely developed and described in literature for large-scale applications such as wind turbines [1], there is still a lack of technology for small-scale devices such as SHM systems for aerospace [2], [3]. Aircraft structures generally waste a large quantity of energy, mainly originated from natural sources such vibrations and heat, which could be harvested and reused. As an example, electrical current can be obtained from temperature gradients available at different locations of the aircraft (e.g. surrounding the engine), which can be used by thermo-electric generators (TEGs). The harvesting of mechanical vibration energy has also been considered by a number of authors [4], [5], but thermo-electric applications, when available, have showed a higher power output [6] in the range of tens of mW and good reliability [7]. TEGs are suitable for aerospace energy harvesting since they are lightweight, do not contain movable parts and provide high-energy conversion. Thermal diffusion systems (also known as heatsinks) can be used to enhance TEGs performance by increasing heat dissipation from a high temperature surface to the ambient air. The improvement of heatsink cooling performance has been a central problem in the past few years [8], [9] and [10]. The development of integrated circuits, such as central processing units (CPU) for home appliances (e.g. personal computers and graphic processor units), has

led to an increase of heat generation so that high-performance heatsinks are needed [11]. Only recently, however, these studies have been applied to thermo-electric energy harvesting [12], [13], and the use of TEGs for powering a wireless SHM system can be still considered an early stage concept [14]. In order to simplify design and optimisation of a TEG-heatsink assembly, computational fluid dynamics (CFD) can be a powerful tool that is able of comparing several heat exchangers under the same boundary conditions [15]. So far, a number of CFD models have been proposed in order to consider the fluid-structure interaction between the examined device and the surrounding environment [16]. Most of these numerical simulations were focused on applications where forced convection is the main heat exchange mechanism [17]. However, in many aerospace applications, such as inside aircraft pylons, the air can be assumed steady so that there is a natural convection regime. This paper is focused on TEG performance improvement through a heatsink in order to make it able to feed a low-power wireless SHM system for aerospace applications. Firstly, a novel heatsink is designed and its performance is compared with a classic pin-fin heatsink, through CFD analyses, by evaluating both temperature and power output of the TEG on which they are applied. Then, CFD results are validated through a number of experiments and, finally, two novel heat diffusion systems are combined in a new assembly composed by copper heatsinks and highly oriented pyrolytic graphite layers in order to allow the TEG to reach operative power requirements.

The paper is outlined as follows: in section 2 thermo-electric generators (TEG) are presented; in section 3 an optimisation process is performed in order to design a novel heatsink; in section 4 the proposed heatsink cooling performance is compared to a classic configuration through computational fluid dynamics (CFD) simulations; section 5 reports the experimental validation results; section 6 introduces a TEG-heatsink assembly for SHM and the main conclusions are discussed in section 7.

2. Thermo-electric energy harvesting

The thermo-electric phenomenon is described by two main effects: the Peltier effect and the Seebeck effect. The Peltier effect is the heat generation caused by an electric current flow in the junction of two different conductors [18]. The Seebeck effect, opposite to the Peltier effect, is the electric current generation from a thermal gradient source [19]. The potential difference V, due to Seebeck effect, can be expressed as:

$$V = \alpha \Delta T \tag{1a}$$

$$\alpha = \frac{\partial V}{\partial T} \tag{1b}$$

where ΔT is the temperature gradient and α is the Seebeck coefficient, i.e. the variation of potential difference V due to a variation of temperature T. Thermo-electric generators (TEG), also known as Peltier elements, are used to harvest energy through the Seebeck effect. A TEG is composed by a number of thermoelectric couples of n-type and p-type semiconductors [20] placed electrically in series and thermally in parallel (figure 1) so that the aggregation of electrons and holes on the cold side (in the n- and p-type legs, respectively) and their diffusion on the hot side create an electrical current able to feed a resistance load. Considering both Ohm's law and Kirchhoff law applied to a circuit having a TEG as the voltage generator, the load potential difference V_{load} and the electrical current i can be expressed as:

$$V_{load} = R_{load} i \tag{2}$$

$$i = \frac{V}{R_{load} + R_{int}} \tag{3}$$

where R_{int} is TEG internal resistance and R_{load} is the load resistance. Substituting eq. (3) into eq. (2) leads to:

$$V_{load} = \frac{R_{load}}{R_{load} + R_{int}} V \tag{4}$$

The TEG power output that feeds the load, P_{load}, can be defined as:

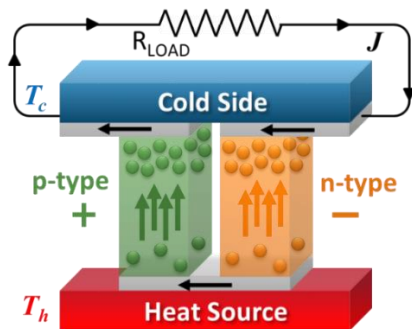$$P_{load} = \frac{V_{load}^2}{R_{load}} \tag{5}$$

Figure 1. Peltier element: the particles (holes and electrons) tend to accumulate on the cold side creating a potential difference.
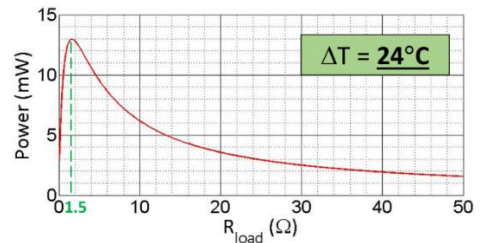
Figure 2. Typical curve representing TEG power output in function of the load resistance. TEG internal resistance R_{int} and Seebeck coefficient α are 1.5 Ohm and 0.012 V/K, respectively (see table 2).

and, thus, considering eqs. (4) and (1), it can be written as:

$$P_{load} = \frac{R_{load}}{(R_{load} + R_{int})^2} V^2 = \frac{R_{load}}{(R_{load} + R_{int})^2} (\alpha \Delta T)^2 \tag{6}$$

Once the TEG is chosen, the internal resistance R_{int}, the load resistance R_{load} and the Seebeck coefficient α are known properties so that the output power P_{load} only depends on the temperature difference ΔT, and can be calculated by using eq. (6). Figure 2 shows a curve representing TEG power output in function of load resistance at a fixed (constant) temperature difference ΔT of 24°C. The maximum power output is obtained when $R_{load} = R_{int}$ (i.e. 1.5 Ω as in the case of figure 2) so that:
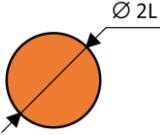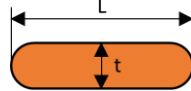
$$P_{max} = \frac{V^2}{4R_{int}} = \frac{(\alpha \Delta T)^2}{4R_{int}} \tag{7}$$

3. Natural convection air cooling heatsinks

3.1   Introduction

Since the internal resistance and Seebeck coefficient are material (constant) properties of the TEG element, with reference to eqs. (6) and (7), the TEG power output can be increased by enhancing the temperature difference between its top and bottom faces. Since the hot face temperature of the Peltier element depends on the available heat source, that is generally fixed and cannot be controlled, the temperature difference can be increased only by decreasing the temperature of TEG cold face. Many thermal cooling methods have been developed in the past years [12]. In an aerospace environment, volume and weight must be kept as small as possible and, thus, several cooling strategies, including the use of liquid cooling systems have to be discarded. Hence, a suitable option for aerospace applications is air cooling through a heatsink placed on the cold face of the TEG. Considering an adiabatic indoor environment such as inside an aircraft pylon, the air can be assumed steady, so that natural convection is the main mechanism of heat transfer [21]. Since the heat transfer is a combination of conduction and convection (radiation can be neglected), the heatsink performance can be improved by choosing the right material and appropriate geometry. In general, according to Newton's cooling law, the heat transfer can be enhanced by (a) increasing the temperature gradient between heatsink and ambient, (b) increasing the convection heat transfer coefficient and (c) increasing the surface area of the heatsink.

Table 1. Considered pin shapes, requirements and manufacturing limitations.

	Circular pin	Rectangular pin
Pin shape		
Reference pin volume V_{pin}	62.8 mm^3 (requirement)	
Reference heatsink volume V_{tot}	1571 mm^3 (requirement)	
Maximum pin height H_{max}	20 mm (requirement)	
Minimum cross-section dimensions t, L	1 mm (manufacturing limit)	

The latter is the most realistic and cost-effective option. Hence, the focus of the proposed research was the design of a new heatsink geometry capable of enhancing the TEG cooling performance [22].

3.2 Pin-fin heatsink optimisation

The most common heatsink configuration consists of a flat base with surface-mounted pins, so that the geometry of each pin can be modified to increase the heat transfer rate. In this work, a classic cylindrical pin heatsink (figure 4a) was here set as a reference and, taking into account manufacturing limitations, a novel heatsink was created by keeping same weight and height (figure 4b and table 1).
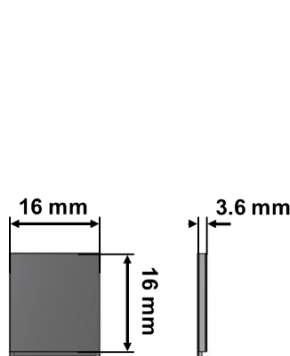
Figure 3. Illustration of TEG geometry.
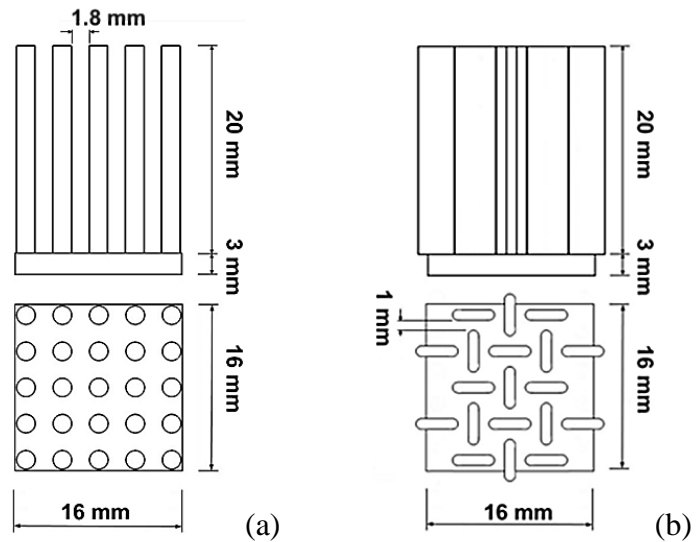
Figure 4. Heatsink geometries with (a) classic cylindric pin and (b) novel pin arrangements.

In the interest of keeping the manufacturing process as simple as possible, two basic pin cross-sections, circular and rectangular, were chosen and analysed in order to maximise the pin external surface (table 1). A mathematical formulation was carried

out for both pin shapes so that an ideal characteristic dimension L (the radius of the circular pin section and the length of the rectangular pin section) could be calculated. The expressions for the pin height H were deduced from the pin volume V_{pin} formulae:

$$\textit{Circular pin section} \qquad\qquad \textit{Rectangular pin section}$$

$$V_{pin} = \pi L^2 H \qquad\qquad\qquad V_{pin} = tHL \qquad\qquad (8a)$$

$$H = \frac{V_{pin}}{\pi L^2} \qquad\qquad\qquad H = \frac{V_{pin}}{tL} \qquad\qquad (8b)$$

where t is the minimum thickness of the rectangular shape. Since, in the case of pins, most of the total surface area is given by the lateral surface area, the expressions for the pin external surface S_{pin} can be simplified as:

$$S_{pin} = 2\pi LH \qquad\qquad\qquad S_{pin} = 2(L + t)H \qquad\qquad (9)$$

Substituting eqs. (8b) in eqs. (9):

$$S_{pin} = \frac{2V_{pin}}{L} \qquad\qquad\qquad S_{pin} = 2V_{pin}\left(\frac{1}{t} + \frac{1}{L}\right) \qquad\qquad (10)$$

The characteristic dimension was varied between 1 mm (manufacturing limit) and 10 mm and the results are showed in figure 5. According to the requirements and the manufacturing limits, the optimal characteristic dimensions were 1 mm and 3.2 mm for circular and rectangular pin sections, respectively.

(a)   (b)

Figure 5. Optimisation of the pin shape: (a) pin height and (b) pin external surface area in function of the characteristic dimension.

The rectangular pin showed a higher external surface and, thus, it was chosen as a pin shape for the novel heatsink. Even if the rectangular pi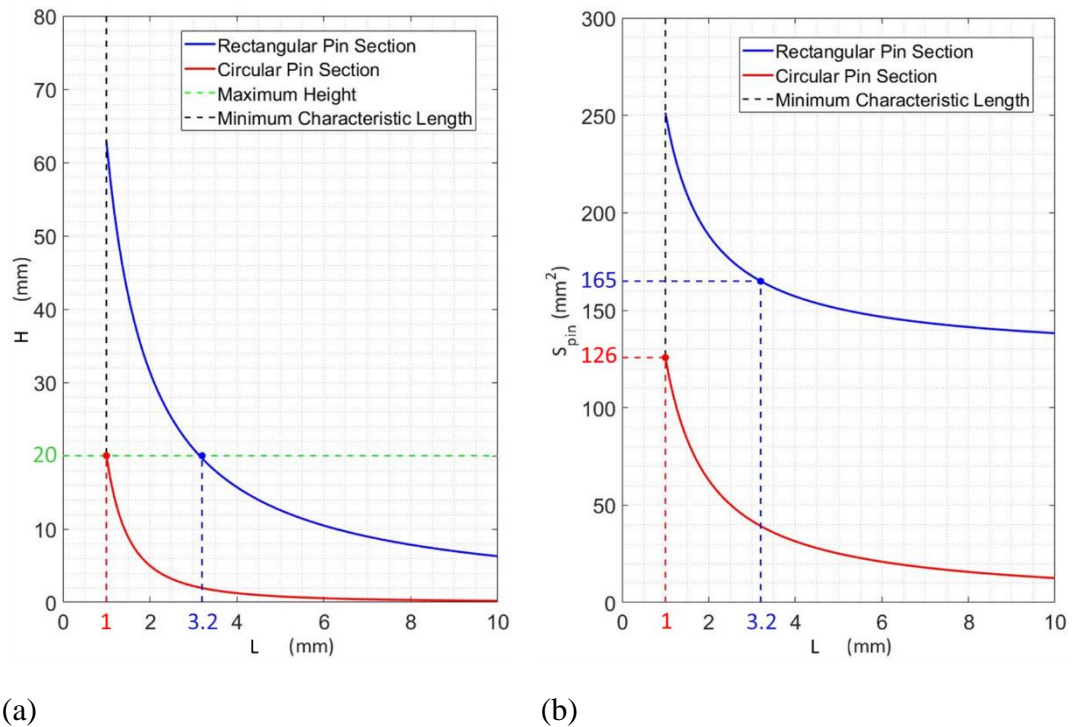n optimal length L was 3.2 mm, such a value can be considered as an ideal case that can be realised through additive manufacturing technology. In this investigation, computer numerical control (CNC) machining was the available manufacturing process so that the characteristic dimension had to be increased to $L = 4$ mm. At this point, a new study was necessary in order to find the number of novel pins N_{pin} that matches the total volume of the reference heatsink (figure 6). The expression of the total volume V_{tot} allows to calculate the characteristic dimension L in function of the number of pins N_{pin}:

Circular pin section   *Rectangular pin section*

$$V_{tot} = N_{pin}\pi L^2 H_{max} \qquad\qquad V_{tot} = N_{pin}t H_{max}L \qquad (11a)$$

$$L = \sqrt{\frac{V_{tot}}{N_{pin}\pi H_{max}}} \qquad\qquad L = \frac{V_{tot}}{N_{pin}t H_{max}} \qquad (11b)$$

where H_{max} is the maximum height from requirements (20 mm). The expressions for the heatsink external surface S_{ext} can be written as:

$$S_{ext} = 2N_{pin}\pi L H_{max} \qquad\qquad S_{ext} = 2N_{pin}(L + t)H_{max} \qquad (12)$$

Substituting eqs. (11b) in eqs. (12):

$$S_{ext} = 2\sqrt{N_{pin}\pi H_{max}V_{tot}} \qquad\qquad S_{ext} = \frac{2V_{tot}}{t} + 2N_{pin}H_{max}t \qquad (13)$$

Table 2. Material properties.

Thermoelectric Generator (TEG)		Heatsink (HS) – Copper		Pyrolytic Graphite Sheet (PGS)	
Density	5.4 g/cm^3	Density	8.92 g/cm^3	Density	2.1 g/cm^3
Weight	5 g	Weight	20 g	Weight	<0.1 g
Thermal conductivity	0.08 W/(mK)	Thermal conductivity	400 W/(mK)	Thermal conductivity	1950 W/(mK)
Internal resistance	1.5 Ohm	Specific heat	385 J/(kgK)	Thickness	25 μm
Seebeck coefficient	0.012 V/K				
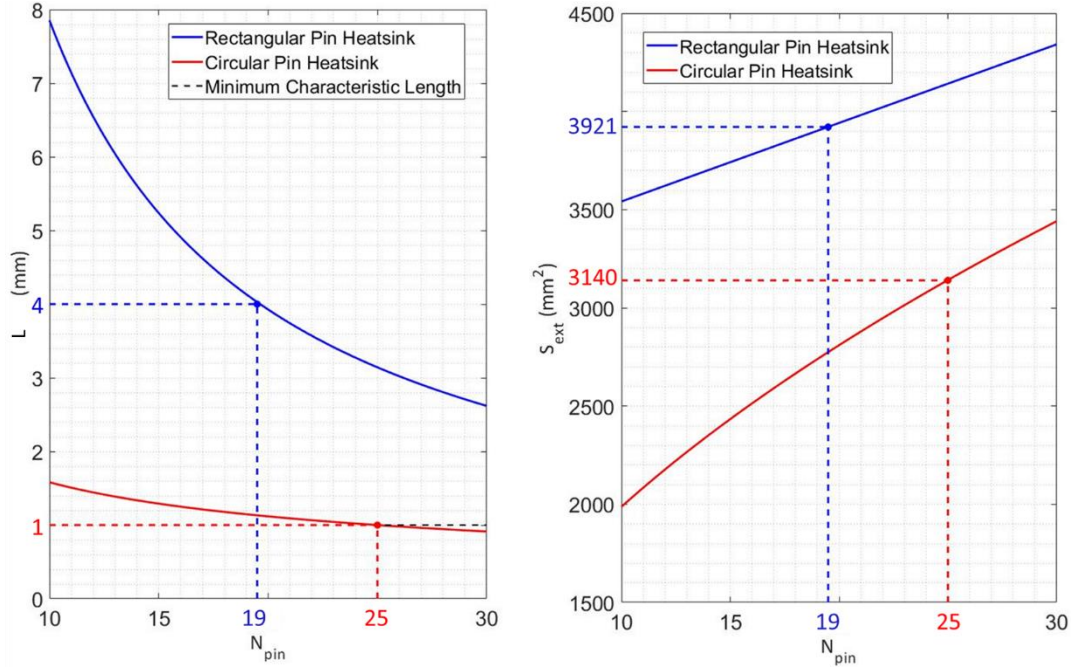
(a)   (b)

Figure 6. Optimisation of the pin number: (a) pin characteristic dimension and (b) pin external surface area in function of the pin number.

4. Thermal CFD analysis in a natural convection environment

4.1   Numerical CFD simulation set-up

ANSYS Fluent was used to perform a number of 3D CFD simulations so that fluid-structure interactions could be numerically analysed. The whole assembly was set inside a box with dimensions 300 mm x 300 mm x 300 mm in order to neglect boundary effects. According to section 3, natural convection was considered as solid-fluid thermal exchange mechanism and, since the TEG-heatsink assembly was set inside a closed domain, a steady-state calculation was possible by using the Boussinesq model [23]. In this model, density can be assumed as a constant in balance equations. The only exception is the density in the buoyancy term of the momentum equation, which can be approximated as follows:

$$(\rho - \rho_0)g \approx -\rho_0\beta(T - T_0) \tag{14}$$

where ρ_0 is the constant density of the flow, T_0 is the operating temperature, g is the gravity acceleration, and β is the thermal expansion coefficient. Eq. (14) is obtained by using the Boussinesq approximation:

$$\rho = \rho_0(1 - \beta\Delta T) \tag{15}$$

113

in order to eliminate ρ from the buoyancy term. This approximation is allowed in the present case since $\beta(\mathrm{T} - \mathrm{T}_0) \ll 1$. Thermal models were built with ANSYS Mechanical APDL software, whilst ANSYS Workbench allowed meshing the thermal system composed by the TEG and the heatsink (figure 8 and table 3). Once boundary conditions were applied, the thermal solution was calculated using ANSYS Fluent. A fixed temperature of 100° C was applied to the TEG hot side and the ambient temperature was set at 25°C (figure 7). A layer of insulant material was inserted between the TEG and the heatsink in order to take into account the air-filled regions due to the roughness at TEG-heatsink interface. MATLAB software was used to post-process temperature differences achieved in the numerical FE simulations in order to obtain TEG power outputs.

4.2   Pin disposition choice and heatsink comparison via CFD

Once the shape and the number of pins have been chosen, thermal CFD simulations were performed in order to compare two novel pin dispositions and choose the best pin arrangement in terms of cooling effect on the TEG. Moreover, the cooling effect of the examined heatsinks was compared to a classic cylindrical pin heatsink.

Table 3. Summary of finite element models.

		Classic heatsink		Aligned rectangular pin heatsink		Novel heatsink	
Body	TEG	Heatsink	Fluid	Heatsink	Fluid	Heatsink	Fluid
Element type	Linear hexahedron	Linear tetrahedron	Linear tetrahedron	Linear tetrahedron	Linear tetrahedron	Linear tetrahedron	Linear tetrahedron
Number of elements	1024	363966	1237218	124535	616502	178033	793424
Number of nodes	1445	79565	227644	31529	116547	44203	151325

In a natural convection environment, considering an input temperature of 100°C on TEG lower face and 25°C as ambient temperature, the aligned rectangular pin heatsink allowed a TEG temperature difference ΔT of 22°C whilst the rectangular pin mixed disposition increased such a value to 22.7°C. The TEG temperature difference due to the cylindrical pin heatsink resulted to be the lowest ($\Delta T = 18.7$°C). Such an increase

of thermal difference is due to the enhanced thermal exchange surface of new pin geometry (figures 8a, 8b and 8c) and the reduced size of the hot air region by means of the new pin arrangement (figures 8d, 8e and 8f). Thus, the heatsink with rectangular pin mixed disposition can be considered as the novel heatsink.
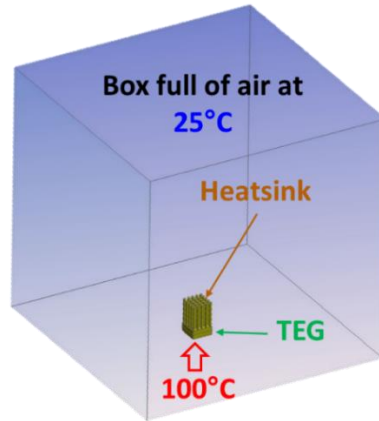
Figure 7. CFD simulation set-up.

The temperature drop between TEG and heatsink is caused by the presence of an insulant layer representing poor thermal coupling. Further, according to section 2, numerical temperature differences were used as input in eq. (6) to obtain power outputs at different load resistances.
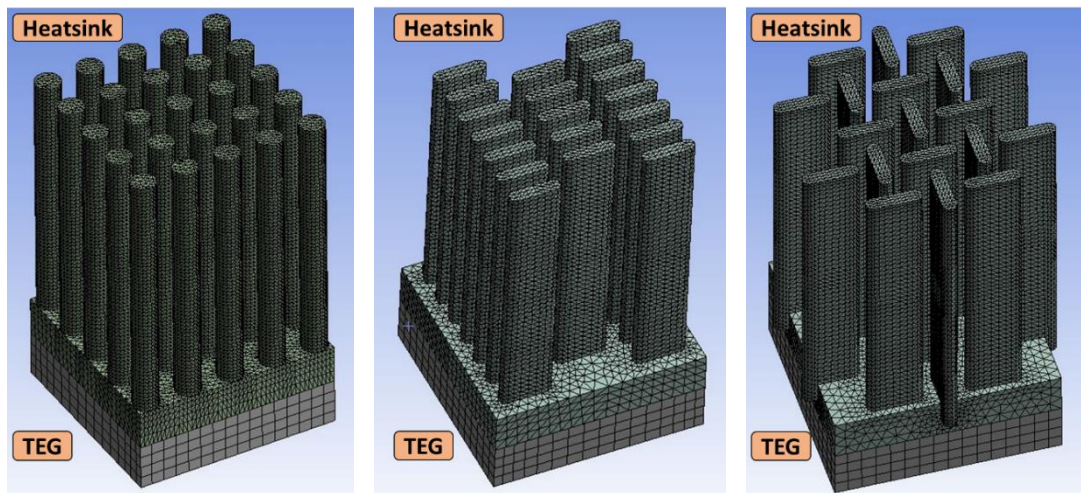
(a) (b) (c)

Figure 8. Meshed geometry of the TEG together with (a) classic, (b) aligned rectangular pin and (c) novel heatsinks.
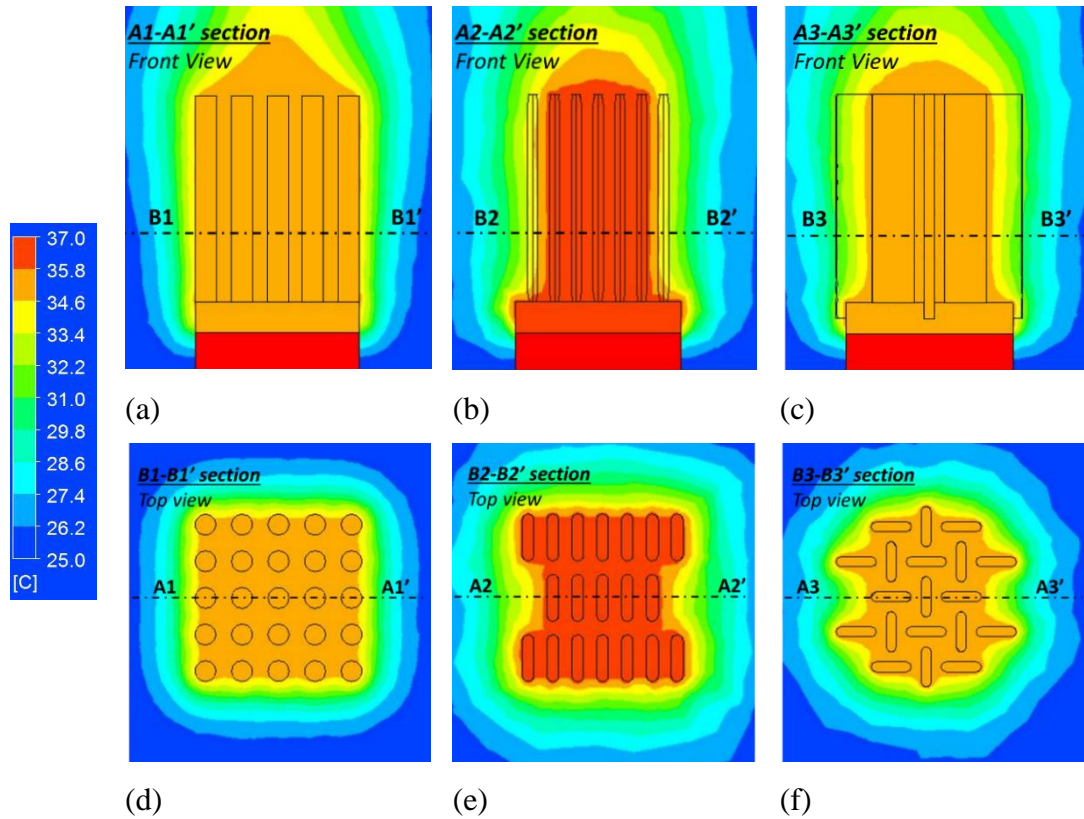
Figure 9. CFD simulation results: static temperature contour of classic (a)-(d), aligned rectangular pin (b)-(e) and novel (c)-(f) heatsink. Sections B-B' are placed at a height of 10 mm from the bottom of the TEG whilst sections A-A' placed right in the middle of the TEG-heatsink system.

The maximum TEG power outputs were 7.9 mW, 10.9 mW and 11.6 mW by using cylindrical pin heatsink, aligned rectangular pin heatsink and novel heatsink, respectively (figure 10).

Figure 10. Numerical TEG power output by using (a) classic, (b) aligned rectangular pin and (c) novel heatsinks. The temperature differences ΔT are calculated by averaging node temperatures on bottom (hot) and top (cold) areas of the TEG.

5. Experimental validation of CFD results

5.1   *Specifications and material properties*

The two different heatsink geometries, introduced in section 3, were manufactured by following the same procedure, i.e. fixing a number of pins on a flat base (table 2 and figures 3 and 4, respectively). Thus, simulation results were validated through a number of experiments. Looking at figure 11, the heat source was reproduced through a Heidolph MR Hei-Standard hot plate and load conditions were introduced by using a Cambridge Instrument ACDC decade resistor. The room temperature was set at 25°C and two thermocouples, placed on both the hot and the cold side of the TEG, allowed an experimental temperature difference evaluation. A PicoScope PC Oscilloscope was linked to a computer to capture the TEG output voltage and MATLAB was used to analyse the results. The output voltages (V) were captured at different load resistances (R_{load}) ranging between 0°C and 50°C, and the resulting power outputs were calculated through eq. (5). A Fischer Elektronic silicon-free thermally conductive paste (WLPK-10) was used to improve the thermal coupling between TEG and heatsink.
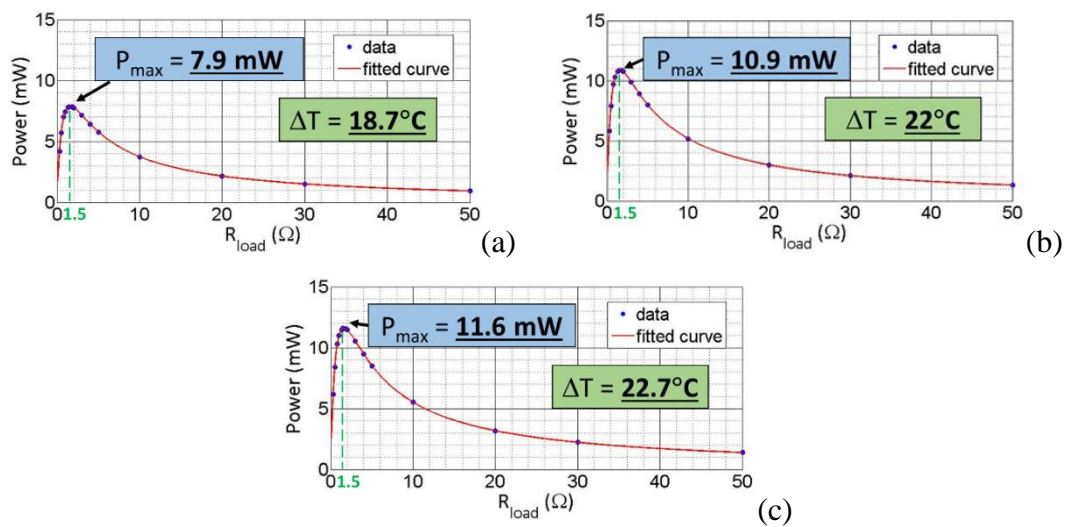
5.2   *Experimental TEG temperature difference and power output*

Several experiments were carried out to validate the numerical CFD results in section 4, which are shown in figures 9 and 10. As in the numerical model, the hot plate and room temperatures were set at 100°C and 25°C, respectively. Experimental tests showed that the introduction of the novel heatsink improved TEG natural convection cooling since it led to a measured temperature difference *ΔT* of 20°C, nearly 2.3°C higher than cylindrical pin heatsink configuration.
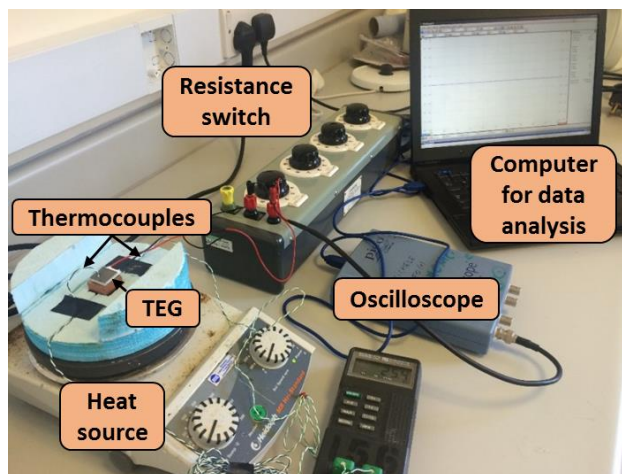
Figure 11. Experimental set-up.

The measured TEG power output data was fitted using eq. (6) (figure 12) so that maximum power output was 7.3 mW and 8.9 mW using classic and novel heatsink, respectively. It should be noted that experimental temperature differences resulted to be slightly lower than the numerical results. This could be due to temperature losses caused by manufacturing defects including stuck/stacked fin poor thermal contact and material impurities. These losses were not simulated in the numerical CFD model so that the optimisation process was less expensive in terms of time.

5.3 Experiments at different TEG hot side temperatures

A number of experiments was carried out in order to understand how the hot plate temperature affected the TEG temperature difference and, in turn, the TEG power output. The hot plate was set at a constant temperature between 50°C and 150°C (see table 4) and both the classic and novel heatsinks were bonded on a single TEG as in section 5.2.
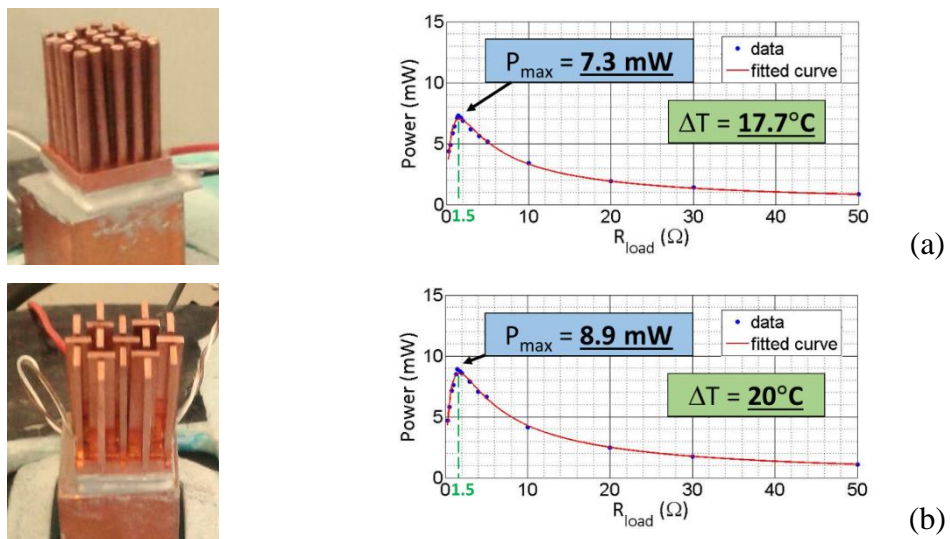
Figure 12. TEG power output comparison: (a) the classic cylindric pin shape heatsink and (b) the proposed novel pin shape heatsink.

Thermal results confirmed, once more, the higher cooling effect of the novel heatsink applied on the TEG cold face. With reference to figures 13 and 14, the increase of hot temperature led to a linear increase of temperature difference and a quadratic increase of maximum power output (in accordance with section 2).

118

Table 4. TEG temperature differences and power output at different input temperatures.

TEG hot temperature T_{hot} (°C)	Temperature difference ΔT (°C)		Maximum power output P_{max} (mW)	
	Classic heatsink	Novel heatsink	Classic heatsink	Novel heatsink
50	4.3	4.8	0.6	0.8
75	11.5	13.3	3.1	4.2
100	17.7	20.1	7.3	8.9
125	24	26.2	12	14.1
150	31.7	34	20.2	23.8

(a)   (b)

Figure 13. TEG power output curve behaviour at different hot temperatures: (a) classic heatsink case and (b) novel heatsink case. In both cases, the power output (red curves) increases with the input temperature (50°C, 75°C, 100°C, 125°C and 150°C, from bottom to top)."

(a)   (b)
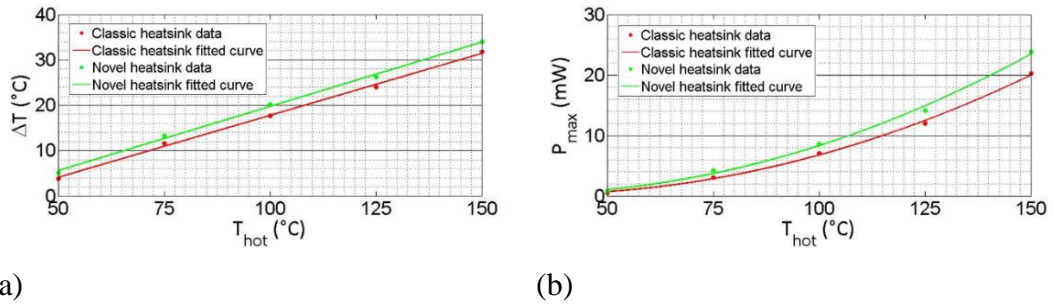
Figure 14. Heatsink effect comparison at different input temperatures: (a) TEG temperature difference and (b) TEG power output.

6. TEG-heatsink assembly for wireless SHM applications

6.1   Introduction

In order to power a wireless SHM system, there is the necessity to further increase TEG power output (typically in the range of few mW) up to two/three times more [24]. Thus, a system including more than one heatsink can be a valid solution to enhance TEG temperature difference. However, in most of aerospace applications, the space available for heatsinks can be limited, or even not sufficient, due to the complexity of some SHM arrangements.
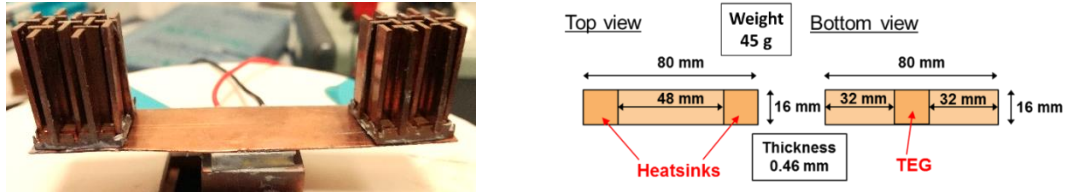
Figure 15. TEG-heatsink assembly geometry.

This issue can be overcome by transferring the heat from the TEG to a location where heatsinks can be placed. A high thermal conductivity material can be used to link TEG and heatsinks so that the heat can quickly spread and dissipate. Based on these considerations, the heatsink assembly proposed in this work consists of two novel heatsinks placed on a copper sheet (figure 15). By assuming that a quick heat transfer corresponds to a higher cooling performance, the heatsink system was improved by placing pyrolytic graphite sheets (PGS) on the copper plate. PGS have a very high in-plane thermal conductivity (1950 W/mK, see table 2) so that they can be used to enhance the heat spreading and, accordingly, the dissipation. By using the heatsink system composed by a combination of copper and PGS materials, the TEG power output could be sufficient to power a wireless SHM system.

6.2   Experimental results

The improvement of the TEG performance due to the novel heatsink led to the possibility of feeding a low-power electronic system, such as a wireless structural health monitoring (SHM) device. In order to reach the power requirements of tens of mW [24], a heatsink assembly was created by combining two new heatsinks through a copper sheet and then placed on the TEG top side (figure 15). Since heat diffuses from TEG to the heatsinks, the cooling performance of the assembly was improved by adding a layer of super-conductive material to the copper sheet in order to allow a faster heat transfer. Pyrolytic graphite sheets (PGS, table 2) were chosen to fulfil this task because of their very high in-plane thermal conductivity. According to previous sections, a number of experiments was carried out and both TEG temperatures and power outputs were measured. The TEG temperature difference achieved with two heatsinks placed on a copper sheet was 29.3°C and the maximum power output of the device was 20.1 mW (figure 16a). PGS application increased the heat transfer and, accordingly, the power output. The PGS layer was firstly applied on the top face of the copper sheet (below the heatsinks, figure 16b). TEG temperature difference increased

to 29.8°C and, thus, the maximum power output increased to 20.5 mW. Then, PGS was applied on the bottom face of the copper sheet (figure 16c) and, once again, both TEG temperature difference and maximum power output increased to 30.4°C and 21.4 mW, respectively.
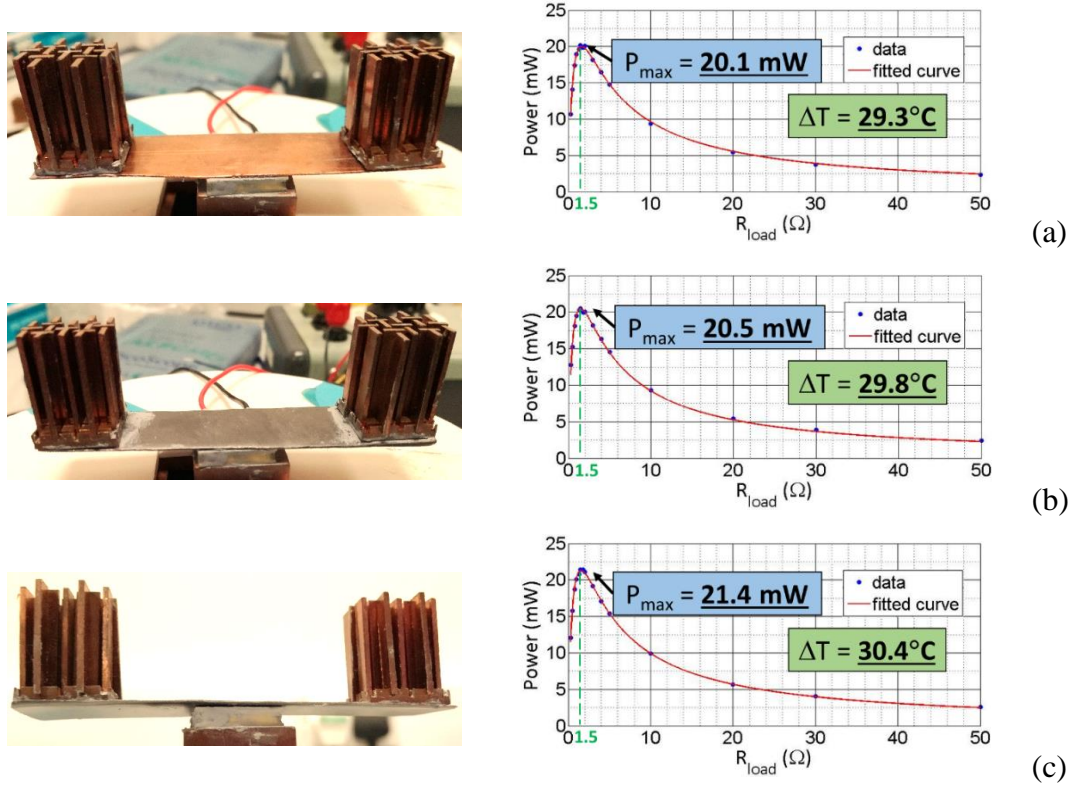
Figure 16. TEG-heatsink assembly experimental set-up and results (a) without PGS, (b) with PGS on top of the copper sheet and (c) with PGS on bottom of the copper sheet.

This configuration gave the best results because PGS high in-plane thermal conductivity was more effective when the graphite was directly in contact with the TEG. The generated energy can be regulated by a power management system in order to allow impedance matching between TEG (R_{int} = 1.5 Ω) and load [25]. The power output of the proposed device can be considered enough to feed a wireless SHM system suitable for aerospace structures (0.15 mW in inactive mode, 18 mW during transmission [24]). Although the two-heatsink arrangement allowed the harvesting of a good amount of power, it is much heavier than the system involving only one heatsink (45 grams instead of 20 grams). However, since a single aircraft data transmission cable has a weight of 32 g/m [26] and has a length of several meters, the proposed power harvesting system can be considered for aerospace applications.

7. Conclusions

This paper was focused on thermo-electric generator (TEG) performance improvement through a heatsink so that it can be suitable for a low-power wireless SHM system. Considering a classic commercial heatsink, having cylindrical pins, as a reference, an optimisation process was performed in order to find the optimum pin shape and pin number. During the process, both pin height and heatsink volume were kept constant and manufacturing limitation were taken into account. Aiming to an easy manufacturing, two basic pin cross-section shape, rectangular (new) and circular (classic), were analysed and the pin external surface was maximised leading to an increase of the heatsink convective thermal exchange. Fixing the pin height to 20 mm and the pin volume to 68.2 mm^3, the circular pin section with a radius of 1 mm (minimum dimension allowed from manufacturing) showed an external surface of 126 mm^2 whilst the rectangular pin section having a thickness of 1 mm and a length of 3.2 mm increased such a value to 165 mm^2. In the case of rectangular pin shape, a length of 3.2 mm has to be considered an ideal value that could be reached through additive manufacturing. CNC machining allowed a pin length of 4 mm so that a new study was carried out to calculate the number of pins necessary to match the reference heatsink volume. Although the reference heatsink was composed of 25 pins, leading to a total external surface of 3140 mm^2, the new pin heatsink showed an augmented exchange area of 3921 mm^2, needing only 19 pins. Two new pin arrangements, aligned and mixed, were studied through CFD thermal analyses in order to choose the best configuration in terms of the cooling effect on the TEG. TEG hot face temperature was 100°C whilst the surrounding environment was set at a temperature of 25°C with natural convection as heat transfer between air and heatsink. Numerical results showed that, using the rectangular pin mixed disposition heatsink, TEG temperature difference ΔT was 22.7°C, enhanced of 0.7°C respect to the aligned rectangular pin heatsink case and 4°C respect to the classic cylindrical heatsink. Thus, the rectangular pin mixed disposition heatsink was chosen as novel heatsink. Since TEG internal resistance and Seebeck coefficient were known, power output could be calculated for every load condition. The maximum power output, depending on temperature difference, resulted to be increased by the new heatsink (11.6 mW) in comparison with the aligned pin heatsink (10.9 mW) and the classic heatsink (7.9 mW). The two heatsinks (classic and novel) were actually manufactured so that CFD simulation results could be validated

through a number of experiments. The improvement due to the new heatsink was confirmed, since the temperature difference resulted to be raised from 17.7°C to 20°C. Accordingly, maximum power output was increased from 7.3 mW to 8.9 mW. However, both experimental temperature differences and power outputs resulted to be lower than numerical results because CFD simulations did not consider heat transfer loss due to manufacturing defects. A different manufacturing process, such as casting, can lead to a TEG cooling performance improvement that is supposed to be greater in the new heatsink set-up, where the ΔT drop resulted to be higher. Experimental campaign was extended as the hot plate temperature was varied between 50°C and 150°C, with a step of 25°C, in order to evaluate the effect of input temperature on TEG-heatsink assembly. The increase of hot temperature led to a linear increase of temperature difference and, as consequence, a quadratic increase of maximum power output. At every hot plate temperature, the new heatsink, compared to a classic heatsink with same weight, showed a higher cooling performance. In the last part of this work, two novel heatsinks were combined in a novel hybrid configuration so that the TEG could reach operative SHM power requirements of tens of mW. A number of experiments was carried out and results showed that placing two heatsinks on a bare copper sheet allowed to reach a TEG temperature difference of 29.3°C leading to a maximum power output of 20.1 mW. Hence, PGS were used to enhance heat transfer in the new heatsink configuration. A PGS was placed between copper sheet and heatsinks and TEG ΔT increased to 29.8°C so that the maximum power output was 20.5 mW. On the other hand, placing a PGS between copper sheet and TEG increased even more these two parameters that reached 30.4°C and 21.4 mW, respectively. The generated energy, regulated by a power management system, can be considered enough to feed a wireless SHM system for aerospace applications (0.15 mW in inactive mode, 18 mW during transmission) and, even if the system weight is increased to 45 grams, the proposed arrangement can still be considered much lighter than a single aircraft data transmission cable (32 g/m). Further, since the proposed TEG-heatsink assembly is very adaptable, it can also be tailored to other uses such as biomedical and military applications.

References

[1]   Khaligh, A., Onar, O.C., 2010. "Energy Harvesting". CRC Press, pp. 101-159.

[2]   Boccardi, S., Callá, D.B., Ciampa, F. Meo, M., 2018. Nonlinear elastic multi-path reciprocal method for damage localisation in composite materials, Ultrasonics 82, pp. 239-245.

[3]   De Simone, M. E., Ciampa, F., Boccardi, S., Meo, M., 2017. Impact source localisation in aerospace composite structures, Smart Materials and Structures 26(12), p. 125026.

[4]   Scarselli, G., Nicassio, F., Pinto, F., Ciampa, F., Iervolino, O., Meo, M., 2016. A novel bistable energy harvesting concept, Smart Materials and Structures 25, p. 055001.

[5]   Erturk, A., Inman, D.J., 2011. Broadband piezoelectric power generation on high-energy orbits of the bistable Duffing oscillator with electromechanical coupling, Journal of Sound and Vibration 330, pp. 2339-2353.

[6]   Roundy, S., Steingart, D., Frechette, L., Wright, P., Rabaey, J., 2004. "Power sources for wireless sensor networks," International Conference on Embedded Wireless Systems and Networks. Madrid, Spain, pp. 1-17.

[7]   Ding, L.C., Akbarzadeh, A., Date, A., 2016. Performance and reliability of commercially available thermoelectric cells for power generation, Applied Thermal Engineering 102, pp. 548-556.

[8]   Nakayama, W., 1986. Thermal management of electronic equipment: A review of technology and research topics, Applied Mechanic Reviews 39(12), pp. 1847-1868.

[9]   Ndao, S., Peles, Y., Jensen, M.K., 2014. Effects of pin fin shape and configuration on the single-phase heat transfer characteristics of jet impingement on micro pin fins, International Journal of Heat and Mass Transfer 70, pp. 856-863.

[10]   Bouknadel, A., Rah, I., El Omari, H., El Omari, H., 2014. "Comparative Study of Fin Geometries for Heat Sinks in Natural Convection," International Renewable and Sustainable Energy Conference. Ouarzazate, Morocco, eds IEEE, pp. 723-728.

[11]   Hirasawa, T., Kawabata, K., Oomi, M., 2005. Evolution of the Heatsink Technology, Furukawa Review 27, pp. 25-29.

[12]   Elghool, A., Basrawi, F., Ibrahim, T.K., Ibrahim, H., Idris, D.M.N.D., 2017. A review on heat sink for thermo-electric power generation: Classifications and parameters affecting performance, Energy Conversion and Management 134, pp. 260-277.

[13]   Wang, C.C., Hung, C.I., Chen, W.H., 2012. Design of heat sink for improving the performance of thermoelectric generator using two-stage optimization, Energy 39, pp. 236-245.

[14]   Pearson, M.R., Eaton, M.J., Pullin, R., Featherston, C.A., Holford, K.M., 2012. "Energy harvesting for aerospace structural health monitoring systems," Journal of Physics: Conference Series 382(1), pp. 20-25.

[15]   Bai, S., Lu, H., Wu, T., Yin, X., Shi, X., Chen, L., 2014. Numerical and experimental analysis for exhaust heat exchangers in automobile thermoelectric generators. Case Studies in Thermal Engineering 4, pp. 99-112.

[16]   Bhutta, M.M.A., Hayat, N., Bashir, M.H., Khan, A.R., Ahmad, K.N., Khan, S., 2012. CFD applications in various heat exchangers design: A review, Applied Thermal Engineering 32, pp. 1-12.

[17]   Junaidi, M.A.R., Rao, R., Sadaq, S.I., Ansari, M.M., 2014. Thermal Analysis of Splayed Pin Fin Heat Sink, International Journal of Modern Communication Technologies & Research 2, pp. 48-53.

[18]   Peltier, J.C.A., 1834. "Nouvelles expériences sur la caloricité des courants électriques". Annales de Chimie et de Physique, vol. 56, pp. 371-386.

[19]   Seebeck, T.J., 1826. "Ueber die magnetische Polarisation der Metalle und Erze durch Temperaturdifferenz". Annalen der Physik, vol. 82, pp. 253-286.

[20]   Neamen, D.A., 2012. "Semiconductor physics and devices: basic principles". McGraw-Hill Education, pp. 103-148.

[21]   Sanz Martinez, P.T., Cortes, D.F., 2014. Aircraft engine supporting pylon, US 8740138 B2.

[22]   Bahadur, R., Bar-Cohen, A., 2005. Thermal Design and Optimization of Natural Convection Polymer Pin Fin Heat Sinks, IEEE Transactions on Components and Packaging Technologies 28(2), pp. 228-246.

[23]   Boussinesq, J., 1903. "Théorie analytique de la chaleur: mise en harmonie avec la thermodynamique et avec la théorie mécanique de la lumière". Gauthier-Villars, vol. 2.

[24]   Zhou, D., Ha, D.S., Inman, D.J., 2010. Ultra low-power active wireless sensor for structural health monitoring, Smart Structures and Systems 6(5-6), pp. 675-687.

[25]   Norton, D. E., Podell, A. F., 1975. Transistor amplifier with impedance matching transformer, US 3891934.

[26]   Daumand, T., Nexans, 2014. Data transmission cable intended for the aeronautical industry. U.S. Patent 20,140,299,348.

Chapter 7

Discussion and conclusions

7.1 Discussion

This project aimed to develop a self-powered wireless structural health monitoring (SHM) system for aerospace applications. Considering that wireless technology has evolved to a level that makes it suitable for the aforementioned applications, the focus of the work was on the development of new accurate SHM techniques as well as on improving power harvesting in order to make the system self-powered. Hence, the work was split in two main parts, progressed in parallel:

1. Introduction of novel nonlinear structural health monitoring methods;
2. Improvement of thermo-electric power harvesting.

The first proposed SHM method was an ultrasonic nonlinear time domain for damage detection and localisation in composite structures without any a priori knowledge of structural lay-up and thickness. In this technique, six surface-attached acoustic emission piezoelectric receiving sensors were used to capture the responses of a damaged structure excited by ultrasonic waves. Considering that cracks and delamination generate nonlinear responses, the idea was to use the time of arrival of the second order nonlinear ultrasonic waves in order to locate damage. Hence, the second order harmonic responses were extracted from the received signals through the phase symmetry analysis and their times of arrival were estimated via an Akaike information criterion methodology. In turn, times of arrival were used as input for a system of nonlinear equations which was solved via a combination of Newton's

iterative method and unconstrained optimisation. The lack of accuracy in time of arrival estimation, due to low amplitude of the received signals, led to the development of a new SHM technique which works in frequency domain and allows damage localisation avoiding time of arrival evaluation. This novel technique, named nonlinear elastic multi-path reciprocal method, is able to detect and localise damage through the evaluation of nonlinear parameters extracted from ultrasonic signals. Ultrasonic waves are transmitted and received via a number of surface bonded sensors placed close to the edge of a damaged structure and, for each received signal, an analysis is performed to extract two second order nonlinear parameters, $\bar{\beta}$ and b^2. The bicoherence b^2, a higher order parameter, was introduced as an alternative to the classical second order parameter $\bar{\beta}$ in order to mitigate instrumentation noise. Sensors on opposite sides of the panel are coupled and, for each couple, nonlinear parameters are used as input for a reciprocal relationship which allows to calculate, on the path between the two opposite sensors, the point closest to damage. Damage is located by averaging all the calculated positions and discarding the worst cases. This technique was further developed to achieve damage imaging in composite structures, leading to a new SHM method, called nonlinear elastic multi-path imaging. As in the previous method, several surface bonded sensors are used to send and receive ultrasonic waves through a damaged composite structure. Ultrasonic sweeps are transmitted instead of single frequency waves so that enough information is available for damage imaging. Again, nonlinear parameters are extracted and used, on each path between two coupled sensors, as input of a reciprocal relationship that allows to find the point closest to damage. A statistical approach is used to discard the worst cases and, on each path, the average of nonlinear parameters is assigned to the calculated point allowing the creation of a 2D image of damage. In this SHM technique, modulated responses, unaffected by instrumentation noise, were introduced as an alternative to the second order harmonics.

The second part of the work was centred on the development of a thermo-electric power harvesting assembly, aiming to supply enough energy to feed a wireless SHM system. Thermo-electric power output, proportional to the temperature difference between the two opposite sides of a thermo-electric generator (TEG), was increased by decreasing TEG cold face temperature through an air cooling heatsink. A classic commercial heatsink, comprising cylindrical pins fixed in a flat base, was considered as a baseline case for an optimisation process aiming to find the optimum shape and

number of pins so that heatsink cooling performance can be maximised. Once found the optimised rectangular pin shape, it was arranged in two different ways so that two new heatsinks could be studied through CFD thermal analyses in order to choose the best configuration in terms of the cooling effect on the TEG. The heatsink with the chosen pin configuration was manufactured and its effect on TEG power generation was compared to a classic heatsink through several experiments so that CFD validation could be validated. Finally, a novel hybrid heatsink system was created by combining two novel heatsinks in order to allow the TEG to reach operative SHM power requirements of tens of mW.

7.2 Conclusion

The time-domain nonlinear technique was validated through a number of experiments carried out on a damaged quasi-isotropic CFRP composite panel with delamination. The results showed that damage localisation was achieved with satisfactory accuracy by transmitting ultrasonic waves at the driving frequency of 319.85 kHz. The maximum location error, throughout the experimental campaign, was ~5 mm. Hence, the novel method, different to previous damage localisation systems, allowed damage detection and localisation on composite panels without a priori knowledge of the group velocities of the propagating waveforms, as well as the structural lay-up and thickness. The nonlinear elastic multi-path reciprocal (NEMR) method was experimentally validated on an impacted anisotropic plate-like specimen which comprised various fibre orientations and, thus, different attenuation effects of the original wave with respect to the path angle. Experimental results demonstrated that damage localisation was not affected by the anisotropy of the structure. The non-dimensional second order harmonic parameter allowed an accurate damage localisation when the SNR was higher (SNR = 11.2 dB at a transmitting frequency of 218.5 kHz). Bicoherence parameter, instead, taking into account the quadratic phase coupling effect at the second harmonic, showed to be more sensitive to nonlinearities, allowing an accurate damage localisation when the SNR was lower (SNR = 1.8 at a frequency of 318.95 kHz). NEMR technique showed a maximum error between calculated and real impact locations of ~13 mm, considered more than satisfactory as an impact on composites produces a delamination all around the impact point. Although a distribution of

sending and receiving sensors, able to cover the delaminated area, is required by this method, damage localisation was achieved, again, with no a priori knowledge of structural lay-up and thickness and avoiding time of arrival estimation inaccuracies. The nonlinear elastic multi-path imaging (NEMI) method was tested on a curved composite panel reinforced by three stiffeners and having barely visible damage (BVID) in three different locations. NEMI method, as NEMR technique, was firstly validated by using the second harmonic frequency band as nonlinear input. The imaging results were compared to a classical C-scan and the maximum damage localisation error was 6.3 mm, due, once more, to second harmonic contributions introduced by instrumentation. Then, low and high modulation bands, and their average, were used, respectively, to carry out a second set of experiments. Damage imaging resulted to be improved by the introduction of modulated responses as the localisation error was reduced to 1.3 mm by using the low band of the nonlinear modulated contribution. This novel technique allows better imaging of damaged regions in complex aeronautical structures so that reliability and accuracy of aircraft inspection procedures can be improved.

The parallel research conducted on power generation improvement led to the introduction of a novel system composed by a thermo-electric harvester and an air cooling heatsink. The geometry of the heatsink was studied in order to enhance the heat transfer from the TEG to ambient air. Initially, pin shape was studied. Considering both circular and rectangular section pin shapes, pin height and pin volume were fixed to 20 mm and 68.2 mm^3, respectively, and the other dimensions were varied in order to maximise pin external surface area. The maximum pin area (165 mm^2) was achieved by the rectangular section (new) pin, having a thickness of 1 mm and a length of 3.2 mm. Manufacturing limits made this length to increase to 4 mm and, thus, a new study was carried out to calculate the number of pins necessary to match the baseline heatsink volume. The analysis results showed that the number of new pins had to be decreased from 25 (baseline heatsink) to 19. However, the total exchange area resulted to be increased from 3140 mm^2 (baseline heatsink) to 3921 mm^2. The effect of two different new pin arrangements on TEG cold face temperature was compared to a commercial heatsink through a number of thermal simulations so that the best pin disposition could be chosen. Numerical results showed that the rectangular pin mixed disposition heatsink allowed a TEG temperature difference of ΔT of 22.7°C, 0.7°C higher than the aligned rectangular pin heatsink case and 4°C higher than the classic

cylindrical heatsink case. Hence, the rectangular pin mixed disposition heatsink was chosen as novel heatsink. The corresponding theoretical power outputs were calculated, and the novel heatsink showed a maximum output of 11.6 mW. The improvement due to the novel heatsink was confirmed by experimental results. The maximum TEG temperature difference, obtained using the novel heatsink, was 20°C and the corresponding maximum power output was 8.9 mW. However, both experimental temperature differences and power outputs were lower than numerical results because heat transfer losses, due to manufacturing defects, were not considered in CFD numerical calculations. The differences between numerical and experimental results should reduce to a negligible value if a better manufacturing process, such as casting, is used for producing the novel heatsink. Further to the validation experiments, other tests were performed on the same two TEG-heatsink assemblies (commercial and novel). The hot plate temperature was varied between 50°C and 150°C, with a step of 25°C, so that the effect of input temperature on TEG-heatsink assembly could be analysed. Results showed that a linear increase of heat source temperature corresponded to a linear increase of temperature difference and, accordingly, to a quadratic increase of maximum power output. The novel heatsink showed a better cooling performance in all cases. Finally, a hybrid heatsink configuration was created by combining two novel heatsinks through a flat copper plate in order to allow the TEG power generation to reach the operative SHM power requirements of tens of mW. A number of experiments was performed, and the results showed that placing two heatsinks on a bare copper sheet allowed a TEG maximum power output of 20.1 mW. Then, pyrolytic graphite sheets (PGS) were introduced on the copper plate to enhance heat transfer from the TEG to the two heatsinks. PGS placed between copper sheet and heatsinks allowed an increase of TEG maximum power output to 20.5 mW. Conversely, placing PGS between copper sheet and TEG resulted to be the best option as TEG maximum power output reached 21.4 mW. The produced energy can be considered enough to feed a wireless SHM system for aerospace applications which, nominally, requires 0.15 mW in inactive mode and 18 mW during transmission. Furthermore, the proposed arrangement resulted to weigh only 45 grams and, thus, can be considered much lighter than a single aircraft data transmission cable that weighs 32 g per metre. Finally, the proposed TEG-heatsink assembly is very adaptable, allowing its introduction in other uses such as biomedical and military applications.

7.3 Limitations and further work

Although the two proposed nonlinear damage localisation techniques allow to find an accurate damage location, they can still be developed. A better accuracy of the time-based method would be achieved by improving stability and accuracy of ToA estimation. Moreover, even though NEMR technique has been evolved to a damage imaging method, called NEMI, the resolution of 2D imaging could be improved through image processing methods such as radial basis functions. There is confidence that both NEMR and NEMI techniques would work correctly on bigger structures as these methods are able to identify low amplitude signals out from noise levels. However, experiments were only carried out on small panels and, thus, further tests shall be performed to validate the proposed techniques on large scale aerospace structures.

On the other hand, albeit the proposed TEG-heatsink configuration is capable to provide enough energy to allow wireless transmission of sensible data, a complete system was not assembled nor tested. The results exposed in this work provide evidence that a complete self-powered wireless SHM system can be designed and pave the way for the future of commercial aircraft maintenance.

References

[1]   Auld, B.A., 1973. *Acoustic fields and waves in solids*. Рипол Классик.

[2]   Cawley, P., 1994. The rapid non-destructive inspection of large composite structures. *Composites*, 25(5), p. 351-357.

[3]   Viktorov, I.A., 1970. *Rayleigh and Lamb waves: physical theory and applications*. Plenum press.

[4]   Ciampa, F., 2012. *Structural Health Monitoring Systems for Impacted Isotropic and Anisotropic Structures*. PhD Thesis, University of Bath.

[5]   Kessler, S.S., Spearing, S.M., Soutis, C., 2002. Damage detection in composite materials using Lamb wave methods. *Smart Materials and Structures*, 11(2), p. 269.

[6]   Mal, A.K., Ricci, F., Gibson, S., Banerjee, S., 2003. Damage detection in structures from vibration and wave propagation data *in NDE for Health Monitoring and Diagnostics*. International Society for Optics and Photonics.

[7]   Yu, L., Giurgiutiu, V., 2008. In situ 2-D piezoelectric wafer active sensors arrays for guided wave damage detection. *Ultrasonics*, 48(2), p. 117-134.

[8]   Tabatabaeipour, M., Hettler, J., Delrue, S., Van Den Abeele, K., 2014. Reconstruction Algorithm for Probabilistic Inspection of Damage (RAPID) in Composites *in 11th European Conference on Non-Destructive Testing (ECNDT 2014)*.

[9]   Flynn, E.B., Todd, M.D., Wilcox, P.D., Drinkwater, B.W., Croxford, A.J., 2011. Maximum-likelihood estimation of damage location in guided-wave structural health monitoring. *Proceedings of the Royal Society A: Mathematical, Physical and Engineering Sciences*, 467(2133), pp. 2575-2596.

[10]   Michaels, J.E., Michaels, T.E., 2007. Guided wave signal processing and image fusion for in situ damage localization in plates. *Wave Motion*, 44(6), p. 482-492.

[11]   Ulrich, T., Sutin, A.M., Claytor, T., Papin, P., Le Bas, P.-Y., TenCate, J.A., 2008. The time reversed elastic nonlinearity diagnostic applied to evaluation of diffusion bonds. *Applied Physics Letters*, 93(15), p. 151914.

[12]   Ostrovsky, L., Johnson, P., 2001. Dynamic nonlinear elasticity in geomaterials. *Rivista del nuovo cimento*, 24(7), p. 1-46.

[13]   Guyer, R.A., Johnson, P.A., 1999. Nonlinear mesoscopic elasticity: Evidence for a new class of materials. *Physics today*, 52, p. 30-36.

[14]   Ciampa, F., Scarselli, G., Meo, M., 2015. Nonlinear imaging method using second order phase symmetry analysis and inverse filtering. *Journal of Nondestructive Evaluation*, 34(2), p. 1-6.

[15]   Ciampa, F., Meo, M., 2012. Nonlinear elastic imaging using reciprocal time reversal and third order symmetry analysis. *The Journal of the Acoustical Society of America*, 131(6), p. 4316-4323.

[16]   Bussgang, J.J., Ehrman, L., Graham, J.W., 1974. Analysis of nonlinear systems with multiple inputs. *Proceedings of the IEEE*, 62(8), p. 1088-1119.

[17]   Ciampa, F., Scarselli, G., Pickering, S., Meo, M., 2015. Nonlinear elastic wave tomography for the imaging of corrosion damage. *Ultrasonics*, 62, p. 147-155.

[18]   Chen, J., Hagiwara, I., Su, X., Shi, Q., 2002. A Bispectrum Feature Extraction Enhanced Structure Damage Detection Approach. *JSME International Journal Series C*, 45(1), p. 121-126.

[19]   Meo, M., Zumpano, G., 2005. Nonlinear elastic wave spectroscopy identification of impact damage on a sandwich plate. *Composite structures*, 71(3-4), pp.469-474.

[20] Meo, M., Polimeno, U., Zumpano, G., 2008. Detecting damage in composite material using nonlinear elastic wave spectroscopy methods. *Applied composite materials*, 15(3), p. 115-126.

[21] Zumpano, G., Meo, M., 2008. Damage localization using transient non-linear elastic wave spectroscopy on composite structures. *International Journal of Non-Linear Mechanics*, 43(3), p. 217-230.

[22] Ciampa, F., Pickering, S., Scarselli, G., Meo, M., 2014. Nonlinear damage detection in composite structures using bispectral analysis *in SPIE Smart Structures and Materials+ Nondestructive Evaluation and Health Monitoring*. International Society for Optics and Photonics.

[23] Donskoy, D., Sutin, A., Ekimov, A., 2001. Nonlinear acoustic interaction on contact interfaces and its use for nondestructive testing. *Ndt & E International*, 34(4), pp. 231-8.

[24] Amerini, F., Meo, M., 2011. Structural health monitoring of bolted joints using linear and nonlinear acoustic/ultrasound methods. *Structural health monitoring*, 10(6), pp. 659-672.

[25] Chen, B.Y., Soh, S.K., Lee, H.P., Tay, T.E. and Tan, V.B., 2016. A vibro-acoustic modulation method for the detection of delamination and kissing bond in composites. *Journal of Composite Materials*, 50(22), pp.3089-3104.

[26] Sohn, H., Lim, H.J., DeSimio, M.P., Brown, K., Derriso, M., 2014. Nonlinear ultrasonic wave modulation for online fatigue crack detection. *Journal of Sound and Vibration*, 333(5), pp. 1473-1484.

[27] Fierro, G.P.M., Meo, M., 2017. Identification of the Location and Level of Loosening in a Multi-bolt Structure using Nonlinear Ultrasound *in 11th International Workshop on Structural Health Monitoring 2017: Real-Time Material State Awareness and Data-Driven Safety Assurance, IWSHM 2017: Real-Time Material State Awareness and Data-Driven Safety Assurance*.

[28] Coverley, P.T., Staszewski, W.J., 2003. Impact damage location in composite structures using optimized sensor triangulation procedure. *Smart materials and structures*, 12(5), p. 795.

[29] Kundu, T., Das, S. and Jata, K.V., 2007. Point of impact prediction in isotropic and anisotropic plates from the acoustic emission data. *The Journal of the Acoustical Society of America*, 122(4), pp.2057-2066.

[30] De Simone, M.E., Boccardi, S., Ciampa, F., Meo, M., 2016. A linearized impact localization algorithm for the health monitoring of aerospace components. *In 8th European Workshop on Structural Health Monitoring, EWSHM 2016*, pp. 1773-1782.

[31] Sedlak, P., Hirose, Y., Enoki, M., Sikula, J., 2008. Arrival time detection in thin multilayer plates on the basis of Akaike information criterion *in 28th European Conference on Acoustic Emission Testing EWGAE-Kraków*.

[32] Bai, H., Atiquzzaman, M., Lilja, D., 2004. Wireless sensor network for aircraft health monitoring. in Broadband Networks. *First International Conference on. 2004. IEEE.*

[33] Hersch, P., Zweibel, K., 1982. *Basic photovoltaic principles and methods*. Solar Energy Research Inst., Golden, CO (USA).

[34] Vullers, R., van Schaijk, R., Doms, I., Van Hoof, C., Mertens, R., 2009. Micropower energy harvesting. *Solid-State Electronics*, 53(7), p. 684-693.

[35] Matak, M., Šolek, P., 2013. Harvesting the Vibration Energy. *American Journal of Mechanical Engineering*, 1(7), p. 438-442.

[36] Cuadras, A., Gasulla, M., Ferrari, V., 2010. Thermal energy harvesting through pyroelectricity. *Sensors and Actuators A: Physical*, 158(1), p. 132-139.

[37] Xu, Y., 2013. *Ferroelectric materials and their applications*. Elsevier.

[38] Wachutka, G., Gerstenmaier, Y., 2006. Thermoelectric and thermionic microgenerators: chances, challenges and limitations *in Mixed Design of Integrated Circuits and System, 2006*. Proceedings of the International Conference IEEE.

[39] Shakouri, A., Bowers, J.E., 1997. Heterostructure integrated thermionic coolers. *Applied Physics Letters*, 71(9), p. 1234-1236.

[40] Tavkhelidze, A., Skhiladze, G., Bibilashvili, A., Tsakadze, L., Jangadze, L., Taliashvili, Z., Cox, I., Berishvili, Z., 2002. Electron tunneling through large area vacuum gap-preliminary results *in Thermoelectrics*. Proceedings ICT'02. Twenty-First International Conference on. 2002. IEEE.

[41] Peltier, J.C.A., 1834. Nouvelles expériences sur la caloricité des courants électriques *in Annales de Chimie et de Physique*.

[42] Seebeck, T.J., 1826. Ueber die magnetische Polarisation der Metalle und Erze durch Temperaturdifferenz. *Annalen der Physik*, 82(3), p. 253-286.

[43] Nolas, G.S., Sharp, J., Goldsmid, J., 2013. *Thermoelectrics: basic principles and new materials developments*. Vol. 45, Springer Science & Business Media.

[44] Woodyard, J.R., 1950. Nonlinear circuit device utilizing germanium. Google Patents.

[45] Lineykin, S., Ben-Yaakov, S., 2007. Modeling and analysis of thermoelectric modules. *Industry Applications, IEEE Transactions*, 43(2), p. 505-512.

[46] Okhotin, A.S., Efremov, A.A., Okhotin, V.S., Pushkarskii, A.S., 1972. Thermoelectric generators (No. FSTC-HT-23-1023-72). ARMY FOREIGN SCIENCE AND TECHNOLOGY CENTER CHARLOTTESVILLE VA.

[47] Naphon, P., Wiriyasart, S., 2009. Liquid cooling in the mini-rectangular fin heat sink with and without thermoelectric for CPU. *International Communications in Heat and Mass Transfer*, 36(2), p. 166-171.

[48] Chang, Y.W., Chang, C.C., Ke, M.T., Chen, S.L., 2009. Thermoelectric air-cooling module for electronic devices. *Applied Thermal Engineering*, 29(13), pp.2731-2737.

[49] Incropera, F.P., Lavine, A.S., Bergman, T.L., DeWitt, D.P., 2007. *Fundamentals of heat and mass transfer*. Wiley.

[50] Jang, S.P., Choi, S.U., 2006. Cooling performance of a microchannel heat sink with nanofluids. *Applied Thermal Engineering*, 26(17), p. 2457-2463.

[51] Abrikosov, A.A., Beknazarov, A., 1988. *Fundamentals of the Theory of Metals*. Vol. 1, North-Holland Amsterdam.

[52] Slack, G.A., 1973. Nonmetallic crystals with high thermal conductivity. *Journal of Physics and Chemistry of Solids*, 34(2), p. 321-335.

[53] Aoki, H., Dresselhaus, M.S., 2013. *Physics of Graphene*. Springer Science & Business Media.

[54] Chen, Y.-M., Ting, J.-M., 2002. Ultra high thermal conductivity polymer composites. *Carbon*, 40(3), p. 359-362.

[55] Pierson, H.O., 1999. *Handbook of chemical vapor deposition: principles, technology and applications*. William Andrew.

[56] Schubert, T., Trindade, B., Weißgärber, T., Kieback, B., 2008. Interfacial design of Cu-based composites prepared by powder metallurgy for heat sink applications. *Materials Science and Engineering: A*, 475(1), p. 39-44.

[57] Forghan, F., Goldthwaite, D., Ulinski, M., Metghalchi, H., 2001. Experimental and theoretical investigation of thermal performance of heat sinks. *In annual meeting for ISME, United States, May*.

[58] Maveety, J., Hendricks, J., 1999. A heat sink performance study considering material, geometry, nozzle placement, and Reynolds number with air impingement. *Journal of Electronic Packaging*, 121(3), p. 156-161.

[59] Maveety, J.G. and Jung, H.H., 2000. Design of an optimal pin-fin heat sink with air impingement cooling. *International Communications in Heat and Mass Transfer*, 27(2), pp.229-240.

[60] Elshafei, E.A.M., 2010, December. Natural convection heat transfer from a heat sink with hollow/perforated circular pin fins. *In 2010 3rd International Conference on Thermal Issues in Emerging Technologies Theory and Applications,* pp. 185-193.

[61] Yu, S.H., Lee, K.S. and Yook, S.J., 2011. Optimum design of a radial heat sink under natural convection. *International Journal of Heat and Mass Transfer*, 54(11-12), pp. 2499-2505.

[62] Chung, D.D.L., 2001. Thermal interface materials. *Journal of Materials Engineering and Performance*, 10(1), pp. 56-59.

[63] Xu, J., Fisher, T.S., 2006. Enhancement of thermal interface materials with carbon nanotube arrays. *International Journal of Heat and Mass Transfer*, 49(9-10), pp. 1658-1666.

[64] Lv, P., Tan, X.W., Yu, K.H., Zheng, R.L., Zheng, J.J., Wei, W., 2016. Super-elastic graphene/carbon nanotube aerogel: a novel thermal interface material with highly thermal transport properties. *Carbon*, 99, pp. 222-228.

[65] Ciampa, F., Meo, M., 2010. Acoustic emission source localization and velocity determination of the fundamental mode A0 using wavelet analysis and a Newton-based optimization technique. *Smart Materials and Structures*, 19(4), p. 045027.

[66] Dennis Jr, J.E., Schnabel, R.B., 1996. *Numerical methods for unconstrained optimization and nonlinear equations*. Vol. 16., Siam.

[67] Boccardi, S., Calla, D.B., Ciampa, F., Meo, M., 2018. Nonlinear elastic multi-path reciprocal method for damage localisation in composite materials. *Ultrasonics*, 82, pp.239-245.

[68] Boccardi, S., Ciampa, F., Meo, M., 2018. Design and development of a heatsink for thermo-electric power harvesting in aerospace applications. *Smart Materials and Structures*.

[69] Boccardi, S., Calla, D.B., Fierro, G.P.M., Ciampa, F., Meo, M., 2016, April. Nonlinear damage detection and localization using a time domain approach. In *Nondestructive Characterization and Monitoring of Advanced Materials, Aerospace, and Civil Infrastructure 2016* (Vol. 9804, p. 98040T). International Society for Optics and Photonics.

[70] Massachusetts Institute of Technology, Department of Mechanical Engineering, 2002. *2.14 Analysis and Design of Feedback Control*, Cambridge, Massachusetts Institute of Technology.

[71] Deng, M., 1999. Cumulative second harmonic generation of lamb-mode propagation in a solid plate. *Journal of Applied Physics*, 85, pp. 3051-3058.

[72] Deng, M., 2003. Analysis of second-harmonic generation of lamb modes using a modal analysis approach. *Journal of Applied Physics*, 94, pp. 4152-4159